

# **Accurate Drag Prediction For Transitional External Flow over Airfoils**

Wassim Basha

A Thesis  
in  
The Department  
of  
Mechanical and Industrial Engineering

Presented in Partial Fulfillment of the Requirements  
for the Degree of Master of Applied Science (Mechanical Engineering) at  
Concordia University  
Montréal, Québec, Canada

April 2006

© Wassim Basha, 2006



Library and  
Archives Canada

Bibliothèque et  
Archives Canada

Published Heritage  
Branch

Direction du  
Patrimoine de l'édition

395 Wellington Street  
Ottawa ON K1A 0N4  
Canada

395, rue Wellington  
Ottawa ON K1A 0N4  
Canada

*Your file    Votre référence*

*ISBN: 0-494-14297-9*

*Our file    Notre référence*

*ISBN: 0-494-14297-9*

#### NOTICE:

The author has granted a non-exclusive license allowing Library and Archives Canada to reproduce, publish, archive, preserve, conserve, communicate to the public by telecommunication or on the Internet, loan, distribute and sell theses worldwide, for commercial or non-commercial purposes, in microform, paper, electronic and/or any other formats.

The author retains copyright ownership and moral rights in this thesis. Neither the thesis nor substantial extracts from it may be printed or otherwise reproduced without the author's permission.

#### AVIS:

L'auteur a accordé une licence non exclusive permettant à la Bibliothèque et Archives Canada de reproduire, publier, archiver, sauvegarder, conserver, transmettre au public par télécommunication ou par l'Internet, prêter, distribuer et vendre des thèses partout dans le monde, à des fins commerciales ou autres, sur support microforme, papier, électronique et/ou autres formats.

L'auteur conserve la propriété du droit d'auteur et des droits moraux qui protègent cette thèse. Ni la thèse ni des extraits substantiels de celle-ci ne doivent être imprimés ou autrement reproduits sans son autorisation.

---

In compliance with the Canadian Privacy Act some supporting forms may have been removed from this thesis.

Conformément à la loi canadienne sur la protection de la vie privée, quelques formulaires secondaires ont été enlevés de cette thèse.

While these forms may be included in the document page count, their removal does not represent any loss of content from the thesis.

Bien que ces formulaires aient inclus dans la pagination, il n'y aura aucun contenu manquant.

  
**Canada**

# ABSTRACT

Accurate Drag Prediction For Transitional External Flow over Airfoils

Wassim Basha

When analyzing the flow over airfoils at relatively low Reynolds numbers, transition from laminar to turbulent flow plays an important role in shaping the flow features and in quantifying the airfoil performance such as lift and drag. In most cases, laminar separation bubbles and transition zones that extend over a relatively long portion of the airfoils surface are present. Hence the proper modeling of transition, including both the onset and extent of the transition region, will lead to a more accurate drag prediction.

The onset of transition is related to the disturbances that propagate in the laminar flow region. Analyzing such instabilities is carried out either by a full study of the Tollmien-Schlichting waves or by the use of empirical correlations most of which are based on results for two-dimensional incompressible flows. As for the transition extent modeling, different intermittency functions of the linear, algebraic or differential type have been developed.

The current work presents a transition model that combines existing methods for predicting the onset and extent of the transition region. The transition onset is predicted using Cebeci and Smith's correlation which is based on Michel's method for incompressible two-dimensional flow while the extent of transition is quantified by developing a linear model for the intermittency function. The proposed transition model is implemented into the Spalart-Allmaras turbulence model available in the commercial software, Fluent, using user defined functions (UDF). It is then used in simulating transitional flow in different well documented experimental cases including

single-element and two-element airfoils under different free-stream conditions. Given the experimental data, the results obtained with the developed transition model reflect a consistent and significant improvement in drag prediction, when compared with the drag predicted using a fully turbulent flow simulation.

## ACKNOWLEDGEMENTS

I would like to thank all those people who made this thesis possible and an enjoyable experience for me. First of all I would like to express my sincere gratitude to my supervisor, Dr. Wahid S. Ghaly, who guided me through this work. It was because of his support, advice and consistent efforts that this work was accomplished.

I would like also to thank Dr. Marius Paraschivoiu for his contribution and many useful discussion.

I am also grateful to my colleagues for their support and advice; especially to Kasra Daneshkhah and Temesgen Mengistu.

Finally, I wish to thank my parents and family for their continuous support and encouragement. I dedicate this work to them.

# TABLE OF CONTENTS

LIST OF FIGURES . . . . .	viii
LIST OF TABLES . . . . .	xi
LIST OF SYMBOLS . . . . .	xii
<b>1 Introduction</b>	<b>1</b>
1.1 Accurate Drag Prediction . . . . .	1
1.2 Transition Modeling . . . . .	3
1.3 Thesis Outline . . . . .	5
<b>2 Transition: Onset And Extent</b>	<b>6</b>
2.1 Transition Onset . . . . .	6
2.1.1 Empirical Methods . . . . .	7
2.1.2 LSE Methods . . . . .	9
2.2 Transition Extent . . . . .	12
<b>3 Numerical Analysis</b>	<b>21</b>
3.1 Free Laminar to Turbulent Transition Model . . . . .	22
3.1.1 Transition Onset Prediction . . . . .	22
3.1.2 Transition Zone Prediction . . . . .	23
3.2 Description of The Computational Domain . . . . .	25
3.3 Flow Solver Description . . . . .	29
3.3.1 Navier-Stokes Equations . . . . .	29
3.3.2 Euler Equations . . . . .	31
3.4 Discretization of The Governing Equations . . . . .	32
3.5 The Turbulence Model . . . . .	33
3.5.1 The Spalart-Allmaras Turbulence Model . . . . .	34
3.6 Convergence to Steady State . . . . .	39

3.7	Numerical Assessment of Fluent for The	
	NACA-0012 Airfoil . . . . .	40
3.7.1	Mesh Type Assessment . . . . .	40
3.7.2	Turbulence Model Assessment . . . . .	43
3.7.3	Grid Sensitivity Analysis . . . . .	44
<b>4</b>	<b>Transition Model Assessment for a One-Element Airfoil</b>	<b>56</b>
4.1	NLF-0416 Airfoil (Incompressible Case) . . . . .	56
4.1.1	Case I: $M_\infty = 0.1, Re = 4 * 10^6$ . . . . .	58
4.1.2	Mesh Sensitivity Analysis . . . . .	62
4.1.3	Case II: $M_\infty = 0.1, Re = 2 * 10^6$ . . . . .	65
4.2	NLF-0416 Airfoil (Compressible Case) . . . . .	67
4.2.1	Case III: $M_\infty = 0.4, Re = 6 * 10^6$ . . . . .	67
<b>5</b>	<b>Transition Model Assessment for a Two-Element Airfoil</b>	<b>85</b>
5.1	NLR-7301 Airfoil With a Trailing Edge Flap . . . . .	85
<b>6</b>	<b>Conclusion</b>	<b>97</b>
6.1	Completed Work . . . . .	97
6.2	Future Work . . . . .	98
	<b>Bibliography</b>	<b>99</b>

## LIST OF FIGURES

2.1	Orr-Sommerfeld spatial amplification curves,[Drela and Giles, [7]]. . .	19
2.2	Universal distribution of $\gamma$ vs. $\xi$ with transition due to different agents, [Dhawan and Narasimha, [9]]. . . . .	20
2.3	Variation of $C^2/3$ with $Re_{x_{tr}}$ ,[Cebeci, [15]]. . . . .	20
3.1	A sample of a structured O-type mesh of a NACA-0012 airfoil. . . . .	47
3.2	A sample of a structured C-type mesh of a NACA-0012 airfoil. . . . .	48
3.3	A sample of a hybrid mesh of a NLF-0416 airfoil. . . . .	49
3.4	Lift coefficient variation with respect to mesh quality for the NACA- 0012 airfoil. . . . .	50
3.5	Drag coefficient variation with respect to mesh quality for the NACA- 0012 airfoil. . . . .	51
3.6	Lift coefficient variation with respect to the turbulence model for the NACA-0012 airfoil. . . . .	52
3.7	Drag coefficient variation with respect to the turbulence model for the NACA-0012 airfoil. . . . .	53
3.8	Lift coefficient variation with respect to $y^+$ values for the NACA-0012 airfoil. . . . .	54
3.9	Drag coefficient variation with respect to $y^+$ values for the NACA-0012 airfoil. . . . .	55
4.1	Model validation of the transition onset for the NLF-0416 airfoil Case I ( $M_\infty = 0.1, Re = 4 * 10^6$ ). . . . .	70
4.2	Drag coefficient comparison for the NLF-0416 airfoil Case I ( $M_\infty =$ $0.1, Re = 4 * 10^6$ ). . . . .	71



4.3	Lift coefficient comparison for the NLF-0416 airfoil Case I ( $M_\infty = 0.1, Re = 4 * 10^6$ ). . . . .	72
4.4	Pressure coefficient distribution for the NLF-0416 airfoil Case I at $\alpha = 0^\circ$ ( $M_\infty = 0.1, Re = 4 * 10^6$ ). . . . .	73
4.5	Pressure coefficient distribution for the NLF-0416 airfoil Case I at $\alpha = 8^\circ$ ( $M_\infty = 0.1, Re = 4 * 10^6$ ). . . . .	73
4.6	Skin-Friction coefficient distribution for the NLF-0416 airfoil Case I at $\alpha = 0^\circ$ ( $M_\infty = 0.1, Re = 4 * 10^6$ ). . . . .	74
4.7	Skin-Friction coefficient distribution for the NLF-0416 airfoil Case I at $\alpha = 8^\circ$ ( $M_\infty = 0.1, Re = 4 * 10^6$ ). . . . .	74
4.8	Mach number contours for the NLF-0416 airfoil Case I at $\alpha = 0^\circ$ ( $M_\infty = 0.1, Re = 4 * 10^6$ ). . . . .	75
4.9	Mach number contours for the NLF-0416 airfoil Case I at $\alpha = 8^\circ$ ( $M_\infty = 0.1, Re = 4 * 10^6$ ). . . . .	75
4.10	Lift coefficient comparison on three different meshes for the NLF-0416 airfoil Case I ( $M_\infty = 0.1, Re = 4 * 10^6$ ). . . . .	76
4.11	Drag coefficient comparison on three different meshes for the NLF-0416 airfoil Case I ( $M_\infty = 0.1, Re = 4 * 10^6$ ). . . . .	77
4.12	Model validation of the transition onset for the NLF-0416 airfoil Case II ( $M_\infty = 0.1, Re = 2 * 10^6$ ). . . . .	78
4.13	Drag coefficient comparison for the NLF-0416 airfoil Case II ( $M_\infty = 0.1, Re = 2 * 10^6$ ). . . . .	79
4.14	Lift coefficient comparison for the NLF-0416 airfoil Case II ( $M_\infty = 0.1, Re = 2 * 10^6$ ). . . . .	80
4.15	Mach number contours for the NLF-0416 airfoil Case III at $\alpha = 0^\circ$ ( $M_\infty = 0.4, Re = 6 * 10^6$ ). . . . .	81

4.16	Mach number contours for the NLF-0416 airfoil Case III at $\alpha = 12^\circ$ ( $M_\infty = 0.4, Re = 6 * 10^6$ ). . . . .	81
4.17	Model validation of the transition onset for the NLF-0416 airfoil Case III ( $M_\infty = 0.4, Re = 6 * 10^6$ ). . . . .	82
4.18	Drag coefficient comparison for the NLF-0416 airfoil Case III ( $M_\infty =$ $0.4, Re = 6 * 10^6$ ). . . . .	83
4.19	Lift coefficient comparison for the NLF-0416 airfoil Case III ( $M_\infty =$ $0.4, Re = 6 * 10^6$ ). . . . .	84
5.1	Pressure coefficient distribution for the NLR-7301 airfoil at $\alpha = 6^\circ$ . . .	90
5.2	Pressure coefficient distribution for the NLR-7301 airfoil at $\alpha = 13.1^\circ$ . . .	90
5.3	Mach number contours for the NLR-7301 airfoil at $\alpha = 6^\circ$ . . . . .	91
5.4	Static pressure contours for the NLR-7301 airfoil at $\alpha = 6^\circ$ . . . . .	91
5.5	Mach number contours for the NLR-7301 airfoil at $\alpha = 13.1^\circ$ . . . . .	92
5.6	Static pressure contours for the NLR-7301 airfoil at $\alpha = 13.1^\circ$ . . . . .	92
5.7	Model validation of the transition onset for the NLR-7301 airfoil. . .	93
5.8	Drag coefficient comparison for the NLR-7301 airfoil. . . . .	94
5.9	Lift coefficient comparison for the NLR-7301 airfoil. . . . .	95
5.10	Polar drag plot for the NLR-7301 airfoil. . . . .	96

## LIST OF TABLES

3.1	Experimental and numerical free-stream flow conditions for the NACA-0012 case. . . . .	42
3.2	Recommended $y^+$ values for different wall treatment functions. . . . .	44
4.1	Experimental and numerical free-stream flow conditions for the NLF-0416 airfoil cases. . . . .	58
4.2	Difference in the lift and drag coefficients for the NLF-0416 airfoil Case I ( $M_\infty = 0.1, Re = 4 * 10^6$ ). . . . .	61
4.3	$y^+$ variations with respect to the mesh quality. . . . .	63
4.4	Difference in the lift and drag coefficients obtained for three different meshes for the NLF-0416 airfoil Case I ( $M_\infty = 0.1, Re = 4 * 10^6$ ). . .	64
4.5	Difference in the lift and drag coefficients for the NLF-0416 airfoil Case II ( $M_\infty = 0.1, Re = 2 * 10^6$ ). . . . .	66
4.6	Difference in the lift and drag coefficients for the NLF-0416 airfoil Case III ( $M_\infty = 0.4, Re = 6 * 10^6$ ). . . . .	69
5.1	Experimental and numerical free-stream flow conditions for the NLR-7301 case. . . . .	86
5.2	Difference in the lift and drag coefficients for the NLR-7301 airfoil. . .	88

## LIST OF SYMBOLS

$C$	Model parameter.
$C_\mu$	Model constant (=0.11).
$d$	Shortest distance to the wall.
$Re_c$	Reynolds number based on the chord length ( $= \frac{uc}{\nu}$ ).
$Re_x$	Reynolds number based on local distance ( $= \frac{ux}{\nu}$ ).
$Re_\theta$	Reynolds number based on the momentum thickness ( $= \frac{u\theta}{\nu}$ ).
$u_e$	Velocity at the edge of the boundary layer.
$x_i$	Point of instability to the Tollmien-Schlichting.
$x_t$	Transition onset location.
$y^+$	Viscous sublayer Reynolds number ( $= \frac{\rho u_\tau y_p}{\mu}$ ).
$\Gamma$	Transition intermittency function.
$\Gamma_b$	Normal-distance-dependent intermittency function.
$\Gamma_x$	Surface-distance-dependent intermittency function.
$\theta$	Momentum thickness.
$\mu$	Viscosity.
$\nu$	Kinematic viscosity.
$\Omega$	Vorticity vector magnitude.

### Subscripts

$i$	Point of instability to the Tollmien-Schlichting.
$L$	Laminar flow.
$t$	Transition onset / Turbulent flow.
$tr$	Transition onset.
$\infty$	Free-stream flow conditions.

### Acronyms

CFD	Computational Fluid Dynamics.
EWT	Enhanced Wall Treatment.
LSE	Linear Stability Equations.

neqWT	Non-equilibrium Wall Treatment.
NLF	Natural Laminar Flow.
RANS	Reynolds Averaged Navier-Stokes.
SA	Spalart-Allmaras.
SWT	Standard Wall Treatment.
UDF	User Defined Function.

# Chapter 1

## Introduction

### 1.1. Accurate Drag Prediction

Accurate CFD-based drag prediction is considered as one of the important quality measures in external flow simulation using computational fluid dynamics (CFD) due to its sensitivity to all the details of the CFD simulation and its influence on the aerodynamic performance of flying objects, airplanes in particular. As an example of drag effect on aircraft design, a reduction of one drag count ( $\Delta C_D = 10^{-4}$ ) on a subsonic civil transport airplane means about 200 lb (1 person) more in payload. Another study carried out on the Lockheed C-5 airplane showed that one drag count at cruise conditions (0.4 % of the total drag on the aircraft) is equivalent to about 1000 lb in load [1]. Thus it is crucial that the drag values predicted from CFD flow simulations would be as close as possible to the actual in-flight values in order to reflect the actual performance of the aircraft and thus supply a more reliable performance prediction.

Drag over a wing can be divided into three major components: viscous, induced and wave drag. Induced drag is generated by the downwash velocity induced by the wing tip vortices, wave drag is a result of the shock waves generated in transonic flows.

As for the viscous drag, it is mostly generated by skin friction and thus it is directly related to the viscous flow behavior [1]. Induced and wave drag are generated by normal forces and thus they can be well predicted using Euler equations simulations provided that the viscous effects are confined to a thin layer near the wall. On the other hand, viscous drag can only be predicted by solving the Navier-Stokes equations since they are generated by tangential forces [1]. To concentrate on the accurate prediction of viscous drag, incompressible transitional flow ( $M_\infty \leq 0.4$ ) is simulated over two-dimensional airfoils, where both wave drag and induced drag vanish.

With the maturity of CFD methods and the ever increasing computing power, engineers are spending more time using CFD tools to design, analyze and predict the aircraft aerodynamic performance. The main reason behind such a trend is the improved effectiveness, accuracy and time-saving of current analytical/computational tools. Given that wind tunnel testing is time consuming, very expensive and elaborate, designers are also using CFD to reduce to a minimum the number of tests that need to be performed so as to validate a given design hence reducing the cost of any new design. Such a reputation acquired by CFD was made possible by decades of work dedicated to improving CFD methodology, where it is becoming a more accurate and reliable tool, and by the exponential growth of computer technology. Today's flow solvers are capable of predicting the different flow properties and variables with high degree of accuracy such that most of the design and analysis procedures are carried out in a reasonable run time. The CFD-based drag prediction is no exception to the rule. However, and despite of all the advances that have been made in the CFD discipline, there is still the need for more improvements particularly when it comes to accurately predicting the aerodynamic drag. That is why accurate drag prediction is a current area of active research.

During a CFD-based drag evaluation, several critical factors have to be considered. Those factors range from geometry fidelity, mesh quality, flow solver, convergence level, laminar-to-turbulent flow transition model, turbulence model and drag evaluation method [2]. The involvement of all these elements, whether in a positive or negative way, makes it more difficult to accurately estimate the drag using CFD.

The focus of this work is on modeling the boundary layer flow transition from laminar to turbulent flow. This is done while keeping in mind the other factors mentioned earlier.

## 1.2. Transition Modeling

Laminar to turbulent transition modeling is one of the key factors affecting CFD-based drag prediction using Reynolds Averaged Navier-Stokes (RANS) equations. Failing to accurately predict the transition behavior in the boundary layer has an adverse effect on the computed drag, as well as on other flow properties. This is due to the large discrepancy particularly in shear stress between the laminar and the turbulent regions. The flow behavior in these two zones differ significantly and thus all the flow variables. Add to this the fact that the transition zone might, in some cases, extend over a significant part of the airfoil surface. Thus in cases where the laminar and the transition zones occupy a relatively large portion of the airfoil surface, neglecting the effect of these two zones by assuming fully turbulent flow over the entire airfoil will definitely result in numerically computed flow properties that diverge from the actual ones. This will lead to an inaccurate evaluation of the viscous properties in the boundary layer, and consequently an inaccurate drag prediction.

For about a century, a large number of studies focused on predicting the transition criteria. However, till today a complete understanding of this phenomenon and what physically is happening in the transition region have not been fully understood.



In the next chapter, an attempt is made in order to explore the different aspects of transition, the physics behind it and some of the methods being used in aerospace related applications.

As it has been mentioned earlier, the current work will deal with the development of a methodology that is capable of modeling transition in terms of its onset and in terms of the extent of the transition region. When dealing with the subject, several issues were taken into account. Firstly, such a model is intended for use with solving the RANS equations and a turbulence model. Therefore it should be compatible with the solver and the turbulence model to be used. Secondly, it must be easy to implement and should require the least processing time possible. All this should be done without losing the credibility of the results to be obtained. Such a task was performed in two steps, first the transition onset is predicted. This is followed by introducing an intermittency function,  $\Gamma$ , that will represent the extent of the transition region. In a typical flow simulation using RANS solver coupled with a one- or two-equation turbulence model, the effective viscosity  $\mu_{eff}$  is computed as:

$$\mu_{eff} = \mu_L + \mu_t \quad (1.1)$$

where  $\mu_L$  and  $\mu_t$  are the laminar and turbulent viscosity, respectively. One of the methods of introducing the transition region in a fully turbulent boundary layer is by multiplying the turbulent viscosity by the intermittency function  $\Gamma$ . Then the modified effective viscosity is equal to:

$$\mu_{eff} = \mu_L + (\Gamma * \mu_t) \quad (1.2)$$

Thus for  $\Gamma$  equal to zero, the boundary layer is fully laminar and for  $\Gamma$  equal to one the boundary layer is fully turbulent. For any value in between 0 and 1, the flow is in the transition region.

### 1.3. Thesis Outline

A review of some of the previous methods developed for transition onset and extent are given in Chapter 2. A complete description of the model, its implementation and the CFD solver (in which it is implemented) is given in Chapter 3. Also a section is included in the same chapter where an assessment of the CFD solver capabilities was carried out (Sec. 3.7). This is followed by an assessment of the developed free transition model where two cases, a single- and a two-element airfoil in two-dimensional transitional flows, are tested under different flow conditions (Chapters 4 and 5). The last chapter summarizes the most salient points covered in the work, this is followed by a layout of any future work.

## Chapter 2

# Transition: Onset And Extent

As mentioned in Chapter 1, transition plays an important role in estimating the different flow characteristics, especially drag. Due to such a role and in order to accurately predict transition, there is a significant body of literature on describing some of the mechanism involved in transition and on quantifying it. This chapter gives a brief description of previous work done on the two aspects of transition, namely onset and extent, where an explanation of the different methods used in solving and analyzing the problem with a description of some of the procedures developed for predicting these two aspects with an emphasis on those that are related to external flow analysis in aerospace applications.

### 2.1. Transition Onset

The first step in the transition analysis procedure consists of the prediction of the transition onset, due to the fact that most of the calculations to follow depend on it. Transition onset is the point at which the transition region starts, the point at which the disturbances in the laminar flow accumulate to a certain degree such that turbulent spots start to form and grow in the flow field. Going back to the reason of which viscous flows undergo a transition from laminar into turbulent, a

wide range of parameters play a role in creating these disturbances. Those which play a major role are free-stream turbulence, pressure gradient, surface curvature, surface roughness, mass transfer and heat transfer. Studies concerning the prediction of transition onset range from using empirical correlations, solutions of the unsteady Navier-Stokes equations (direct numerical simulation), solving the linear stability equations (LSE) or the parabolized stability equations (PSE). While it has been proven that the direct numerical simulation (DNS) can predict the transition onset for simple flows, the large computer requirements and the difficulty that it encounters in the case of complex bodies makes it a hard choice to be implemented in engineering applications in the near future [3, 4]. Regarding the PSE method, the concept is still new and its direct application into engineering is still far from being realized [3].

### 2.1.1 Empirical Methods

A lot of effort has been spent on the development of empirical equations, that quantify the flow behavior and are validated with experimental data, to predict the transition onset. This could be due to the fact, that sophisticated theoretical approaches to simulate transitional flow are difficult to implement and require a lot of computing resources. However, most of the empirical methods are based on incompressible two-dimensional flows. They are relatively accurate and are simple to implement. To name some, there are the methods of Michel (1951), Granville (1953) Smith and Gamberoni (1956), Van Ingen (1956), Crabtree (1958), and Van Driest and Blumer (1963) [5, 6]. Of those that are widely recognized for their accuracy and ease of implementation in engineering applications are Michel's and Granville's methods [5].

#### **Michel Method:**

Michel based his method on relating the transition momentum thickness Reynolds number ( $Re_{\theta_{tr}}$ ) to the local distance Reynolds number ( $Re_x$ ) at transition through a

universal relation given as [6]:

$$Re_{\theta_{tr}} \approx \frac{U(x)\theta(x)}{\nu} \approx 2.9Re_{x,tr}^{0.4}, \quad 0.4 * 10^6 \leq Re_x \leq 7 * 10^6 \quad (2.1)$$

Following Michel method, Cebeci and Smith [5] suggested later that the  $e^9 - method$  that is discussed later, can be correlated using the following equation:

$$Re_{\theta_{tr}} = 1.174 [1 + (22,400/Re_x)] Re_x^{0.46}, \quad 0.1 * 10^6 \leq Re_x \leq 40 * 10^6 \quad (2.2)$$

Equation 2.2 is applicable for attached flows on airfoils for chord Reynolds numbers,  $Re_c$ , greater than  $2 * 10^6$ .

### **Granville Method:**

Granville correlated the value of  $(Re_{\theta_{tr}} - Re_{\theta_{xi}})$  to the mean Pohlhausen (Thwaites) parameter  $\lambda_m$  through a single curve [6]. Here again  $Re_{\theta_{tr}}$  is the Reynolds number based on transition momentum thickness and  $Re_{\theta_{xi}}$  is the Reynolds number based on the momentum thickness at the point of instability to Tollmien-Schlichting waves,  $x_i$ . The parameter  $\lambda_m$  is defined as [6]:

$$\lambda_m = \frac{1}{(x_{tr} - x_i)} \int_{x_i}^{x_{tr}} \lambda(x) dx \quad (2.3)$$

where  $\lambda = \theta^2(dU/dx)/\nu$ . The transition onset is predicted through the curve defined by Granville as [6]:

$$Re_{\theta}(x_{tr}) \approx Re_{\theta}(x_i) + 450 + 400e^{60\lambda_m} \quad (2.4)$$

for  $\lambda < 0.04$ . For an adverse gradient ( $\lambda \approx -0.1$ ), the last term is negligible and transition is very near to  $x_i$ . For a favorable gradient the last term is very large and transition moves far downstream. In comparison with Michel method, an extra computation of  $x_i$  is required. That is why the current method is known as the two step method while Michel method is known as the one step method [6].

### 2.1.2 LSE Methods

The linear stability equations (LSE) analysis is based on the study of the disturbances that occur in the laminar boundary layer flow. By analyzing the behavior and stability of these waves (disturbances), known as the Tollmien-Schlichting instabilities, transition is predicted. This is done by finding the solution of the wave equations known as the Orr-Sommerfeld equation. For the case of two-dimensional incompressible flows, the Orr-Sommerfeld equation can be written as a fourth-order ordinary differential equation in the following manner [3]:

$$\nu (\phi^{iv} - 2\alpha^2 \phi'' + \alpha^4 \phi) = i [(\alpha u - \omega) (\phi'' - \alpha^2 \phi) - \alpha u'' \phi] \quad (2.5)$$

Here primes denote differentiation with respect to  $y$ ,  $u$  denotes the stream-wise velocity profile and  $\phi(y)$  denotes the complex amplitude of the disturbance stream function  $\psi'$  defined by the fluctuating velocity components  $u'$  and  $v'$

$$u' = \frac{\partial \psi'}{\partial y}, v' = -\frac{\partial \psi'}{\partial x} \quad (2.6)$$

The parameter  $\alpha$ , the wave number of the disturbance, is related to  $\lambda$ , the wave-length of the disturbance, by  $\lambda = 2\pi/\alpha$ .  $\omega$  is the circular frequency. In a dimensionless form, the Orr-Sommerfeld equation can be written in the following manner [3]:

$$\phi^{iv} - 2\alpha_l^2 \phi'' + \alpha_l^4 \phi = iR [(\alpha_l \bar{u} - \bar{\omega}) (\phi'' - \alpha_l^2 \phi) - \alpha_l \bar{u}'' \phi] \quad (2.7)$$

In Eq. 2.7, the primes denote differentiation with respect to  $\bar{y}$  which is equal to  $y/l$ . The parameter  $\phi(\bar{y})$  is the complex amplitude of the disturbance stream function  $\psi'(\bar{x}, \bar{y}, \tau)$  and is defined as [3]:

$$\psi'(\bar{x}, \bar{y}, \tau) = \phi(\bar{y}) \exp[i(\alpha_l \bar{x} - \bar{\omega} \tau)] \quad (2.8)$$

The dimensionless parameters are given by :

$$\alpha_l = \alpha l, \quad \bar{u} = \frac{u}{u_0}, \quad \bar{\omega} = \frac{u_0 \omega}{l}, \quad R = \frac{u_0 l}{\nu} \quad (2.9)$$

The eigenvalues of the Orr-sommerfeld equation can be found, after applying the corresponding boundary conditions, and thus the amplification rate  $\alpha$  and frequency  $\omega$  can be calculated. Then the transition onset can be predicted using the  $e^n$ -method. The procedure, which is famously known as the  $e^n$ -method, is based on the growth of the Tollmien-Schlichting instabilities in the laminar flow. The analysis assumes that when these disturbances in the boundary layer are amplified to a certain limit, usually specified as the  $n$  factor, flow undergoes a transition from laminar into turbulent. Most of the procedures use a value of  $n$  equal to 9 or  $e^9 \simeq 8100$  and thus they are identified as the  $e^9$ -method. This factor,  $n$ , is defined as the logarithm of the maximum amplification ratio ( $A/A_0$ ) calculated using the  $\alpha$  and  $\omega$  obtained from the solution of the Orr-sommerfeld equation [3].

Smith and Gamberoni(1956) and independently van Ingen (1956) have estimated that by using the temporal stability theory, the total growth ratio is equal to

$$\frac{A}{A_0} = \exp \left[ \int_{x_i}^{x_{tr}} \alpha \omega_i dt \right] \approx e^9 \quad (2.10)$$

This will be known later as the  $e^9$ -method [6]. In the spirit of that, Jaffe et al. (1970) have proved later that by using the spatial stability theory a better results for transition measurements can be achieved [6]. The growth ratio given by Jaffe et al. is given as:

$$\frac{A}{A_0} = \exp \left[ \int_{x_i}^{x_{tr}} (-\alpha_i) dx \right] \approx e^{10} \quad (2.11)$$

Also based on the  $e^9$ -method and the previous achievements in the field, Drela and Giles have developed a transition prediction method that will be described below.

### **Drela and Giles:**

What Drela and Giles did was the implementation of the spatial-amplification theory based on the Orr-sommerfeld equation and the  $e^9$ -method, that was developed by Smith and Gamberoni and Ingen, in a transition prediction model [7]. By using the

Falkner-Skan profile family for boundary layer flow description, the Orr-Sommerfeld equation has been solved for the spatial amplification rates of a range of shape parameters and unstable frequencies. Then based on the work done by Gleyzes et al., where they employed an incompressible integral boundary-layer formulation to calculate the transitional bubble, the envelopes of the integrated rates are approximated by straight lines which equation is given below [7]:

$$\tilde{n} = \frac{d\tilde{n}}{dRe_\theta} (H_k) [Re_\theta - Re_{\theta_0} (H_k)] \quad (2.12)$$

Here,  $\tilde{n}$  is the logarithm of the maximum amplification ratio (same as  $n$  in the previous discussion).  $H_k$  is the kinematic shape parameter and it is defined with the density taken constant across the boundary layer. The slope  $d\tilde{n}/dRe_\theta$  and the critical Reynolds number  $Re_{\theta_0}$  are expressed by the following empirical equations [7]:

$$\frac{d\tilde{n}}{dRe_\theta} = 0.01 \{ [2.4H_k - 3.7 + 2.5 \tanh(1.5H_k - 4.65)]^2 + 0.25 \}^{1/2} \quad (2.13)$$

$$\log_{10} Re_{\theta_0} = \left( \frac{1.415}{H_k - 1} - 0.489 \right) \tanh \left( \frac{20}{H_k - 1} - 12.9 \right) + \frac{3.295}{H_k - 1} + 0.44 \quad (2.14)$$

Equation 2.12 that describes the spatial amplification curves are plotted in Fig. 2.1, on the next page, together with the actual amplification curves [7]. Then by integrating Eq. 2.13 with respect to  $Re_\theta$ , the growth ratio is defined as:

$$\tilde{n} = \int_{Re_{\theta_0}}^{Re_\theta} \frac{d\tilde{n}}{dRe_\theta} dRe_\theta \quad (2.15)$$

However, Drela and Giles transform the coordinate system to the spatial coordinate  $\xi$  which is along the streamlines. Thus the integration of the amplification rate is rewritten as [7]:

$$\frac{d\tilde{n}}{d\xi} = \frac{d\tilde{n}}{dRe_\theta} \frac{dRe_\theta}{d\xi} = \frac{d\tilde{n}}{dRe_\theta} \frac{1}{2} \left( \frac{\xi}{u_e} \frac{du_e}{d\xi} + 1 \right) \frac{\rho_e u_e \theta^2}{\mu_e \xi} \frac{1}{\theta} \quad (2.16)$$

and by implementing the following empirical relations,

$$\frac{\rho_e u_e \theta^2}{\mu_e \xi} \equiv l(H_k) = \frac{6.54H_k - 14.07}{H_k^2} \quad (2.17)$$



$$\frac{\xi}{u_e} \frac{du_e}{d\xi} \equiv m(H_k) = \left( 0.058 \frac{(H_k - 4)^2}{H_k - 1} - 0.068 \right) \frac{1}{l(H_k)} \quad (2.18)$$

the new formula for the amplification rate, with respect to  $\xi$ , is written in terms of  $H_k$  and  $\theta$  as:

$$\frac{d\tilde{n}}{d\xi}(H_k, \theta) = \frac{d\tilde{n}}{dRe_\theta}(H_k) \frac{m(H_k) + 1}{2} l(H_k) \frac{1}{\theta} \quad (2.19)$$

Then the rate  $\tilde{n}$  can be expressed in the following manner:

$$\tilde{n}(\xi) = \int_{\xi_0}^{\xi} \frac{d\tilde{n}}{d\xi} d\xi \quad (2.20)$$

where  $\xi_0$  is the point where  $Re_\theta = Re_{\theta_0}$ .

## 2.2. Transition Extent

The second aspect of transition modeling is that of the transition extent prediction. That is the zone over which the boundary layer undergoes a change from a fully laminar flow to a fully turbulent flow. Such a region starts at the transition onset location  $x_t$ , where turbulent spots start to form in the laminar boundary layer, and ends at the point where the flow is fully (100 percent) turbulent. The region can be represented quantitatively by using intermittency functions, generally known as  $\Gamma$  functions. Such functions are defined as the percentage of time in which the flow is turbulent. Thus at the beginning of the transition zone, the  $\Gamma$  function is  $0^+$  and it increases until it approaches  $1^-$  at the end of the transition zone. A wide range of intermittency functions have been developed. Those functions are classified under three types: the linear-combination type, the algebraic type and the differential type functions which are the most complex. In the case of linear-combination or algebraic model, the intermittency distribution is needed as an input. For the case of a differential model, the RANS equations of motion are solved with one- or two-equation turbulence closure. Narasimha has performed a detailed survey of the different transition models that have been proposed [8], here are some of these methods.

### **Dhawan and Narasimha:**

Dhawan and Narasimha [9] have correlated the experimental data collected and proposed a generalized distribution function across the transition region. Such a function, which is developed for two-dimensional incompressible flow along a flat plate, could be based on the hypothesis of concentrated breakdown. The intermittency function is defined as [8, 9]:

$$\gamma = \begin{cases} 0 & \text{if } x < x_t, \\ 1 - \exp \left[ -\frac{(x-x_t)^2 n \sigma}{U} \right] = 1 - \exp [-0.41 \xi^2] & \text{if } x \geq x_t. \end{cases} \quad (2.21)$$

where  $x_t$  is the transition onset location,  $U$  is the free stream velocity,  $n$  is the spot formation rate (per unit time, per unit distance in the span-wise direction),  $\sigma$  is a spot propagation parameter and the parameter  $\xi$  is defined as:

$$\xi = (x - x_t) / \lambda \quad (2.22)$$

which is a non-dimensional variable that describes the extent of transition and is a function of  $\lambda$ , the distance between the two stations where  $\gamma = 0.25$  and  $\gamma = 0.75$ .

$$\lambda = \{x\}_{\gamma=0.75} - \{x\}_{\gamma=0.25} \quad (2.23)$$

It is to be noted, from Eq. 2.21, that transition is described by a universal intermittency distribution. The same equation is plotted in comparison with experimental data used by Dhawan and Narasimha [9] and as it could be seen from Fig. 2.2 the agreement between experimental results and the equation is obvious.

Concerning the intermittency function distribution across the boundary layer, that is in the direction normal to the wall surface, Dhawan and Narasimha suggests that  $\gamma$  varies from a constant maximum value close to the wall to zero towards the edge of the boundary layer. However, it is noted by the authors that such a variation has a secondary influence in determining the mean velocity profiles in transition [9].

Dhawan and Narasimha also give a correlation between the local Reynolds number at transition onset,  $x_t$ , and the Reynolds number based on the parameter  $\lambda$ .

$$Re_\lambda = 5.0 Re_{x_t}^{0.8} \quad (2.24)$$

Due to the universality of the intermittency function, such a relation is helpful in linking the transition extent to the location of the transition onset. Other curves, such as those given by Schubauer and Klebanoff (1955), Abu-Ghannam and Shaw (1980), have also been suggested. However, what makes Eq. 2.21 more favorable is the fact that it is directly related to the spot theory. Such a characteristic make it possible to derive extensions to the equation based on data collected on spot behavior for more complex cases [8].

#### Chen and Thyson:

Chen and Thyson [10] based their work on Emmons' spot theory for predicting the transition and they have suggested an intermittency function in order to achieve a smooth transition from laminar into turbulent flow in the boundary layer. The function, known as  $\Gamma_{tr}$ , is defined as [10]:

$$\Gamma_{tr} = 1 - \exp \left[ -G (x - x_{tr}) \int_{x_{tr}}^x \frac{dx}{u_e} \right] \quad (2.25)$$

where  $x_{tr}$  is the location of the transition onset and the G factor is given empirically by

$$G = \frac{3}{C^2} \frac{u_e^3}{\nu^2} Re_{x_{tr}}^{-1.34} \quad (2.26)$$

where the transition Reynolds number  $Re_{x_{tr}} = (u_e x / \nu)_{tr}$  and C is a constant with a recommended value of 60 [10]. This function,  $\Gamma_{tr}$  was derived for flows over blunt bodies, where the flow experience a large variation of pressure gradient, as opposed to the model given by Dhawan and Narasimha [9], which was based on flow over a flat plate.

**Edwards *et al.*:**

Edwards *et al.* [11] have developed a one-equation turbulence/ transition model that is based on the Spalart-Allmaras one-equation turbulence model and a transition model that was developed by Warren and Hassan [12]. The transport equation of such a model is written as [11]:

$$\begin{aligned} \frac{D\tilde{\nu}}{Dt} = (1 - \Gamma) \tilde{\nu} \Omega \left[ C_\mu \Omega \tau_{nt} - a \frac{\tilde{\nu}}{\sqrt{2\nu}} \right] + C_t \Gamma (1 - \Gamma) \tilde{\nu} \Omega + \\ \Gamma \left[ C_{b1} (1 - f_{t2}) \tilde{\nu} \Omega - \left( C_{w1} f_w - \frac{C_{b1}}{\kappa^2} f_{t2} \right) \left( \frac{\tilde{\nu}}{d} \right)^2 \right] + \\ \frac{\Gamma}{\sigma} C_{b2} (\nabla \tilde{\nu})^2 + \nabla \cdot \left( \frac{1}{\sigma_l} \nu + \frac{1}{\sigma_t} \tilde{\nu} \right) \nabla \tilde{\nu} \end{aligned} \quad (2.27)$$

The intermittency function,  $\Gamma$ , developed by Edwards *et al.* consists of two components, a surface-distance-dependent component  $\Gamma_N(s)$  which is based on the work of Dhawan and Narasimha (Eq. 2.21) and a multidimensional component  $\Gamma_b(x, y)$  developed by the authors that is used to calculate the transition distribution normal to the surface [11]. Then the two components are combined together through the following relation:

$$\Gamma(x, y) = 1 + \Gamma_b(x, y) [\Gamma_N(s) - 1] \quad (2.28)$$

The surface-distance-dependent expression  $\Gamma_N$  is defined along the airfoil surface starting from the stagnation point:

$$\Gamma_N(s) = 1 - \exp(-0.412\xi^2) \quad (2.29)$$

$$\xi = \max(s - s_t, 0) / \lambda \quad (2.30)$$

$$Re_\lambda = 9.0 Re_{s_t}^{-0.75} \quad (2.31)$$

And the boundary-layer localization function  $\Gamma_b$  (normal to the airfoil surface) is defined as:

$$\Gamma_b(x, y) = \tanh(\eta^2) \quad (2.32)$$

$$\eta = \frac{\max[0, \max(t_1, t_2) - t_\infty]}{t_3 + t_\infty} \quad (2.33)$$

$$t_1 = \frac{500\nu}{d^2} \quad (2.34)$$

$$t_2 = \frac{\sqrt{(\nu + \nu_t)\Omega}}{C_\mu^{\frac{3}{2}}d} \quad (2.35)$$

$$t_3 = \sqrt{C_\mu}\Omega \quad (2.36)$$

$$t_\infty \approx 1 * 10^{-7} \frac{U_\infty^2}{\nu_\infty} \quad (2.37)$$

$\Gamma_b$  approaches one near the wall and zero at the edge of the boundary. However for simpler flows, the authors [11] suggest that the multidimensional component can be omitted and thus only  $\Gamma_N$  can be used. So the intermittency function can be simplified to the formula mentioned below with equivalent results.

$$\Gamma(x, y) = \Gamma_N(s) \quad (2.38)$$

but in the case where calculations of transitional flow is performed on complex geometries, and again according to the same paper, the multidimensional component  $\Gamma_b$  should not be neglected.

Concerning intermittency functions of the differential type, these models are more complex and they either require the solution of an independent transport equation, or are integrated inside the turbulence model itself. Thus the solution of such models would involve a considerable effort and time. To give a sample of this type of functions, a brief introduction of two models, Steelant and Dick's model plus that of Cho and Chung, is given below.

#### **Steelant and Dick:**

Steelant and Dick transition model was developed in 1996 and it is to be used in conjunction with conditioned Navier-Stokes equations [13]. Again this model is based on the work of Dhawan and Narasimha. By differentiating Eq. 2.21 along the streamline

direction,  $s$ , the following transport equation is obtained :

$$\frac{\partial \rho \gamma}{\partial t} + \frac{\partial \rho u \gamma}{\partial x} + \frac{\partial \rho v \gamma}{\partial y} = (1 - \gamma) \rho \sqrt{u^2 + v^2} \beta(s) \quad (2.39)$$

where  $\beta(s) = 2f(s)f'(s)$  represents the term  $\frac{(x-x_t)^2 n \sigma}{U}$  in Eq. 2.21. The function  $f(s)$  is to account for the distributed breakdown and is given by:

$$f(s) = \frac{as'^4 + bs'^3 + cs'^2 + ds' + e}{gs'^3 + h} \quad (2.40)$$

where the coefficients are

$$a = \sqrt{\frac{n\sigma}{U}}, \quad b = -0.4906, \quad c = 0.204 \left(\frac{n\sigma}{U}\right)^{-0.5} \quad (2.41)$$

$$d = 0, \quad e = 0.04444 \left(\frac{n\sigma}{U}\right)^{-1.5}, \quad g = 1.0, \quad h = 10e \quad (2.42)$$

and the streamline coordinate is defined as

$$s = \int \frac{u dx + v dy}{\sqrt{u^2 + v^2}} \quad (2.43)$$

and  $s' = s - s_t$ , where  $s_t$  is the location of transition onset. The model was tested by Steelant and Dick in conjunction with two proposed sets of conditioned averaged Navier-Stokes equations for zero, adverse and favorable pressure gradient flows and their results showed that the model performed well for all cases [13].

### Cho and Chung:

Cho and Chung developed a  $k-\epsilon-\gamma$  turbulence model for free shear flows [14]. In the model, the intermittency effect is incorporated into the conventional  $k-\epsilon$  turbulence model equations explicitly by introducing a transport equation for the intermittency factor  $\gamma$ . The eddy viscosity is expressed in terms of  $k$ ,  $\epsilon$  and  $\gamma$ . The intermittency equation is defined as :

$$u_j \frac{\partial \gamma}{\partial x_j} = D_\gamma + S_\gamma \quad (2.44)$$

where the diffusion term ( $D_\gamma$ ) and the source term ( $S_\gamma$ ) are defined as :

$$D_\gamma = \frac{\partial}{\partial x_j} \left[ (1 - \gamma) \frac{\nu_t}{\sigma_g} \frac{\partial \gamma}{\partial x_j} \right] \quad (2.45)$$

$$S_\gamma = C_{g1} \gamma (1 - \gamma) \frac{P_{k,s} + P_{k,n}}{k} + C_{g2} \frac{k^2}{\epsilon} \frac{\partial \gamma}{\partial x_j} \frac{\partial \gamma}{\partial x_j} - C_{g3} \gamma (1 - \gamma) \frac{\epsilon}{k} \Gamma \quad (2.46)$$

and the terms and constants used in the above equations are:

$$P_{k,s} = -\overline{u_i u_j} \frac{\partial u_i}{\partial x_j}, (i \neq j), \quad P_{k,n} = -\overline{u_i u_j} \frac{\partial u_i}{\partial x_j}, (i = j) \quad (2.47)$$

$$\Gamma = \frac{k^{5/2}}{\epsilon^2} \frac{u_i}{(u_k u_k)^{0.5}} \frac{\partial u_i}{\partial x_j} \frac{\partial \gamma}{\partial x_j} \quad (2.48)$$

$$\sigma_g = 1.0, \quad C_{g1} = 1.6, \quad C_{g2} = 0.15, \quad C_{g3} = 0.16 \quad (2.49)$$

As it can be noticed the development of a differential transition model would require the modification of an existing turbulence model in order to incorporate the new feature or the creation of an independent transport equation to solve for the transition variable  $\Gamma$ . In both cases, a considerable effort and time is required.

### **Cebeci Transition Model:**

The CFD solver developed by Cebeci is composed of an inviscid model coupled with a boundary-layer equations model. In order to predict the transition onset, Cebeci alternate between two methods. In the case of high Reynolds numbers, empirical correlation described by Eq. 2.2 is used. And in the case of low Reynolds numbers, the  $e^n$  - *method* is used [3]. Concerning the transition extent, Cebeci uses the intermittency function  $\Gamma_{tr}$  suggested by Chen and Thyson (Eq. 2.25). However, in order for the equation to cover the cases of two-dimensional low Reynolds number flows, especially that separation bubbles increase in such domains, Cebeci has introduced some modifications to the C parameter in Eq. 2.25. It was expressed as a function of the Reynolds number based on onset of transition  $Re_{x_{tr}}$  [15]. Figure 2.3 is a plot of such a variation which is compared to experimental data obtained for airfoils NACA

66-0.28, ONERA-D, NACA 65-218, and LNV109A. The data obtained are for a range of low Reynolds numbers that vary between  $Re_c = 2.4 * 10^5$  and  $2 * 10^6$ . These data can be represented on a semilog scale by a straight line with the following form:

$$C^2 = 213 (\log Re_{x_{tr}} - 4.7323) \quad (2.50)$$

From the material presented in the current chapter, it is concluded that, by using the empirical relations for predicting transition, a major time and effort could be saved in comparison with the percentage accuracy to be gained by using more complex procedures. This conclusion was instrumental in the choice of transition model to use. This model is developed in the next chapter.

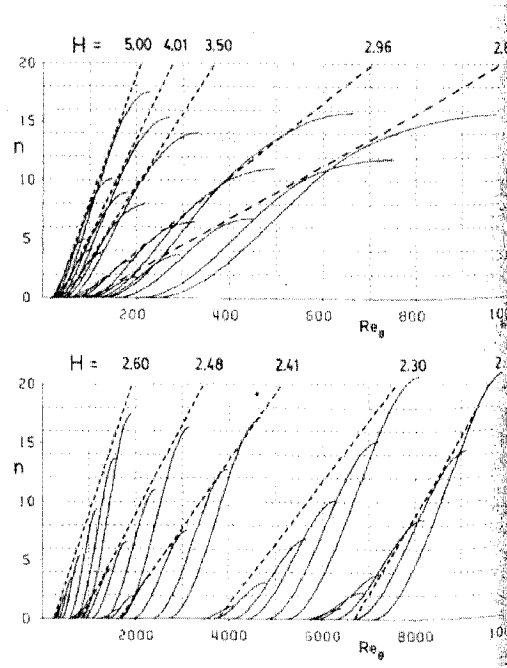


Figure 2.1: Orr-Sommerfeld spatial amplification curves,[Drela and Giles, [7]].



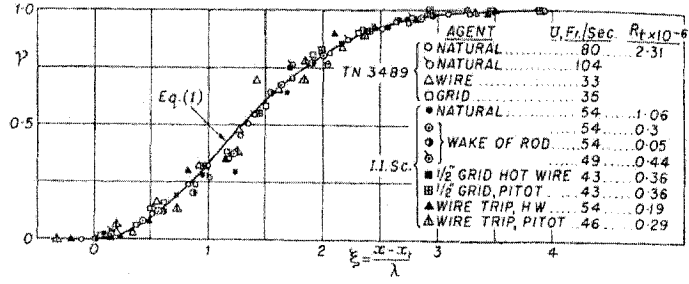


Figure 2.2: Universal distribution of  $\gamma$  vs.  $\xi$  with transition due to different agents, [Dhawan and Narasimha, [9]].

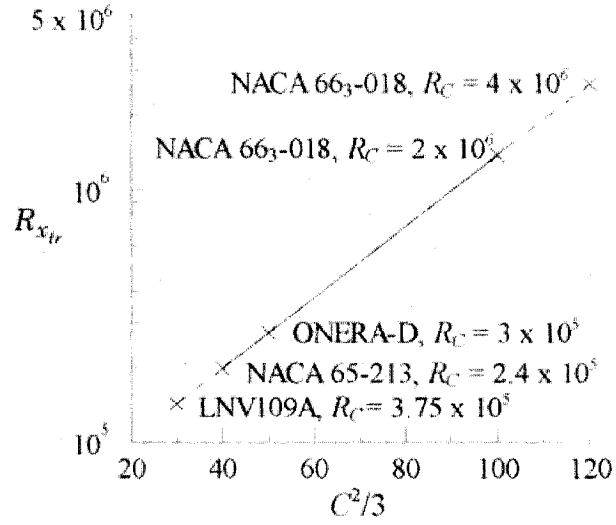


Figure 2.3: Variation of  $C^2/3$  with  $Re_{x_{tr}}$ , [Cebeci, [15]].

## Chapter 3

# Numerical Analysis

Based on the information collected concerning transition analysis and the related methods and procedures that are used in engineering applications, a model for free transition is developed and implemented into the CFD solver, Fluent. After reviewing the different procedures and methods developed to predict transition, let us make the following observations. First, in order to correctly predict the drag coefficient, the chosen method should be able to predict rather accurately the transition onset as well as the intermittency function that would represent the transition zone for typical airfoil sections used in transitional flow. While trying to achieve such an objective, the simplicity and ease of implementing such a procedure in a CFD flow simulation was taken into consideration. Moreover, the model must be inexpensive when it comes to computing time and capabilities.

Fluent, the commercial CFD package, was used in this work to simulate the flow. It includes the CFD solver Fluent 6.1 and the preprocessor Gambit 2.1.6.

The development and implementation of the free transition model is presented in this chapter. This is followed by a parametric study of the effect of the CFD parameters on the drag prediction. These parameters include type and size of mesh used, the solution procedure of governing equations and their discretization, and the

turbulence model used. The chapter is then concluded with a presentation of some of the cases used to evaluate the solver behavior in order to better understand and assess its capabilities.

### 3.1. Free Laminar to Turbulent Transition Model

Transition prediction procedure can be divided into two steps. The first task is to predict the transition onset, and the second is to compute an intermittency function that describes the transition distribution in the boundary layer. Then the procedure is implemented into the flow solver Fluent, where the Spalart-Allmaras (SA) model is used as the turbulence model.

#### 3.1.1 Transition Onset Prediction

In order to predict the transition onset location, the correlation derived by Cebeci and Smith, based on Michel's method, is used. Cebeci and Smith suggested that the following correlation, which is compatible with the  $e^9 - method$ , gives more accurate results than the one given originally by Michel [5, 6]:

$$Re_{\theta_{tr}} \approx 1.174 [1 + (22,400/Re_x)] Re_x^{0.46} \quad (3.1)$$

the Reynolds number based on the momentum thickness,  $Re_\theta$ , and the local Reynolds number,  $Re_x$ , are defined as:

$$Re_\theta = \frac{u_e \theta}{\nu} \quad (3.2)$$

$$Re_x = \frac{u_e x}{\nu} \quad (3.3)$$

where  $u_e$  is the velocity at the boundary layer edge.

Equation 3.1 is derived for attached flows on airfoils for chord Reynolds numbers greater than  $2 * 10^6$  and it is based on incompressible fluid flow properties. The momentum thickness,  $\theta$ , is calculated using Thwaites Method [16]. The equation

derived by Thwaites, which he based on the integral momentum equation, is defined as [16]:

$$\theta^2 \approx \frac{0.45\nu}{u_e^6} \int_0^x u_e^5 dx \quad (3.4)$$

Using Eq. 3.4, Thwaites has proved that  $\theta(x)$  can be predicted with an accuracy of  $\pm 3\%$  for most types of incompressible laminar boundary layer flows [6]. The inviscid velocity profile along the wall,  $u_e$ , is computed by solving the Euler equations using Fluent.

### 3.1.2 Transition Zone Prediction

Now that the transition onset is known, the next step is to model the transition zone. This is done by using an intermittency function that will divide the flow domain into three zones: the laminar zone with a corresponding intermittency function value of zero, the fully turbulent zone with a value of one and the transition zone that will have a value ranging from zero at the beginning of transition to one where the flow becomes fully turbulent.

The intermittency function used in the current work is a combination of two components, a surface-distance-dependent one  $\Gamma_x$  and a normal-distance-dependent one  $\Gamma_b$ . The two components are blended together through the following equation:

$$\Gamma(x, y) = 1 + \Gamma_b [\Gamma_x - 1] \quad (3.5)$$

To evaluate  $\Gamma_x$ , the function developed by Chen and Thyson [10], with taking into account the modifications added later by Cebeci [15] to account for the separation bubbles at lower Reynolds numbers, is used. Thus the function used to compute  $\Gamma_x$  is defined as [10]:

$$\Gamma_x = 1 - \exp \left[ -G (x - x_{tr}) \int_{x_{tr}}^x \frac{dx}{u_e} \right] \quad (3.6)$$

where the factor  $G$  is given as:

$$G = \frac{3}{C^2} \frac{u_e^3}{\nu^2} Re_{x_{tr}}^{-1.34} \quad (3.7)$$

and the parameter  $C$  is replaced by the term suggested by Cebeci [15]:

$$C^2 = 213 (\log Re_{x_{tr}} - 4.7323) \quad (3.8)$$

where  $Re_{x_{tr}}$  is the Reynolds number at transition onset location ( $x_t$ ) and  $u_e$ , defined as the velocity at the boundary layer edge, is replaced by inviscid velocity values computed by solving Euler equations using Fluent.

On the other hand, the normal-distance-dependent term  $\Gamma_b$  is evaluated based on the work of Edwards et al. [11]. Thus the equations used in the current work are [11]:

$$\Gamma_b = \tanh(\eta^2) \quad (3.9)$$

where  $\eta$  is defined as:

$$\eta = \frac{\max[0, \max(t_1, t_2) - t_\infty]}{t_3 + t_\infty} \quad (3.10)$$

The terms used in evaluating  $\eta$  are defined as:

$$t_1 = \frac{500\nu}{d^2} \quad (3.11)$$

$$t_2 = \frac{\sqrt{(\nu + \nu_t)\Omega}}{C_\mu^{\frac{3}{2}}d} \quad (3.12)$$

$$t_3 = \sqrt{C_\mu\Omega} \quad (3.13)$$

and

$$t_\infty \approx 1 * 10^{-5} \frac{U_\infty^2}{\nu_\infty} \quad (3.14)$$

where  $C_\mu$  is a model constant equal to 0.11. The values of  $C_\mu$  and  $t_\infty$  have been modified so as to match the CFD discretization method used in Fluent.

The transition model is then implemented into the flow solver, Fluent, where the RANS equations are solved with the Spalart-Allmaras turbulence model and the intermittency function,  $\Gamma(x, y)$ , is introduced using the User-Defined-Function (UDF) feature that is available in Fluent. This function gives access to different variables in the flow solver and thus allows for modifying them [17]. The turbulent

viscosity  $\mu_t$ , computed using the fully turbulent Spalart-Allmaras turbulence model, is multiplied by the intermittency function in order to reflect the introduction of the laminar and the transition zones into the fully turbulent boundary layer. Thus the modified effective viscosity  $\mu_{eff}$  is computed as:

$$\mu_{eff} = \mu_L + (\Gamma * \mu_t) \quad (3.15)$$

where  $\mu_L$  is the laminar viscosity.

## 3.2. Description of The Computational Domain

The airfoil geometry, the computational domain and the mesh used for numerical flow simulation were generated using Fluent preprocessor, Gambit. The software allows the usage of rectangular and triangular elements. When analyzing external flow over two-dimensional airfoils, the general routine is to use an O-type or a C-type computational domain where the airfoil is at the center of a circle that extends between 20c and 50c out, c being the chord length. A sample of a structured O-type and C-type meshes are shown in Figs. 3.1 and 3.2, respectively. Hybrid meshes are also used to perform CFD analysis. A hybrid mesh is a combinations of both structured elements (rectangular cells) that are usually constructed around the airfoil and unstructured elements (triangular cells) that fill the remaining part of the computational domain. Figure 3.3 shows a hybrid mesh constructed around the NLF-0416 airfoil. In the current study, a variety of mesh types were used depending on the purpose of the analysis to be carried out. Two boundary conditions are involved in this problem: The airfoil surface is defined as a wall, and the outer boundary is defined as a characteristic boundary. Wall boundary conditions are used to bound fluid and solid regions. In inviscid simulations where the flow is assumed to slip along the wall surface,  $\vec{V} \cdot \vec{n} = 0$ . For viscous flows, the no-slip boundary condition is enforced at walls and thus  $\vec{V} = 0$ . Characteristic boundary condition, which are named in Fluent as pressure

far-field boundary conditions, is a non-reflecting boundary condition that uses the Riemann invariants to determine the flow variables at the boundaries. It is used to model free-stream conditions at infinity, with free-stream Mach number and static conditions being specified ([17]). For flow that is subsonic there are two Riemann invariants, corresponding to incoming and outgoing waves:

$$R_{\infty} = v_{n\infty} - \frac{2c_{\infty}}{\gamma - 1} \quad (3.16)$$

and

$$R_i = v_{ni} + \frac{2c_i}{\gamma - 1} \quad (3.17)$$

where  $v_n$  is the velocity magnitude normal to the boundary,  $c$  is the local speed of sound and  $\gamma$  is the ratio of specific heats (ideal gas). The subscript  $\infty$  refers to conditions being applied at infinity (the boundary conditions), and the subscript  $i$  refers to conditions in the interior of the domain (i.e., in the cell adjacent to the boundary face). These two invariants can be added and subtracted to give the following two equations:

$$v_n = \frac{1}{2}(R_i + R_{\infty}) \quad (3.18)$$

and

$$c = \frac{\gamma - 1}{4}(R_i - R_{\infty}) \quad (3.19)$$

where  $v_n$  and  $c$  become the values of normal velocity and sound speed applied on the boundary. At a face through which flow exits, the tangential velocity components and entropy are extrapolated from the interior. At an inflow face, these are specified as having free-stream values.

When performing numerical analysis, the grid used plays an important role in the quality of the variables being computed. Such an effect is governed mainly by the mesh's density and concentration areas and the mesh's quality.

### **Mesh Quality:**

The mesh quality has a significant impact on the numerical solution accuracy. The quality can be measured by two major criteria, smoothness and element skewness. Mesh smoothness is used to describe the change ratio in area for a two-dimensional mesh. Such a change has to be gradual and any jumps in the size ratio have to be avoided especially in areas where the flow undergoes critical changes or where the flow gradients are high. The other aspect of mesh quality is the elements skewness. Skewness can be measured, in Gambit, by the equiangle skewness check for two-dimensional elements. Such properties compare the cells under examination to a similar equilateral cell. A value of 0 indicates that the cell is equilateral and a value of 1 is given for collapsed cells or in other words for cells with coplanar nodes. Even though in some cases it is impossible to eliminate all the skewed elements in a mesh, one must always try to lower the number of highly skewed elements.

### **Mesh Density:**

It is obvious that the smaller the cells size is, the better the numerical results are. However, this is accompanied by penalties that have to be carefully assessed in order to optimize the output of the computations. First, the computational time is proportional to the number of cells used and thus this would become increasingly expensive as the number of cells increases. The second drawback is the increase in numerical error associated with the discretization method and solver schemes used. On the other hand and in order to fully capture the different flow phenomena a dense mesh is a must. So a compromise has to be done when building the mesh and choosing the number of cells. One way to do this is to vary the mesh density along the computational domain. Thus one would have more cells where gradients are large, e.g. viscous effects near the wall and would use a much coarser cell distribution where there is no change in flow properties. Therefore, nodes are clustered in the vicinity of the leading



and trailing edge where pressure gradients are relatively higher, downstream of the trailing edge in order to capture the wake, and near the airfoil surface in order to fully capture the boundary layer and the viscous properties associated with it. A coarser mesh can be used at the outer boundary area and far away from the airfoil due to the fact that flow properties are more uniform, property gradients are relatively low and viscous effects are negligible.

### **Mesh Considerations For Turbulent Flow Simulations:**

Due to the important role that turbulence plays in the transport of mean momentum and other scalars, it is essential that the turbulence quantities be properly computed so that high accuracy is achieved. This would involve the usage of a fine mesh that would fully resolve the viscous-affected regions. The parameter  $y^+$ , which is function of the distance of the first cell away from the wall, is useful in checking if the mesh that is used is capable of properly capturing the turbulent properties properly. However, different turbulence models with different near-wall options within these models would necessitate different mesh density near the wall region. Thus when constructing a "viscous" mesh, it has to be kept in mind the turbulence model, and thus the wall treatment functions, that will be used. This will put forward the distance of the first cell from the wall to be used (A discussion of the suggested  $y^+$  values to be used with the Spalart-Allmaras turbulence model is given in Sec. 3.5).  $y^+$  is a non-dimensional parameter defined by the following equation:

$$y^+ = \frac{\rho u_\tau y_p}{\mu} \quad (3.20)$$

where  $u_\tau$  is the friction velocity,  $y_p$  is the distance from point p, and  $\rho$  and  $\mu$  are the fluid density and viscosity at point p, respectively.

In the results presented in the current work, mesh features such as quality, density and distance from the wall are taken into account when generating the computational domain. This will minimize the numerical error related to the grid been

used and ensure that the solution is grid-independent.

### 3.3. Flow Solver Description

Fluent solver offers a wide variety of options to simulate the real flow conditions as close as possible. The solver could be chosen to be segregated (implicit) or coupled (explicit or implicit). The fluid can be simulated as 2D/3D, compressible/incompressible, inviscid/viscous (Laminar and turbulent), with the choice between Spalart-Allmaras  $k - \epsilon$   $k - \omega$  /Reynolds Stress as a turbulence model. In the present study, the flow is an external compressible air flow which is represented by the Navier-Stokes conservation equations described below. Simulations were performed using the compressible, viscous flow properties and Spalart-Allmaras as the turbulence model.

#### 3.3.1 Navier-Stokes Equations

The compressible viscous flow can be described through a set of three equations known as the conservation equations. Below is the general vectorial form of these equations as it is implemented into Fluent [17].

##### The Mass Conservation Equation:

The equation for conservation of mass, or continuity equation, can be written as follows:

$$\frac{\partial \rho}{\partial t} + \nabla \cdot (\rho \vec{v}) = S_m \quad (3.21)$$

The source term  $S_m$  is the mass added to the continuous phase from the dispersed second phase and/or any user-defined sources. The simplified form of the continuity equation is given as:

$$\frac{\partial}{\partial x_j} (\rho u_j) = 0 \quad (3.22)$$

### The Momentum Conservation Equation:

Conservation of momentum in an inertial (non-accelerating) reference frame is described by:

$$\frac{\partial}{\partial t} (\rho \vec{v}) + \nabla \cdot (\rho \vec{v} \vec{v}) = -\nabla p + \nabla \cdot (\bar{\bar{\tau}}) + \rho \vec{g} + \vec{F} \quad (3.23)$$

where  $p$  is the static pressure,  $\bar{\bar{\tau}}$  is the stress tensor, and  $\rho \vec{g}$  and  $\vec{F}$  are the gravitational body force and external body forces respectively.  $\vec{F}$  also contains other model-dependent source terms such as user-defined sources. The stress tensor  $\bar{\bar{\tau}}$  is given by:

$$\bar{\bar{\tau}} = \nabla \left[ (\nabla \vec{v} + \nabla \vec{v}^T) - \frac{2}{3} \nabla \cdot \vec{v} I \right] \quad (3.24)$$

where  $\mu$  is the molecular viscosity,  $I$  is the unit tensor, and the second term on the right hand side is the effect of volume dilation. Again in the simplified format, the momentum equation will become:

$$\frac{\partial}{\partial x_j} (\rho u_i u_j) = -\frac{\partial p}{\partial x_i} + \frac{\partial}{\partial x_j} \left( \mu \frac{\partial u_i}{\partial x_j} - \rho \overline{u'_i u'_j} \right) \quad (3.25)$$

### The Energy Equation:

The energy equation is given in the following form:

$$\frac{\partial}{\partial t} (\rho E) + \nabla \cdot (\vec{v} (\rho E + p)) = \nabla \cdot \left( k_{eff} \nabla T - \sum_j h_j \vec{J}_j + (\bar{\bar{\tau}}_{eff} \cdot \vec{v}) \right) + S_h \quad (3.26)$$

where  $k_{eff}$  is the effective conductivity ( $k + k_t$ , where  $k_t$  is the turbulent thermal conductivity, defined according to the turbulence model being used), and  $\vec{J}_j$  is the diffusion flux of species  $j$ . The first three terms on the right-hand side of Eq. 3.26 represent energy transfer due to conduction, species diffusion, and viscous dissipation, respectively.  $S_h$  includes the heat of chemical reaction, and any other volumetric heat sources been defined. In Eq. 3.26

$$E = h - \frac{p}{\rho} + \frac{v^2}{2} \quad (3.27)$$

where enthalpy  $h$  is defined for ideal gases as

$$h = \sum_j Y_j h_j \quad (3.28)$$

and for incompressible flows as

$$h = \sum_j Y_j h_j + \frac{p}{\rho} \quad (3.29)$$

In Eqs. 3.28 and 3.29,  $Y_j$  is the mass fraction of species  $j$  and

$$h_j = \int_{T_{ref}}^T c_{p,j} dT \quad (3.30)$$

where  $T_{ref}$  is 298.15 K.

The simplified form of the energy equation is:

$$\frac{\partial}{\partial x_j} (\rho T u_j) = \frac{\partial}{\partial x_j} \left( \frac{\mu}{Pr} \frac{\partial T}{\partial x_j} - \rho \theta u_j' \right) \quad (3.31)$$

### 3.3.2 Euler Equations

For inviscid flow, a simplified form of the conservation equations, which is known as the Euler equations, is solved. These equations neglect the viscous effect, and it is usually used in cases where the viscous forces are not of interest or where these forces are much less than those of the inertial ones. The mass conservation equation is the same as for a viscous flow, but the momentum and energy conservation equations are reduced due to the absence of molecular diffusion.

#### The Momentum Conservation Equation:

The conservation of momentum is described by:

$$\frac{\partial}{\partial t} (\rho \vec{v}) + \nabla \cdot (\rho \vec{v} \vec{v}) = -\nabla p + \rho \vec{g} + \vec{F} \quad (3.32)$$

### The Energy Equation:

Conservation of energy is described by:

$$\frac{\partial}{\partial t}(\rho E) + \nabla \cdot (\vec{v}(\rho E + p)) = -\nabla \cdot \left( \sum_j h_j J_j \right) + S_h \quad (3.33)$$

## 3.4. Discretization of The Governing Equations

Fluent is a control-volume solver that discretizes the governing flow equations, in the conservative form, into algebraic equations in order to be solved numerically. In this work, the implicit-coupled solver was used through out all the simulations performed. The governing equations are solved simultaneously using the coupled solver where flow variables are stored at the cell centers. The second-order upwind scheme was used for solving the flow equations.

### Governing Equations in Vector Form:

The system of governing equations, that describes a fluid entity in the computational domain, are written for a control volume  $V$  with differential surface area  $dA$  in the following form:

$$\frac{\partial}{\partial t} \int_V W dV + \oint [F - G] \cdot dA = \int_V H dV \quad (3.34)$$

where the vectors  $W$ ,  $F$ , and  $G$  are defined as

$$W = \begin{pmatrix} \rho \\ \rho u \\ \rho v \\ \rho \omega \\ \rho E \end{pmatrix}, \quad F = \begin{pmatrix} \rho \mathbf{v} \\ \rho \mathbf{v} u + p \hat{i} \\ \rho \mathbf{v} v + p \hat{j} \\ \rho \mathbf{v} \omega + p \hat{k} \\ \rho \mathbf{v} E + p \mathbf{v} \end{pmatrix}, \quad G = \begin{pmatrix} 0 \\ \tau_{xi} \\ \tau_{yi} \\ \tau_{zi} \\ \tau_{ij} v_j + \mathbf{q} \end{pmatrix} \quad (3.35)$$

and the vector  $\mathbf{H}$  contains source terms such as body forces and energy sources. Here  $\rho$ ,  $\mathbf{v}$ ,  $E$ , and  $p$  are the density, velocity, total energy per unit mass, and pressure, respectively.  $\tau$  is the viscous stress tensor, and  $\mathbf{q}$  is the heat flux vector.

The total energy  $E$  and total enthalpy  $H$  are related by the following formula:

$$E = H - p/\rho \quad (3.36)$$

where  $H = h + |\mathbf{v}|^2/2$ .

In the case of low Mach number, the Navier-Stokes equations described above (Eq. 3.34) become numerically stiff and will lead to poor convergence rates. Such a problem is overcome by including time-derivative preconditioning in the coupled solver.

### 3.5. The Turbulence Model

When random fluctuations occur in the velocity field, flow is said to be turbulent, or at least it is starting to turn turbulent. Such a behavior in the velocity will definitely be translated as fluctuations in the transported quantities such as momentum and energy. These fluctuations are known to be of small scale and high frequency which make it difficult to simulate through a system of equations that is easy and computationally inexpensive to solve. Thus in order to overcome such a problem, the instantaneous governing equations are modified through introducing a new set of variables and thus turbulence models are needed in order to solve for those additional quantities.

However, when it comes to modelling turbulence, it is impossible to assign a specific turbulence model as the one suitable for all kinds of flow problems. This could be related to the fact that those models were developed for a specific type of problems or with certain limitations. Thus when it comes to choosing a turbulence model, a full understanding of the various models available with their potentials and limitations is essential. Also the flow physics to be covered should be investigated.

Such a knowledge is essential such that a better choice of turbulence model is made.

FLUENT provides the option to chose one of the following turbulence models (for two-dimensional cases):

- Spalart-Allmaras model
- $k - \epsilon$  models
  - Standard  $k - \epsilon$  model
  - Renormalization-group (RNG)  $k - \epsilon$  model
  - Realizable  $k - \epsilon$  model
- $k - \omega$  models
  - Standard  $k - \omega$  model
  - Shear-stress transport (SST)  $k - \omega$  model
- Reynolds stress model (RSM)

### 3.5.1 The Spalart-Allmaras Turbulence Model

The Spalart-Allmaras is a one equation turbulence model that solves a transport equation for the turbulent (eddy) viscosity. It was based on empiricism and arguments of dimensional analysis, Galilean invariance and selective dependence on the molecular viscosity. It was developed specifically for aerospace applications involving wall-bounded flows and it gives good results for boundary layers with adverse pressure gradients [18]. Even though the original model developed by Spalart and Allmaras included a transition terms where the transition onset has to be specified by the user, the model used by Fluent is fully turbulent. Another modification added by Fluent is concerning the mesh resolution in the boundary layer region. In the original model, it is essential that the viscous affected regions in the boundary layer to be

resolved properly due to the fact that the model was developed as a low Reynolds number model. However in Fluent, the model was adjusted to use wall functions in case the mesh being used isn't fine enough in such regions. Thus if the accuracy of the turbulent flow computations is not critical, a coarser mesh could be used [17, 18].

### The Transport Equation:

The actual variable solved by the Spalart-Allmaras transport equation is not the turbulent viscosity itself but a modified form of it. This transported variable,  $\tilde{\nu}$ , is identical to the turbulent kinematic viscosity except in the near-wall region where viscous effects become effective. The transport equation for  $\tilde{\nu}$  is written as [17]:

$$\frac{\partial}{\partial t}(\rho\tilde{\nu}) + \frac{\partial}{\partial x_i}(\rho\tilde{\nu}u_i) = G_\nu + \frac{1}{\sigma_{\tilde{\nu}}} \left[ \frac{\partial}{\partial x_j} \left\{ (\mu + \rho\tilde{\nu}) \frac{\partial \tilde{\nu}}{\partial x_j} \right\} + C_{b2}\rho \left( \frac{\partial \tilde{\nu}}{\partial x_j} \right)^2 \right] - Y_\nu + S_{\tilde{\nu}} \quad (3.37)$$

where  $G_\nu$  is the production term of the turbulent viscosity and  $Y_\nu$  is the destruction term that occurs in the near-wall region due to wall blocking and viscous damping.  $\sigma_{\tilde{\nu}}$  and  $C_{b2}$  are constants and  $\nu$  is the molecular kinematic viscosity.  $S_{\tilde{\nu}}$  is a user-defined source term.

### Modeling The Turbulent Viscosity:

The turbulent viscosity,  $\mu_t$ , and the modified kinematic viscosity,  $\tilde{\nu}$ , are related by the following form [17]:

$$\mu_t = \rho\tilde{\nu}f_{\nu1} \quad (3.38)$$

where the viscous damping function,  $f_{\nu1}$ , is given by:

$$f_{\nu1} = \frac{\chi^3}{\chi^3 + C_{\nu1}^3} \quad (3.39)$$



and

$$\chi \equiv \frac{\tilde{\nu}}{\nu} \quad (3.40)$$

$C_{\nu 1}$  is a constant.

### Modeling The Turbulent Production:

The production term,  $G_\nu$ , is modelled as [17]:

$$G_\nu = C_{b1} \rho \tilde{S} \tilde{\nu} \quad (3.41)$$

where

$$\tilde{S} \equiv S + \frac{\tilde{\nu}}{\kappa^2 d^2} f_{\nu 2} \quad (3.42)$$

and

$$f_{\nu 2} = 1 - \frac{\chi}{1 + \chi f_{\nu 1}} \quad (3.43)$$

$C_{b1}$  and  $\kappa$  are constants,  $d$  is the distance from the wall, and  $S$  is a scalar measure of the deformation tensor. By default in Fluent, as in the original model proposed by Spalart and Allmaras,  $S$  is based on the magnitude of the vorticity [17, 18]:

$$S \equiv \sqrt{2\Omega_{ij}\Omega_{ij}} \quad (3.44)$$

where  $\Omega_{ij}$  is the mean rate-of-rotation tensor and is defined by:

$$\Omega_{ij} = \frac{1}{2} \left( \frac{\partial u_i}{\partial x_j} - \frac{\partial u_j}{\partial x_i} \right) \quad (3.45)$$

The justification for the default expression for  $S$  is that, for the wall-bounded flows that were of most interest when the model was formulated, turbulence is found only where vorticity is generated near walls. However, it has since been acknowledged that one should also take into account the effect of mean strain on the turbulence production, and a modification to the model has been proposed and incorporated into Fluent. This modification combines measures of both rotation and strain tensors in the definition of  $S$ :

$$S \equiv |\Omega_{ij}| + C_{prod} \min(0, |S_{ij}| - |\Omega_{ij}|) \quad (3.46)$$

where  $C_{prod} = 2.0$ ,  $|\Omega_{ij}| \equiv \sqrt{2\Omega_{ij}\Omega_{ij}}$ ,  $|S_{ij}| \equiv \sqrt{2S_{ij}S_{ij}}$   
with the mean strain rate,  $S_{ij}$ , is defined as

$$S_{ij} = \frac{1}{2} \left( \frac{\partial u_j}{\partial x_i} + \frac{\partial u_i}{\partial x_j} \right) \quad (3.47)$$

### Modeling The Turbulent Destruction:

The destruction term is modelled as [17]:

$$Y_\nu = C_{w1} \rho f_w \left( \frac{\tilde{\nu}}{\bar{d}} \right)^2 \quad (3.48)$$

where

$$f_w = g \left[ \frac{1 + C_{w3}^6}{g^6 + C_{w3}^6} \right]^{1/6} \quad (3.49)$$

$$g = r + C_{w2} (r^6 - r) \quad (3.50)$$

$$r \equiv \frac{\tilde{\nu}}{\tilde{S} \kappa^2 d^2} \quad (3.51)$$

$C_{w1}$ ,  $C_{w2}$  and  $C_{w3}$  are constants, and  $\tilde{S}$  is given by Eq. 3.42.

### Model Constants:

The model constants  $C_{b1}$ ,  $C_{b2}$ ,  $\sigma_{\tilde{\nu}}$ ,  $C_{\nu 1}$ ,  $C_{w1}$ ,  $C_{w2}$ ,  $C_{w3}$ , and  $\kappa$  have the following default values [17]:

$$\begin{aligned} C_{b1} &= 0.1355, & C_{b2} &= 0.622, & \sigma_{\tilde{\nu}} &= \frac{2}{3}, & C_{\nu 1} &= 7.1 \\ C_{w1} &= \frac{C_{b1}}{\kappa^2} + \frac{(1+C_{b2})}{\sigma_{\tilde{\nu}}}, & C_{w2} &= 0.3, & C_{w3} &= 2.0, & \kappa &= 0.4187 \end{aligned}$$

### Wall Boundary Conditions:

At walls the modified turbulent kinematic viscosity,  $\tilde{\nu}$ , is set to zero. In the case of a fine mesh where the laminar sub-layer is completely resolved, then the wall shear stress is calculated using the laminar stress-strain relationship:

$$\frac{u}{u_\tau} = \frac{\rho u_\tau y}{\mu} \quad (3.52)$$

On the other hand, if the laminar sub-layer isn't resolved due to the usage of a coarse mesh, then it is assumed that the centroid of the wall-adjacent cell falls within the logarithmic region of the boundary layer, and the law-of-the-wall is used:

$$\frac{u}{u_\tau} = \frac{1}{\kappa} \ln E \left( \frac{\rho u_\tau y}{\mu} \right) \quad (3.53)$$

where  $u$  is the velocity parallel to the wall,  $u_\tau$  is the shear velocity,  $y$  is the distance from the wall,  $\kappa$  is the von Karman constant (0.4187) and  $E = 9.793$ .

### Near-Wall Mesh Guidelines for The Spalart-Allmaras Model:

In order to capture the laminar sublayer and the turbulent properties calculated by the Spalart-Allmaras model, a mesh that comply with the guidelines suggested by Fluent documentation is preferred. These directions are related to the distance of the first cell center from the wall and they are defined by the parameter  $y^+$ . These suggestions can be summed up as [17]:

- In order to resolve the laminar sublayer,  $y^+$  at the wall-adjacent cell should be on the order of  $y^+ \approx 1$ . However, a higher  $y^+$  is acceptable as long as it is well inside the viscous sublayer ( $y^+ < 4$  to 5).
- At least 10 cells should be included within the viscosity-affected near-wall region ( $Re_y < 200$ ) to be able to resolve the mean velocity and turbulent quantities in that region.

But, and as it has been mentioned before, the original Spalart-Allmaras model has been adjusted to accommodate coarser meshes by the introduction of wall functions. So if a coarser mesh is used, then the subsequent guidelines can be followed [17]:

- The log-law is valid for values of  $y^+$  between 30 and 60.

- The upper bound of the log-layer depends on, among others, pressure gradients and Reynolds number. As the Reynolds number increases, the upper bound tends to also increase.  $y^+$  values that are too large are not desirable, because the wake component becomes substantially large above the log-layer.
- A  $y^+$  value close to the lower bound ( $y^+$  approx. 30) is most desirable.
- It is important to have at least a few cells inside the boundary layer.

### 3.6. Convergence to Steady State

The residual is an indicator of a solutions convergence. For a simulation to be fully converged, the residuals have to be zero. The residual for the coupled solvers is defined, in Fluent, as the time rate of change of the conserved variable (W). The RMS residual is thus the square root of the average of the squares of the residuals in each cell of the domain and is represented by the following equation [17]:

$$R(W) = \sqrt{\sum \left( \frac{\partial W}{\partial t} \right)^2} \quad (3.54)$$

However, this equation is the unscaled residual sum reported for all the coupled equations solved by the coupled solver in Fluent [17]. This would make it difficult to judge convergence. Thus a scaling option defined by the subsequent equation is supplied.

$$\frac{R(W)_{iteration \ N}}{R(W)_{iteration \ 5}} \quad (3.55)$$

The denominator is the largest absolute value of the residual in the first five iterations. Fluent also give the option of normalizing the residual value, which is a measure of how much a residual has decreased during calculations [17]. Residual scaling and normalization are better indicators of solution convergence than the standard equation (Eq. 3.54). Normalization is achieved by dividing the residual by the

maximum residual value after M iterations:

$$\frac{\overline{R}(W)_{iteration\ N}}{R(W)_{iteration\ M}} \quad (3.56)$$

After each iteration, the residual for each of the conserved variables is calculated. On an ideal computer, these residuals are supposed to go to a zero value as the solution converges. However on an actual computer, the residual decreases to a very small value and then it levels out. For single precision computations, such a value would be of six orders of magnitude drop, while on a double precision computations it could reach up to twelve orders of magnitude drop. For the cases presented in the current work, a double precision setup was used and the residual was monitored until convergence is achieved. For most of the simulations presented in this work, the residual would drop about eight to ten orders.

### 3.7. Numerical Assessment of Fluent for The NACA-0012 Airfoil

Several simulations were carried out assuming fully turbulent flow to observe the behavior of the CFD solver, Fluent, under different conditions and thus achieve a better understanding of the solver capabilities. In the cases considered, certain parameters of the simulation problem were varied while keeping others fixed in order to assess the solver sensitivity to such variables. Analysis can be categorized into three sections: an assessment of the mesh type, an assessment of the turbulence model and a grid sensitivity study.

#### 3.7.1 Mesh Type Assessment

The first task was to evaluate the dependency of the results computed on the type of mesh used. To do so, three different types of mesh were constructed on a NACA-0012

airfoil, namely a structured O-mesh, a structured C-mesh and a hybrid mesh. Even though great care was taken in order to make sure that all the three meshes have exactly the same number of cells and characteristics, certain discrepancies could not be avoided. This is due to the fact that each type of mesh has certain parameters and constraints that have to be taken into account in order to achieve a smooth and coherent computational grid. The number of nodes on the airfoil surface is sixty on each side of the airfoil with a bell shape distribution of ratio equal to 0.65. Also the distance of the first cell from the airfoil surface is equal to  $10^{-4}$  chord. It is to be noted that when constructing the hybrid mesh, the structured boundary layer mesh around the airfoil was extended for about 25 % of the chord length at the trailing edge with a slope parallel to the trailing edge's slope. Thus the airfoil is surrounded by a structured C-mesh (see Fig. 3.3 for more details). This method is repeated for all the hybrid meshes used in the current work. The reason behind such a choice was to enable the solver to capture the viscous effects and the wake downstream of the airfoil.

The experimental data used for the NACA0012 case were obtained from a wind tunnel experiment at the Langley Low-Turbulence Pressure Tunnel (NASA) [19]. The data available in the report are those of the following free-stream conditions: Mach number is equal to 0.15 and a set of Reynolds number equal to  $2 * 10^6$ ,  $4 * 10^6$  and  $6 * 10^6$ . The angle of attack varies between  $-4^\circ$  and  $16^\circ$ . The numerical simulations carried out using Fluent were performed for a Reynolds number equal to  $2 * 10^6$  and a Mach number of 0.15 and over a range of angle of attacks varying between  $-4^\circ$  and  $20^\circ$ . Table 3.1 gives a summary of the free-stream conditions of both the experimental and numerical data. The turbulence model used is that of Spalart-Allmaras, the fully turbulent version.

Figures 3.4 and 3.5 represent the variation in the lift and drag coefficients, respectively, with the angle of attack. Comparing the lift values computed numerically

and those obtained experimentally (Fig. 3.4), the following comments can be pointed out. First, the lift coefficient predicted numerically, for the three different meshes used, matches well the values given experimentally for  $\alpha \leq 8^\circ$ . However, at higher angles of attack the difference between experimental and numerical values reaches a maximum of 8% at  $C_{L,max}$ . While the numerical model under-predicts  $C_{L,max}$ , the location of the maximum lift is delayed by about two degrees and the stall region is smoother than the one obtained experimentally. Comparing the numerical values obtained by the three different meshes used, the agreement between the data obtained is evident where the difference between the three curves is less than one percent throughout the whole range of angles of attack considered.

Analyzing the drag coefficient variations with the angle of attack (Fig. 3.5), the difference between the experimental and numerical data and also among the three sets of numerical data is bigger than the differences observed in the lift coefficient case (Fig. 3.4). Again at low angles of attack the corresponding data are closer than those obtained at high angles of attack. The difference between experimental and numerical data is as close as 0.5 % at an angle of attack of zero and it increases up to a maximum of 25 % at higher angles of attack. By comparing the sets of data computed numerically for each of the three meshes used, the difference between those sets is on an average of 4 % at low angles of attack and about 10 % at high angles of attack with those obtained by the hybrid mesh been the closet to the experimental data and the ones obtained by the structured C-mesh been the farthest. The minimum difference

	Experimental upstream flow conditions	Numerical upstream flow conditions
Mach Number	0.15	0.15
Reynolds Number	$2 * 10^6$ , $4 * 10^6$ and $6 * 10^6$	$2 * 10^6$
Alpha	$-4^\circ$ to $16^\circ$	$-4^\circ$ to $20^\circ$
Transition conditions	Fixed at 0.07c	Fully turbulent

Table 3.1: Experimental and numerical free-stream flow conditions for the NACA-0012 case.

between the numerical data computed using the hybrid mesh and the experimental data is equal to 0.37% at angle of attack equal to  $0^\circ$ . And the maximum is at angle of attack of  $13^\circ$  and it is about 13%. The discrepancy in numerical data obtained could be related to the fact that when constructing the structured boundary layer mesh in the hybrid mesh using Gambit, more control can be achieved on the quality of the cells in the boundary layer domain. Thus the boundary layer flow and the related viscous effects could be better resolved using such a mesh.

### 3.7.2 Turbulence Model Assessment

The next step was to assess the effectiveness of choosing the Spalart-Allmaras model as the turbulence model. In order to do so, the two-equation turbulence model  $k - \epsilon$  was used. Fluent offers the choice between the standard  $k - \epsilon$  model and two modified versions of the model, namely the Renormalization group (RNG) model and the Realizable model. The mesh used in the current evaluation is the same hybrid O-mesh used in the previous section (Sec. 3.7.1). Also the free-stream conditions are set with the same conditions mentioned in Table 3.1. Figures 3.6 and 3.7 below compare the lift and drag coefficient variation with respect to the angle of attack for the Spalart-Allmaras, standard  $k - \epsilon$  and the RNG  $k - \epsilon$  models beside those given experimentally. From Fig. 3.6, the lift coefficient computed by the standard  $k - \epsilon$  model matches those computed by the Spalart-Allmaras model. However, for  $\alpha \geq 10^\circ$ , the values obtained using the Spalart-Allmaras model are closer to the experimental data from those obtained by the other two models. On the other hand, the lift coefficient computed by the RNG  $k - \epsilon$  model have the largest mismatch with the experimental values. Plus the difference between the latter model and the other two sets of numerical data is on the average of 5% at the low range of angles of attack and the it grows larger near the stall angle. Concerning the drag coefficient variations, the values computed using the RNG  $k - \epsilon$  model matches the Spalart-Allmaras model at low angles of



attack ( $\alpha \leq 10^\circ$ ) while those obtained using the standard  $k - \epsilon$  model differ by about 10%. But at higher angles of attack, the two  $k - \epsilon$  models diverge rapidly from both the Spalart-Allmaras and experimental values. As it can be concluded, the Spalart-Allmaras turbulence model gives the closest results to the experimental data over a wide range of angles of attack for both lift and drag coefficients.

### 3.7.3 Grid Sensitivity Analysis

The third step evaluates the solution dependency on the  $y^+$  value, and thus test the different wall treatment functions used by the turbulence models. Five structured O-mesh were used with the only difference among all was the distance of the first cell from the wall. Such a distance was set as  $5 \times 10^{-3}$ ,  $10^{-3}$ ,  $5 \times 10^{-4}$ ,  $10^{-4}$  and  $5 \times 10^{-5}$  chord. Also two turbulence models were used in the process, the Spalart-Allmaras model and the standard  $k - \epsilon$  model. As it has been mentioned in Sec. 3.5.1, if a coarse mesh is used and thus the laminar sublayer is not properly resolved, then the Spalart-Allmaras turbulence model will automatically use wall functions in order to compute the flow properties in the boundary layer. Concerning the  $k - \epsilon$  turbulence model, Fluent offers the option between three different wall function treatments. Namely, the standard wall treatment(SWT), the enhanced wall treatment(EWT) and the non-equilibrium wall treatment(neqWT). The recommendations given by Fluent [17] concerning grid construction for each of the wall function treatments are summarized in Table 3.2.

Turbulence Model	Wall Treatment	Recommended $y^+$
Spalart-Allmaras	Near wall wall functions	1 (up to 4-5) Between 30 and 60
$k - \epsilon$	SWT EWT neqWT	Between 30 and 60 1 (up to 4-5) more than 30

Table 3.2: Recommended  $y^+$  values for different wall treatment functions.

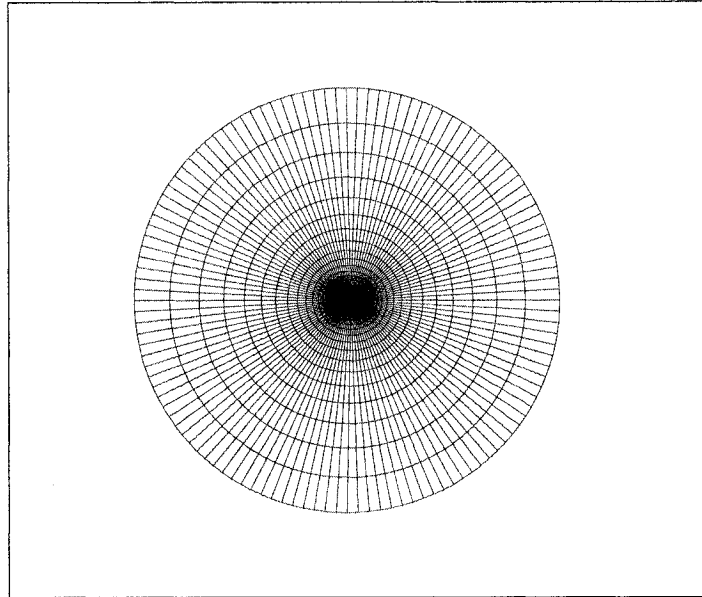
Simulations were performed on the five meshes with the free-stream conditions been set at values of Mach number equal to 0.15, Reynolds number equal to  $2 * 10^6$  and an angle of attack equal to  $4^\circ$ . Figures 3.8 and 3.9 plot the variation of lift and drag coefficients with respect to  $y^+$  for different wall treatment methods. Analyzing the lift variations with the mesh density, it seems that for the Spalart-Allmaras model and the  $k-\epsilon$  model with the EWT option, mesh independency is reached at the lower end of the  $y^+$  range with variations less than 0.5%. On the other hand, the  $k-\epsilon$  model with the neqWT option has reached mesh independency at the high end of the  $y^+$  range with variations less than 0.2% while the  $k-\epsilon$  model with the SWT option has reached a peak at the recommended values of  $y^+$ . By disregarding the lift coefficients with  $y^+$  values outside the recommended range given by Fluent (Table 3.2), the difference between the experimental lift coefficient and the numerical ones obtained is on the average of 4% over-prediction with those obtained by the Spalart-Allmaras model being the lowest at a value of about 3.5%.

Concerning the drag coefficient behavior and by tracing the variation of drag coefficient for the case of the Spalart-Allmaras turbulence model in Fig. 3.9, the closet value to the experimental data corresponds to the case with the smallest  $y^+$  value. In other words, it corresponds to the mesh with the closest cell to the wall where the laminar sublayer is fully resolved. This coincides with the recommendations given by Fluent for the Spalart-Allmaras turbulence model (Sec. 3.5.1). Also mesh independency is achieved for values of  $y^+$  less than 10 which is in total agreement with the behavior observed for the lift coefficient (Fig. 3.8). The same comments can be made about the case of the  $k-\epsilon$  turbulence model with the enhanced wall treatment option (EWT), where the same  $y^+$  restrictions are applied.

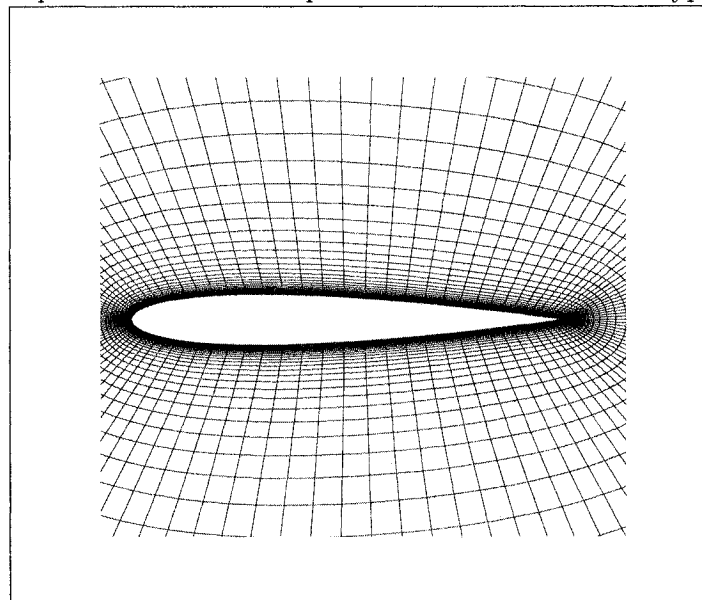
When using the  $k-\epsilon$  turbulence model with the standard and non-equilibrium wall treatment functions, the best drag coefficient values were obtained with higher values of  $y^+$  ( $20 \leq y^+ \leq 60$ ), which again is in agreement with the recommended

values given by Fluent manual and the conclusions drawn for the lift coefficient variations. This is also due to the fact that the law of the wall purpose is to bridge out the gap between the wall and the outer layer of the boundary layer by using special functions and thus a coarser mesh is required. Concerning the drag prediction, which is highly dependent on the viscous effects in the boundary layer and thus require the laminar sublayer to be fully resolved, it is clear from Fig. 3.9 that the closest match with the experimental data belongs to the one computed by the Spalart-Allmaras model. This is also in agreement with the conclusions drawn in the previous section (Sec. 3.7.2). Also this is achieved with the finest mesh where the  $y^+$  value is close to 1.

Going back to the points in the lift coefficient curve (Fig. 3.8) that are outside the recommended range of  $y^+$  and with values closer to the experimental lift coefficient, if the corresponding drag values are compared with the experimental one, it could be noticed that the difference is much higher where it cross in some cases the 30 and 60% difference. Thus considering the price been paid, which is about 4% increase in lift, at least 30% improvement in drag is achieved. From the discussion carried out in this section, it could be clearly stated that the Spalart-Allmaras turbulence model with a fine mesh, where  $y^+$  values are less than 5, is a more desirable choice for accurate drag prediction.

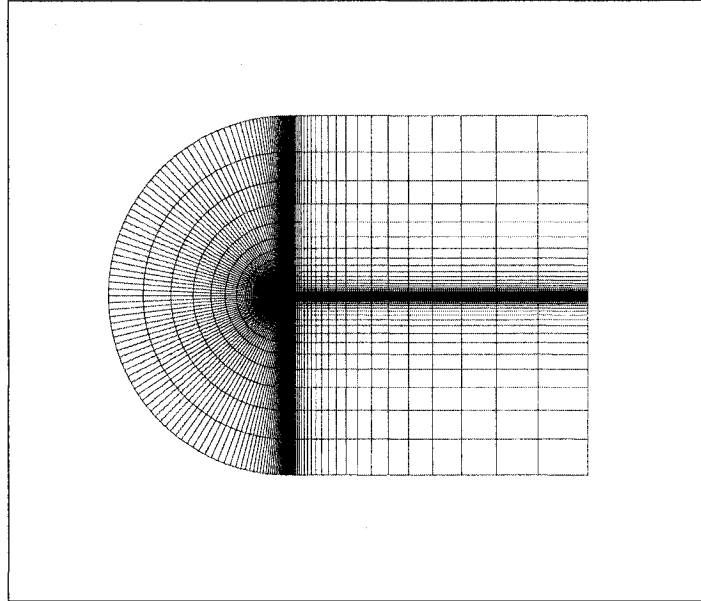


a. A complete view of the computational domain for an O-type mesh.

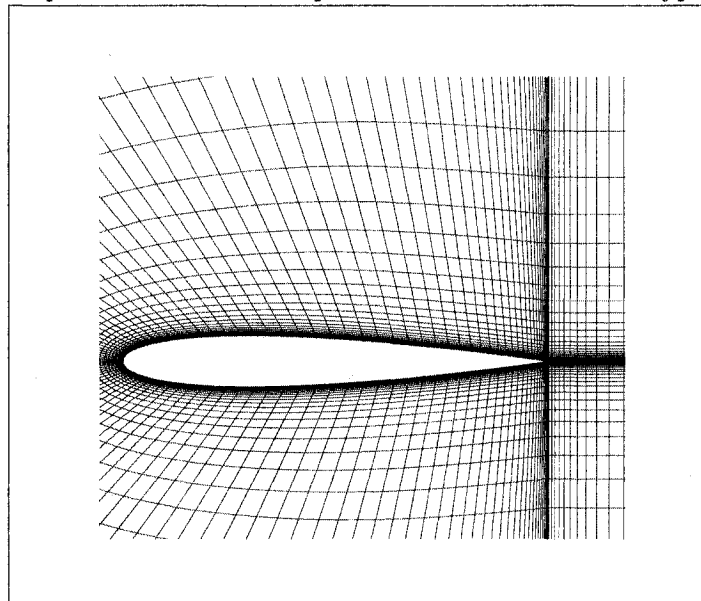


b. A close view of the airfoil for an O-type mesh.

Figure 3.1: A sample of a structured O-type mesh of a NACA-0012 airfoil.

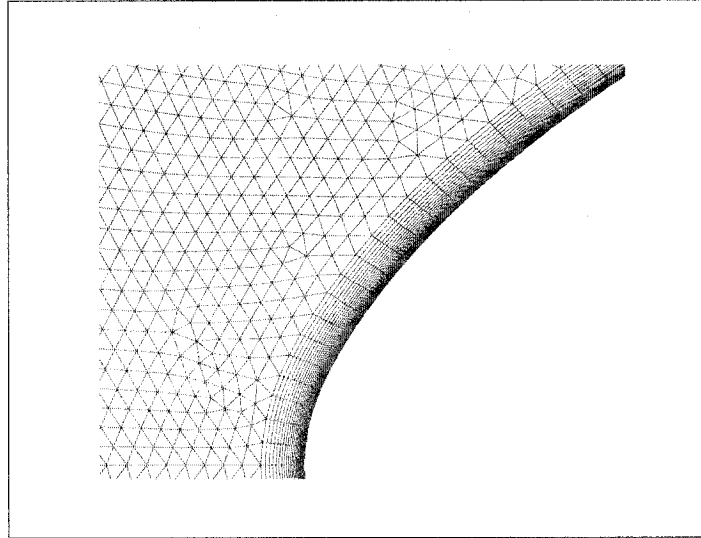


a. A complete view of the computational domain for a C-type mesh.

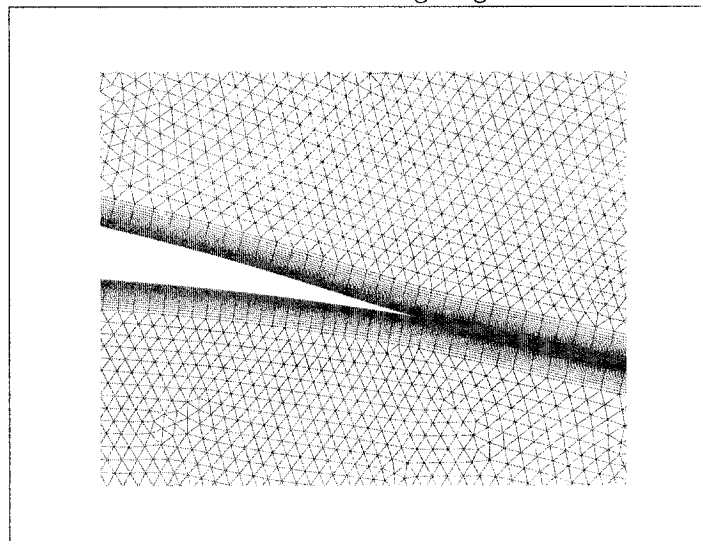


b. A close view of the airfoil for a C-type mesh.

Figure 3.2: A sample of a structured C-type mesh of a NACA-0012 airfoil.



a. A close view of the Leading Edge of the airfoil.



b. A close view of the Trailing Edge of the airfoil.

Figure 3.3: A sample of a hybrid mesh of a NLF-0416 airfoil.

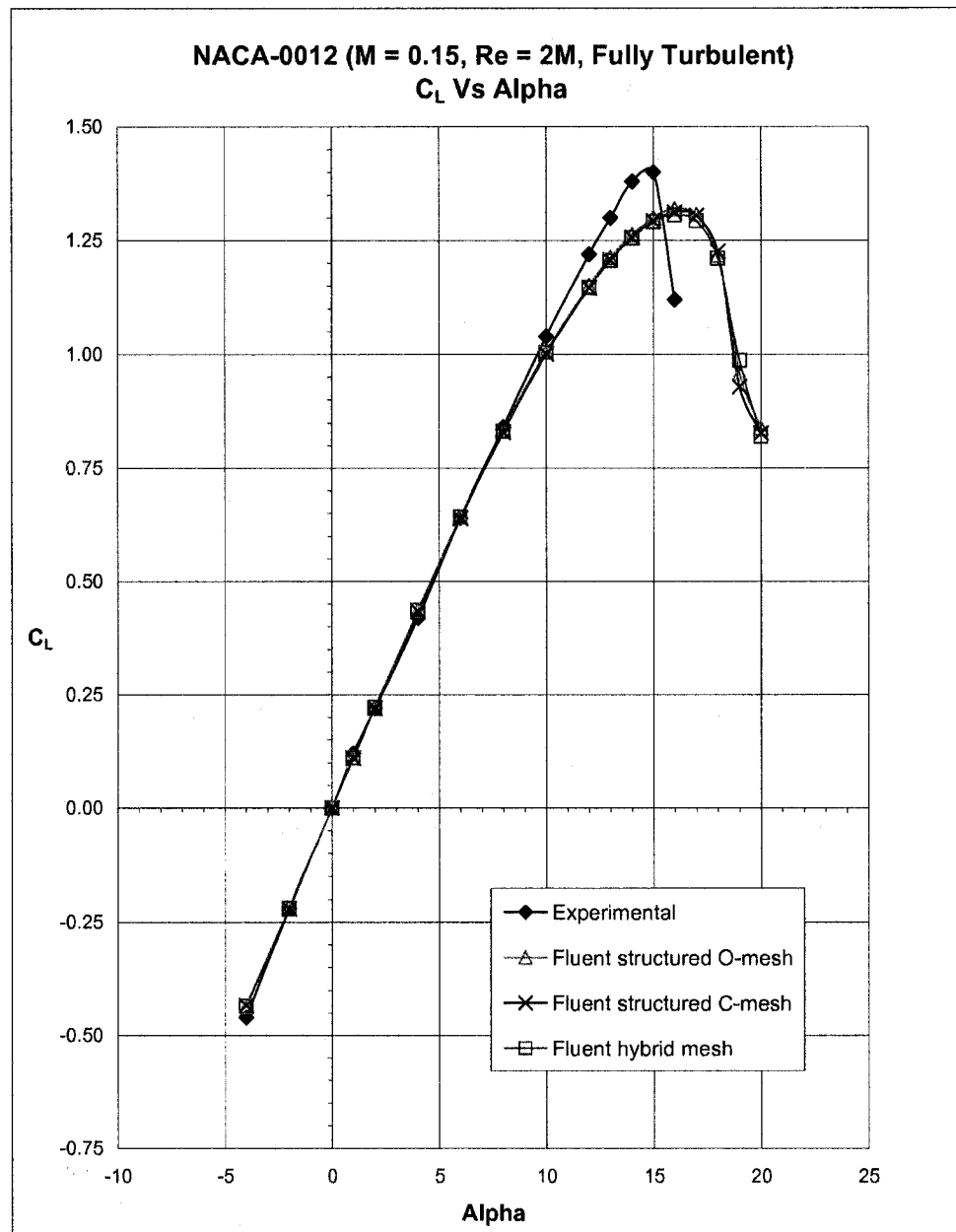


Figure 3.4: Lift coefficient comparison between experimental and numerical data for the Fully-Turbulent Spalart-Allmaras model on three different meshes for the NACA-0012 airfoil.

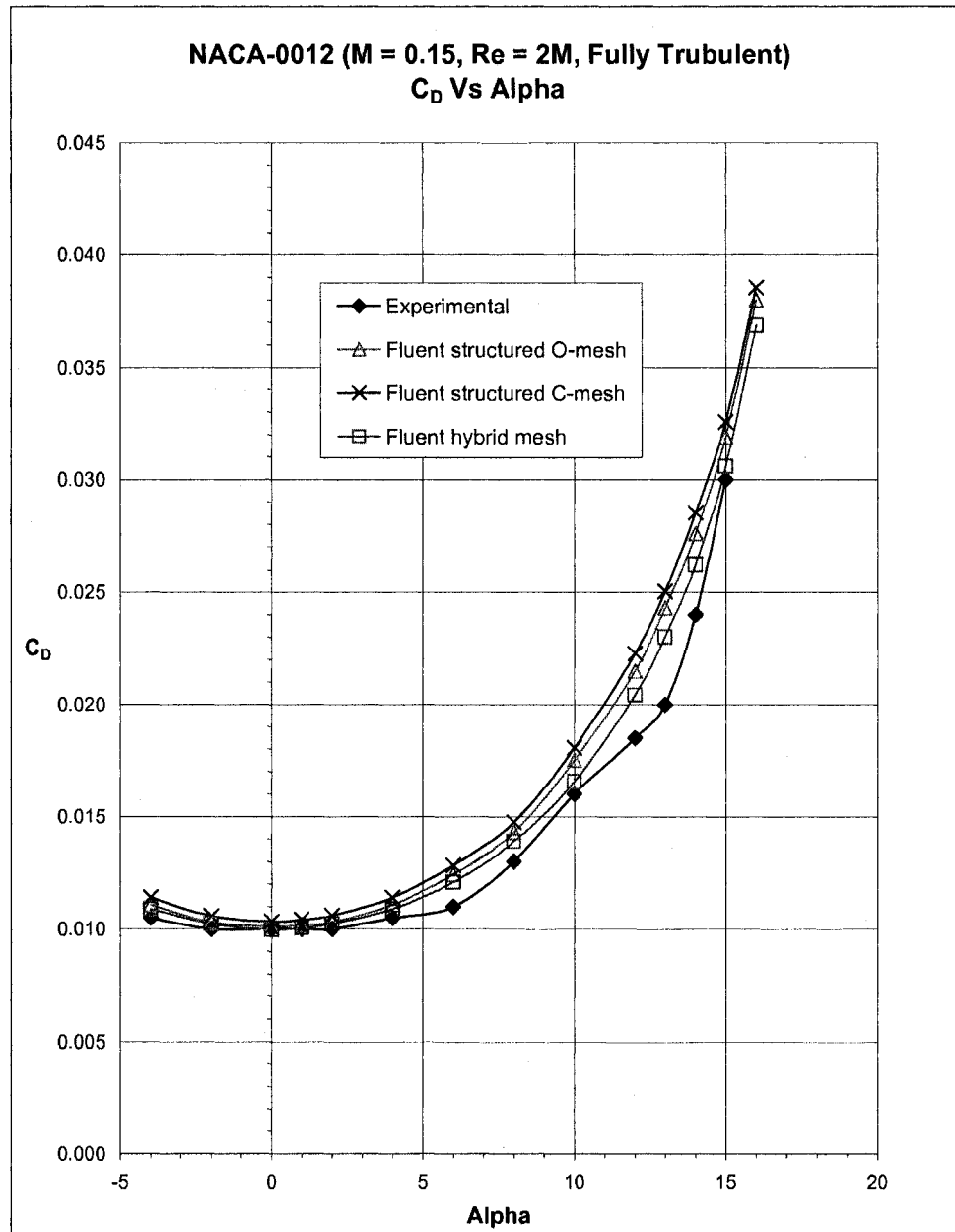


Figure 3.5: Drag coefficient comparison between experimental and numerical data for the Fully-Turbulent Spalart-Allmaras model on three different meshes for the NACA-0012 airfoil.



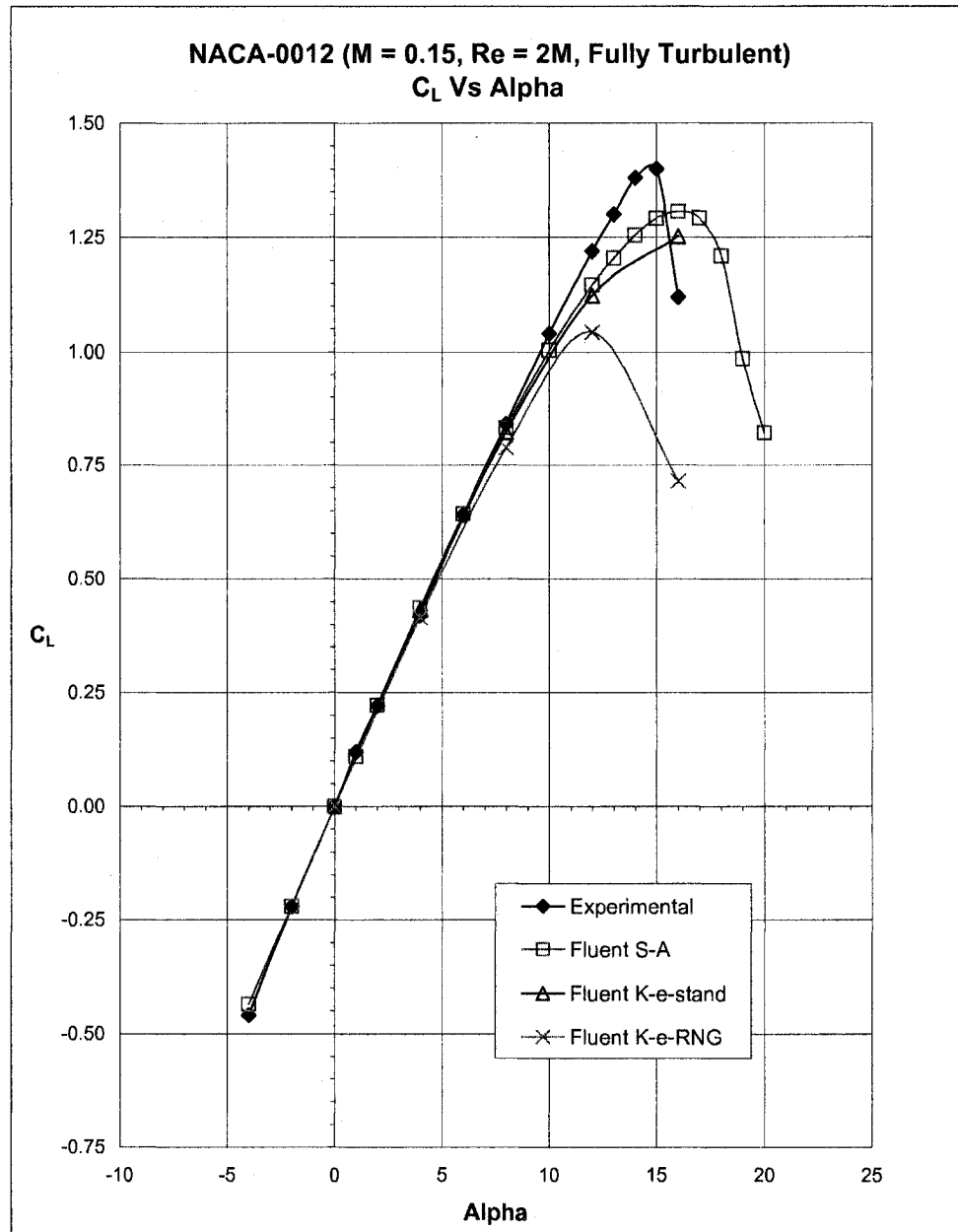


Figure 3.6: Lift coefficient comparison between experimental and numerical data for different turbulence models for the NACA-0012 airfoil.

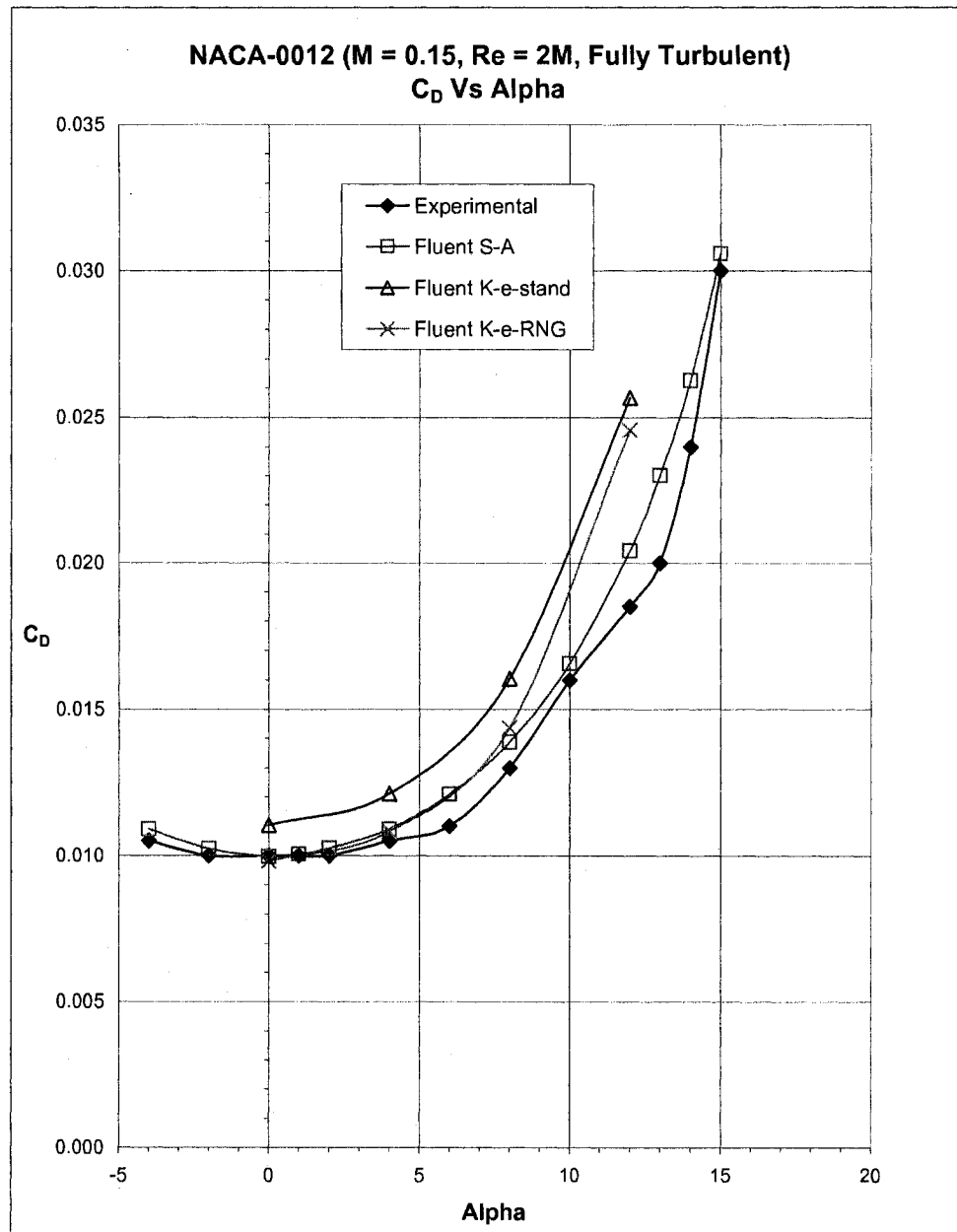


Figure 3.7: Drag coefficient comparison between experimental and numerical data for different turbulence models for the NACA-0012 airfoil.

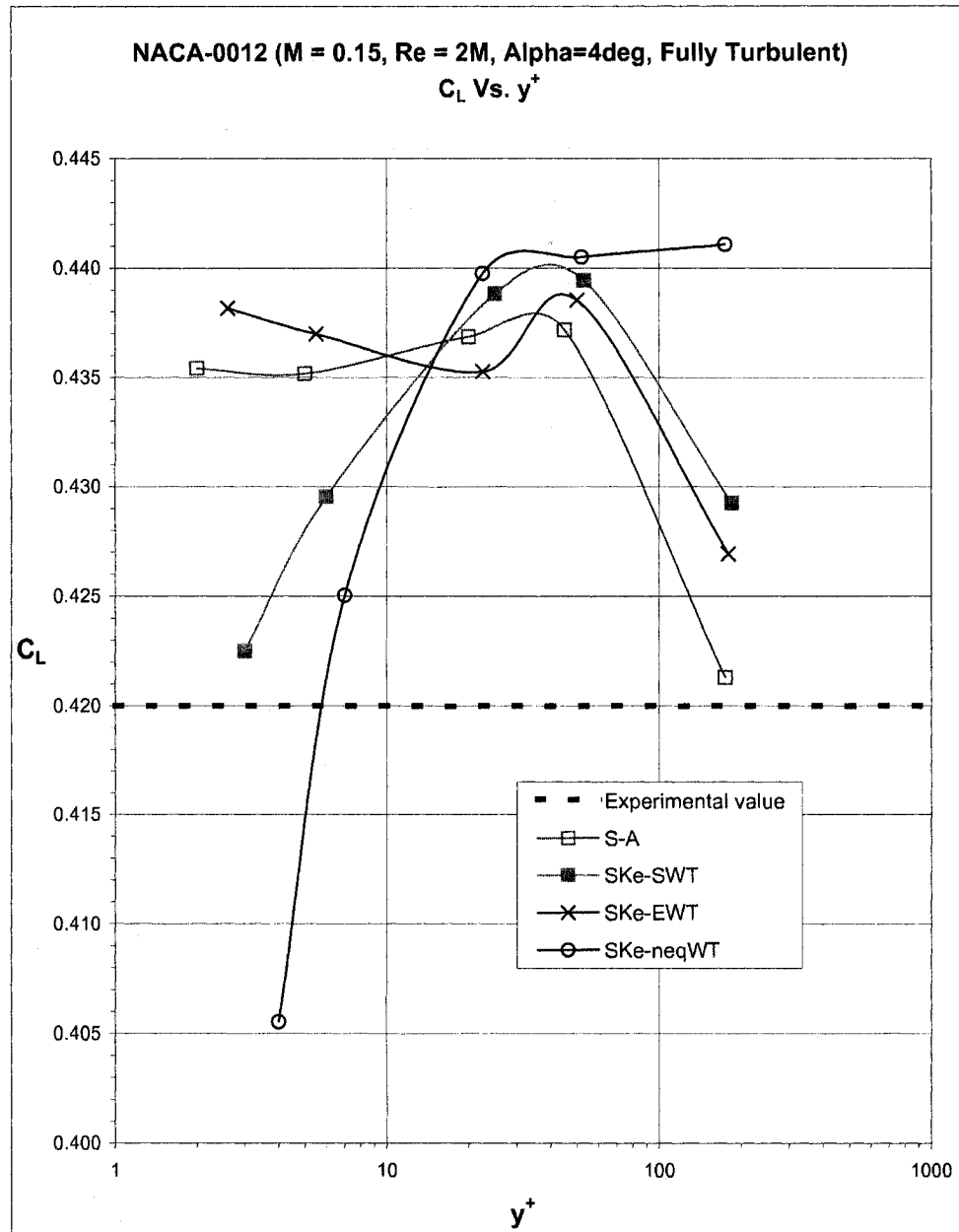


Figure 3.8: Lift coefficient variation with respect to  $y^+$  values for different wall treatment functions on an O-type structured mesh for the NACA-0012 airfoil.

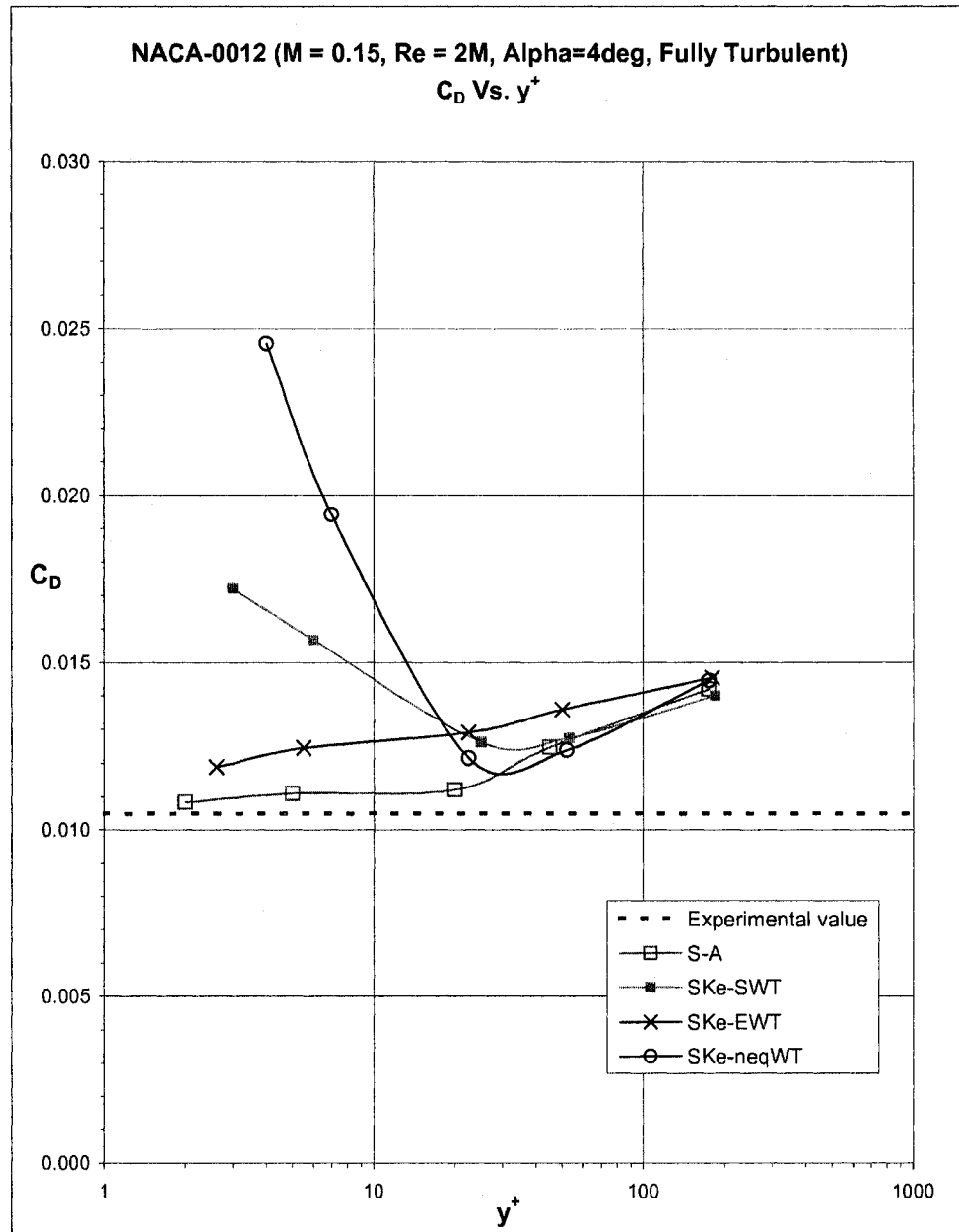


Figure 3.9: Drag coefficient variation with respect to  $y^+$  values for different wall treatment functions on an O-type structured mesh for the NACA-0012 airfoil.

## Chapter 4

# Transition Model Assessment for a One-Element Airfoil

To test the transition model effectiveness and accuracy, flow simulations using the new model were carried out for two well documented experimental cases: a single element airfoil (NLF-0416) that is presented in this chapter and a two-element airfoil (NLR-7301 with a trailing edge flap) that is presented in the next chapter. Even though a single case is presented where the flow is compressible, the rest of the cases are for incompressible flow conditions with Reynolds number greater than or equal to two millions. Thus the test cases considered are chosen as to match the flow assumptions under which the free transition model was developed. The results obtained with the new transition model were also compared with those obtained with the fully turbulent flow simulations.

### 4.1. NLF-0416 Airfoil (Incompressible Case)

The NLF-0416 is a Natural-Laminar-Flow airfoil designed for use in light, single-engine, general aviation airplanes. It was developed and tested by D. Somers at the NASA Langley Research center for the purpose of obtaining an airfoil with a low

cruise drag coefficient while maintaining a high maximum lift [20]. The term Natural-Laminar-Flow (NLF) airfoil refers to an airfoil which can achieve laminar flow over a significant extent of its chord ( $\geq 30\%$  chord) due to favorable pressure gradient only. Such a fact makes it a good candidate for validating the free transition model. The wind tunnel results published in [20] cover the following range of flow conditions: free-stream Mach number varies between 0.1 and 0.4, free-stream Reynolds number based on the airfoil chord varies between 1 and 9 millions, and the angle of attack varies between  $-16^\circ$  and  $17^\circ$ . Standard, low-speed, wind-tunnel boundary corrections have been applied to the experimental data. However, the wake-rake total pressure tube displacement corrections, a maximum increase of approximately 2 percent of the measured profile-drag coefficients, has not been taken into account [20]. To maintain the clarity of the data presented, error bars were not plotted in the figures shown in the current work.

Numerical simulations were carried out using Fluent as the flow solver and the Spalart-Allmaras turbulence model with and without the transition model, the original fully turbulent SA version used by Fluent (referred to as the Fully-Turbulent model) and the modified SA version where the free transition model is implemented (referred to as the Free-Transition model). The test cases performed on the current airfoil are divided into two groups, the incompressible test cases where free-stream Mach number  $M_\infty = 0.1$  and the compressible subsonic test cases where the free-stream Mach number  $M_\infty = 0.4$ . The current section will deal with the incompressible set while the compressible set will be discussed in Sec. 4.2. Thus for the incompressible flow conditions, tests were carried out for two different Reynolds numbers ( $Re_c$  equal to 2 millions and 4 millions) and it covers a wide range of angles of attack. Table 4.1 gives a summary of both experimental free-stream conditions available and the numerical free-stream conditions used in numerical simulations.

Based on the simulations carried out on the NACA-0012 airfoil concerning the

	Mach Number	Reynolds Number	Angles of Attack	Transition conditions
Experimental Data	0.1 - 0.4	1M to 9M	$-16^\circ$ to $17^\circ$	Free transition*
Numerical Data Case I	0.1	4M	$-16^\circ$ to $16^\circ$	a- Fully-Turbulent model b- Free-Transition model
Numerical Data Case II	0.1	2M	$0^\circ$ to $16^\circ$	a- Fully-Turbulent model b- Free-Transition model
Numerical Data Case III	0.4	6M	$-5^\circ$ to $14^\circ$	a- Fully-Turbulent model b- Free-Transition model

Table 4.1: Experimental and numerical free-stream flow conditions for the NLF-0416 cases. (\* Experimental data are only available for the following conditions:  $M = 0.1$  and  $Re = 1M$  to  $4M$ .)

mesh sensitivity (Sec. 3.7.1), where the hybrid mesh proved to give more reliable results for the drag prediction, a hybrid mesh is used as the computational domain for the current test cases. Thus a structured C-mesh is built around the airfoil so as to control  $y^+$  and the mesh stretching near the airfoil surface. The remaining part of the computational domain is filled with unstructured triangular mesh. The distance of the first cell adjacent to the airfoil surface was taken to be  $10^{-5}$  chord with the boundary layer structured mesh stretching for 35 cells in the direction normal to the airfoil surface. This ensured an average  $y^+$  value that is about 1, in accordance with the recommendations given in Fluent documentations [17]. Again when constructing the structured boundary layer mesh around the airfoil, the structured domain was extended for about 25% of the chord length at the trailing edge with a slope parallel to the trailing edge slope. The whole mesh is composed of 157,250 cells that corresponds to 92,173 nodes.

#### 4.1.1 Case I: $M_\infty = 0.1$ , $Re = 4 * 10^6$

The free-stream conditions for the first group of test cases are : Mach number  $M_\infty = 0.1$ , Reynolds number  $Re_c = 4$  millions and a range of angles of attack varying

between  $-16^\circ$  and  $16^\circ$ . The data obtained from the converged solutions were compiled together in order to produce the characteristic curves presented in this section. Figure 4.1 compares the transition onset  $x_t$  predicted by the developed transition model, on both the upper and lower sides of the airfoil, with that obtained from the experimental data for different angles of attack. The transition onset is captured experimentally by using microphone measurements. Such a method is based on the concept that laminar flow is silent while a turbulent flow is noisy. Since the microphone is connected to individual orifices on the model surface, the onset location can only be determined as in between two adjacent orifices [20]. Thus the open symbols in Fig. 4.1 represent orifice locations at which the flow is laminar and the solid symbols represent orifice locations at which the flow is turbulent. Analyzing Fig. 4.1, it is to be noticed that the transition onset on both sides of the airfoil are changing in the same direction as that of the stagnation point. That is, with increasing the angle of attack, the location of the transition onset on the upper surface is moving forward and the location of transition onset on the lower surface is moving backward. Such a behavior is in accordance with the one observed experimentally and expected physically. Quantitatively, the predicted transition onset is in the vicinity of the limits given by the experimental data for a large range of angles of attack.

Figures 4.2 and 4.3 compare the variation of the drag and lift coefficients with the angle of attack ( $\alpha$ ) for three sets of data, one set is given experimentally [20] and the other two sets are obtained numerically by using the Fully-Turbulent and Free-Transition models. Examining the drag coefficient for the three sets (Fig. 4.2), the improvement achieved in numerical drag computations by switching from a Fully-turbulent Spalart-Allmaras turbulence model to the developed Free-Transition one is quite clear. As an example, for zero angle of attack the experimental drag coefficient is 59 drag counts (0.0059) while the value predicted using the Fully-Turbulent model is 99.07 drag counts (0.009907) with a variation from the experimental value equal



to 40 drag counts. On the other hand, the values predicted using the Free-Transition model is equal to 59.34 drag counts (0.005934) with a difference that is less than one drag count. Such results are repeated for other angles of attack, where the difference between experimental and numerical data obtained using the Free-Transition model is again less than one drag count for  $\alpha = 1^\circ$  and  $-6^\circ$ . It is also less than 5 drag counts for  $-8^\circ \leq \alpha \leq 2^\circ$ . It is equal to 3.86 drag counts at  $\alpha = 14^\circ$ . The maximum difference is obtained for angles of attack between  $4^\circ$  and  $12^\circ$  where it is at an average of 22 drag counts. On the other hand, the difference between the drag values computed using the Fully-Turbulent model and those given experimentally is much higher where it is between 40 and 50 drag counts for  $0^\circ \leq \alpha \leq 14^\circ$  and on an average of 15 drag counts for most of the negative angles of attack. Table 4.2 gives a comparison of the predicted drag values at selected angles of attack.

As for the lift coefficient, the Free-Transition model over-predicts lift values for angles of attack between  $-8^\circ$  and  $6^\circ$  with an average equal to 0.04 while the difference between the experimental values and those computed using the Fully-Turbulent model is less than 0.01 for the same range of angles of attack. Such a difference would increase rapidly for angles of attack outside the given range. Nonetheless, for  $\alpha > 6^\circ$  both models under-predict lift. But the values computed by the Free-Transition model are closer to the experimental ones where  $C_{L,max}$  is under-estimated by about 0.08 using the Free-Transition model. Also the predicted location of  $C_{L,max}$  using numerical simulations is delayed by about one degree. Such a behavior is similar to the one observed in the case of the NACA-0012 airfoil presented in Sec. 3.7.

### **Pressure and Skin-Friction Coefficients:**

In order to acquire a better understanding of the flow properties and behavior under the specified free-stream conditions, plots of the pressure and skin-friction coefficients at two different angles of attack are presented in this section. Also figures that

Alpha	Experimental Data	Numerical Data Fully-Turbulent S-A	Numerical Data Free-Transition S-A
	$C_D$ (2% error)	Difference in $C_D$	Difference in $C_D$
$-14^\circ$	0.0367	-86 drag count (-23.4%)	-9 drag count (-2.4%)
$-6^\circ$	0.0093	16 drag count (+17%)	0.825 drag count (+0.9%)
$0^\circ$	0.0059	40 drag count (+68%)	0.34 drag count (+0.6%)
$8^\circ$	0.0107	46 drag count (+42.4%)	25 drag count (+22.8%)
$14^\circ$	0.0249	47 drag count (+18.6%)	3.86 drag count (+1.6%)
	$C_L$	Difference in $C_L$	Difference in $C_L$
$-14^\circ$	-1.134	0.1688 (+15%)	0.1440 (+12.7%)
$-6^\circ$	-0.269	0.0118 (+4.4%)	0.0320 (+11.9%)
$0^\circ$	0.447	0.0053 (+1.2%)	0.0381 (+8.5%)
$8^\circ$	1.317	-0.0233 (-1.8%)	0.0035 (+0.3%)
$14^\circ$	1.765	-0.1396 (-7.9%)	-0.0794 (-4.5%)

Table 4.2: Difference in the lift and drag coefficients between experimental and numerical results for the Fully-Turbulent and Free-Transition models for the NLF-0416 airfoil Case I ( $M_\infty = 0.1$ ,  $Re = 4 * 10^6$ ) [1 drag count =  $10^{-4}$ ].

symbolize contours of the Mach number are added for the two cases considered. Figures 4.4, 4.6 and 4.8 represent the pressure coefficient, skin-friction coefficient and the Mach number contours for the case of  $\alpha = 0^\circ$ . And the pressure coefficient, skin-friction coefficient and the Mach number contours for the case of  $\alpha = 8^\circ$  are given in Figs. 4.5, 4.7 and 4.9 respectively. The pressure coefficient distribution over the airfoils surface shown in Figs. 4.4 and 4.5 belong to three sets of data, experimental, Fully-Turbulent and Free-Transition numerical models. As can be seen from these figures, there is a fair agreement between all three sets of data. As for the skin-friction coefficient distribution over the airfoils surface, due to the absence of any experimental data, only numerical data obtained for the two models (Fully-Turbulent and Free-Transition) are plotted in these figures. By comparing the two corresponding sets of data, the effect of introducing the Free-transition model into the computation is evident. The skin-friction coefficient distribution in the leading part of the airfoil have changed in order to take into account the introduction of the

Laminar-Transition zones by the Free-Transition model. As it can also be observed by comparing Figs. 4.6 and 4.7, the difference in skin-friction distribution between the two models is bigger for the one corresponding to  $0^\circ$  angle of attack than the other case. This can explain the larger difference in predicted drag between the Fully-Turbulent and Free-Transition models for the first case where it is about 70% while it is about 20% for the second case. Looking at the Mach number contours presented in Figs. 4.8 and 4.9, the maximum Mach number achieved is within the limit of 0.138 and 0.189 for the angles of attack  $0^\circ$  and  $8^\circ$ , respectively. This confirms that the flow is within the incompressible limits.

The main conclusion that can be drawn out from the  $C_p$  and  $C_f$  distributions is that the pressure field is almost unaffected by introducing the Free-Transition model. On the other hand, the skin friction distribution for the Fully-Turbulent and the Free-Transition models reflects a strong dependency on transition. This emphasizes the fact that, while lift is controlled by the inviscid flow for attached flows, drag is controlled by the viscous boundary layer flow.

### 4.1.2 Mesh Sensitivity Analysis

Another two series of simulations were carried out in order to examine the mesh sensitivity of the developed Free-Transition model. To perform such a task, a coarse and a medium size meshes were constructed where the distance of the first cell from the airfoil surface is  $10^{-4}$  and  $5 * 10^{-5}$  chord, respectively. Free stream conditions are the same as those simulated in Case I (i.e.  $M_\infty = 0.1$ ,  $Re_c = 4$  millions and  $0^\circ \leq \alpha \leq 16^\circ$ ). Thus a comparison can be made with the mesh used previously where the distance of the first cell from the wall was set as  $10^{-5}$  chord (referred to as the fine mesh). An important parameter to be looked at is the  $y^+$  value obtained using the three different meshes. For the fine mesh, the average  $y^+$  is equal to 1 compared to a value of 12 for the coarse mesh. Table 4.3 summarizes the average  $y^+$

values obtained for each of the three meshes.

Mesh type	Coarse	Medium	Fine
Distance from the wall	$10^{-4}$	$5 * 10^{-5}$	$10^{-5}$
Average $y^+$ values	12	5	1

Table 4.3:  $y^+$  variations with respect to the mesh first cell distance from the wall for the NLF-0416 airfoil Case I ( $M_\infty = 0.1, Re = 4 * 10^6$ ).

Figures 4.10 and 4.11 compare the lift and drag coefficient variation with the angle of attack obtained numerically for the three meshes and the experimental data given. By examining these figures, a set of observations can be drawn. The lift coefficients computed numerically using the three different meshes match each other with a difference less than 1% at low angles of attack. At angles of attack higher than  $6^\circ$ , the difference between the coarse mesh and the other two meshes starts to increase while it stays within the 1% limit between the fine and medium meshes. It also can be added that the behavior observed previously concerning the delay in predicting the stall angle and the under-prediction of the lift at high angles of attack is present in this case also with the lift coefficients near  $C_{L,max}$  obtained using the coarse mesh are closer to the experimental values.

As for drag prediction, it is to be noticed that at low angles of attack the fine and medium meshes are in total agreement where the difference between both sets is less than one drag count. However, this is not the case for the coarse mesh where the difference between the data obtained for this set and the other two sets starts at about 3 drag counts for  $\alpha = 0^\circ$  and increases for angles of attack equal to  $4^\circ$  and more. Such a difference would reach a maximum of 30 drag counts at  $\alpha = 14^\circ$ . This is also the case between the fine and medium meshes for  $\alpha \geq 8^\circ$  with a maximum difference of about 15 drag counts at angles of attack equal to  $12^\circ$  and  $14^\circ$ .

From the analysis carried out in the current section, it can be concluded that viscous flow properties are clearly dependent on the  $y^+$  values as well as the mesh

quality. This is also in agreement with the recommendations given by Fluent which suggest that when using the Spalart-Allmaras turbulence model the  $y^+$  values should fall between 1 and 5 (Sec. 3.5.1). The computed lift and drag values are quite sensitive to  $y^+$ . Thus the data computed using the fine mesh, with an average  $y^+$  of 1, and the medium mesh, with an average  $y^+$  of 5, are in better harmony than the third mesh which failed to achieve the suggested  $y^+$  values.

Difference in $C_L$ (in %)	Coarse ( $y^+ \approx 12$ )	Medium ( $y^+ \approx 5$ )	Fine ( $y^+ \approx 1$ )
Alpha = 0°	+9.2	+8.3	+8.5
Alpha = 4°	+5.8	+4.7	+4.7
Alpha = 8°	+2.3	+0.4	+0.3
Alpha = 12°	-1.6	-3.4	-4.6
Alpha = 14°	-1.7	-3.9	-4.5
Difference in $C_D$ (in %)			
Alpha = 0°	-7.8	+3.1	+0.6
Alpha = 4°	+7.3	+23.2	+24.2
Alpha = 8°	-0.9	+17.8	+22.8
Alpha = 12°	-7.2	+5.1	+13.6
Alpha = 14°	-14.4	-5.1	+1.6
Difference in $C_D$ (in Drag Count)			
Alpha = 0°	-4.57	+1.82	+0.34
Alpha = 4°	+4.9	+15.5	+16.24
Alpha = 8°	-1	+19	+24.4
Alpha = 12°	-12.8	+9.12	+24.28
Alpha = 14°	-35.9	-12.75	+3.86

Table 4.4: Difference in the lift and drag coefficients between experimental and numerical results obtained for three different meshes used in evaluating the mesh sensitivity of the Free-Transition model for the NLF-0416 airfoil Case I ( $M_\infty = 0.1$ ,  $Re = 4 * 10^6$ ) [1 drag count =  $10^{-4}$ ].

### 4.1.3 Case II: $M_\infty = 0.1, Re = 2 * 10^6$

The second group of simulations was carried out at the following free-stream conditions: Mach number  $M_\infty = 0.1$ , Reynolds number  $Re_c = 2$  millions and a range of angles of attack that varies between  $0^\circ$  and  $16^\circ$ . The fine hybrid mesh ( $y_{ave}^+ \approx 1$ ) is used in the current simulations. Once again, the data obtained from the converged solutions were used to compile together the same set of variables presented in case I. Simulations were carried out using the Spalart-Allmaras turbulence model with and without the free transition model.

Thus Fig. 4.12 compares the transition onset  $x_t$  predicted by the Free-Transition model, for both the upper and lower airfoil surfaces, with that obtained from the experimental data for different angles of attack. Similar behavior to the one observed in Case I, Sec. 4.1.1, is repeated in the current case. Here again the transition onset variation with the angle of attack is in complete harmony with those observed experimentally and the values computed are in the vicinity of the limits given by the experimental data for a large range of angles of attack. Nonetheless, the predicted values on the airfoil lower side match better the experimental results compared with the ones predicted on the upper side.

As for the drag and lift coefficients, the general trend is similar to the one observed in the first group of simulations. Figs. 4.13 and 4.14 compare the variation of drag and lift coefficients, respectively, with angle of attack ( $\alpha$ ) for three sets of data (experimental, the Fully-Turbulent and Free-Transition numerical models). Examining the drag coefficient for the three sets (Fig. 4.13), the improvement achieved in numerical drag computations by switching from a Fully-Turbulent Spalart-Allmaras turbulence model to the developed Free-Transition one is quite clear. For zero angle of attack, the experimental drag coefficient is 69 drag counts while the value predicted using the Fully-Turbulent model is 110 drag counts with a variation from the experimental value equal to 41 drag counts. On the other hand, the values predicted

using the Free-Transition model is equal to 64 drag counts with a variation from the experimental value equal to 5 drag counts. Thus the difference has dropped by about 8 times. For angles of attack between  $4^\circ$  and  $10^\circ$ , the difference in drag coefficients given experimentally and those obtained using the Fully-Turbulent model is on the average 50 drag counts. While the difference between the experimental values and those obtained using the Free-Transition model is on the average of 26 drag counts. And at angle of attack of  $12^\circ$ , where the experimental drag coefficient is equal to 214 drag counts, the difference in the value predicted by the Fully-Turbulent model and the one given experimentally is equal to 37.5 drag counts while it is equal to 8.5 drag counts for the Free-Transition model case. A summary of some of the results obtained for drag and lift coefficients is given in Table 4.5.

Alpha	Experimental Data	Numerical Data Fully-Turbulent S-A	Numerical Data Free-Transition S-A
	$C_D$ (2% error)	Difference in $C_D$	Difference in $C_D$
$0^\circ$	0.0069	41 drag count (+59.5%)	-5 drag count (-7.2%)
$6^\circ$	0.0094	51 drag count (+54.1%)	26 drag count (+27.7%)
$12^\circ$	0.0214	38 drag count (+17.5%)	8.5 drag count (+4%)
	$C_L$	Difference in $C_L$	Difference in $C_L$
$0^\circ$	0.430	0.010 (+2.3%)	0.049 (+11.4%)
$6^\circ$	1.103	-0.013 (-1.9%)	0.012 (+1.1%)
$12^\circ$	1.605	-0.079 (-4.9%)	-0.061 (-3.8%)

Table 4.5: Difference in the lift and drag coefficients between experimental and numerical results for the Fully-Turbulent and Free-Transition models for the NLF-0416 airfoil Case II ( $M_\infty = 0.1$ ,  $Re = 2 * 10^6$ ) [1 drag count =  $10^{-4}$ ].

As for the lift coefficient, the curves can be divided into two sections: one corresponding to low values of angles of attack where  $\alpha \leq 6^\circ$  and another one that corresponds to high values of angles of attack where  $\alpha > 6^\circ$ . For the first section, the Free-Transition model again over-predicts the lift with a maximum difference of 0.045 at zero angle of attack and an average difference equal to 0.032 while the difference between the experimental values and those predicted using the Fully-Turbulent model

are less than 0.01. However, for higher angles of attack both models under-predict the lift values with those obtained by the Free-Transition model being closer to the experimental ones with a difference equal to 0.06 at an angle of attack equal to  $12^\circ$ . Finally,  $C_{L,max}$  predicted numerically is delayed by about 2 degrees for both models. Nonetheless, these results are consistent with the ones obtained for the first group of simulations where Reynolds number was equal to 4 millions.

## 4.2. NLF-0416 Airfoil (Compressible Case)

### 4.2.1 Case III: $M_\infty = 0.4$ , $Re = 6 * 10^6$

In order to assess the performance of the developed transition model under compressible flow conditions, simulations were carried out on the NLF-0416 airfoil with Mach number  $M_\infty = 0.4$  and  $Re_c = 6$  millions. The angle of attack was varied between  $-5^\circ$  and  $14^\circ$ . Numerical simulations, as before, were performed using the Spalart-Allmaras turbulence model with one of the two configurations, the Fully-Turbulent model and the Free-Transition model. As for the computational domain, the same fine hybrid mesh ( $y_{ave}^+ \approx 1$ ) was used to perform the computations.

Figures 4.15 and 4.16 represent the Mach number contours at two different angles of attack:  $0^\circ$  and  $12^\circ$ , respectively. The local Mach number in the boundary layer reaches a maximum of 0.58 and 1.28 on the airfoils upper side for  $\alpha = 0^\circ$  and  $12^\circ$ , respectively. Thus the flow in the boundary layer is compressible and add to that there is a shock near the leading edge for the last case ( $\alpha = 12^\circ$ ). Actually, the shock starts to appear in the flow for  $\alpha \geq 11^\circ$ . This is reflected in the results obtained using the Free-Transition model.

Figure 4.17 provides the transition onset  $x_t$  predicted by the developed transition model for different angles of attack. Due to the absence of any experimental readings of the transition onset for the current case, only the numerical data are



presented. For  $\alpha \leq 11^\circ$ , the variation of the transition onset location on both sides of the airfoil is similar to the one obtained for the incompressible cases presented in the previous sections (Figs. 4.1 and 4.12). However, for  $\alpha \geq 11^\circ$ , there is a twist in the direction of the predicted transition onset on the upper side of the airfoil. This coincides with the location of the shock which appears on the airfoils upper side near the leading edge for the same range of angles of attack. After reviewing these cases, it was concluded that, by the current method used for transition onset prediction, the location of the transition onset is delayed till after the shock. This is inconsistent with the physics of the problem and it is one of the current model's limitations.

Figures 4.18 and 4.19 compare the variation of drag and lift coefficients with angle of attack ( $\alpha$ ) for three sets of data (experimental, Fully-Turbulent and Free-Transition models). Figure 4.18 shows, as in the cases presented previously, an improvement in predicted drag values when the free transition model is implemented in the turbulence model. For zero angle of attack, the experimental drag coefficient is about 57 drag counts. The drag value computed by the Fully-Turbulent model is equal to 97.6 drag counts with a difference equal to about 40 drag counts. On the other hand, the drag coefficient predicted by the Free-Transition model is equal to 61.56 drag counts where the difference with the experimental value drops to about 4 drag counts. Thus for  $-5^\circ \leq \alpha \leq 1^\circ$ , the difference in drag coefficient between the values given experimentally and the ones predicted using the Free-Transition model is within the 5 drag counts limit. As the angle of attack is increased beyond the  $1^\circ$  limit, the difference in drag increases where it reaches a maximum of 65 drag counts in difference at  $\alpha = 11^\circ$ . Such a difference is larger than the one observed in the incompressible cases presented in the previous sections. This is also true for the Fully-Turbulent model case where the difference between numerical and experimental drag values also increases with increasing the angle of attack.

As for the lift coefficient, the trend followed by the numerical values is similar to

the one observed in previous cases presented. Once again the Free-Transition model over-predicts lift for  $\alpha < 5^\circ$  with an average difference equal to 0.03. And for  $\alpha \geq 5^\circ$ , the model under-predicts lift by a difference that is about 0.07 at  $C_{L,max}$ , plus the location of  $C_{L,max}$  is delayed by about  $1^\circ$ . Table 4.6 summarizes some of the results obtained for the current case.

The main conclusion that can be drawn from the current section is that as the local Mach number increases beyond 0.85 (which occurs when the angle of attack exceeds  $8^\circ$ ), the discrepancy in drag coefficient between the Free-Transition model and experimental data becomes too large and reaches a peak when the flow is transonic when  $\alpha \geq 11^\circ$ . Such a behavior is expected since the Free-Transition model assumes incompressible flow.

Alpha	Experimental Data	Numerical Data Fully-Turbulent S-A	Numerical Data Free-Transition S-A
	$C_D$ (2% error)	Difference in $C_D$	Difference in $C_D$
$-5^\circ$	0.0081	18.3 drag count (+22.5%)	-2.80 drag count (-3.5%)
$0^\circ$	0.0057	40.1 drag count (+69.9%)	4.10 drag count (+7.2%)
$5^\circ$	0.0077	56.5 drag count (+72.6%)	27.0 drag count (+34.7%)
$11^\circ$	0.0165	79.9 drag count (+48.4%)	65.1 drag count (+39.4%)
	$C_L$	Difference in $C_L$	Difference in $C_L$
$-5^\circ$	-0.177	0.0282 (+16%)	0.0502 (+28.4%)
$0^\circ$	0.4933	-0.0057 (-1.2%)	0.0315 (+6.4%)
$5^\circ$	1.1316	-0.0431 (-3.8%)	-0.0056 (-0.5%)
$11^\circ$	1.8395	-0.1951 (-10.6%)	-0.1857 (-10.1%)

Table 4.6: Difference in the lift and drag coefficients between experimental and numerical results for the Fully-Turbulent and Free-Transition models for the NLF-0416 airfoil Case III ( $M_\infty = 0.4$ ,  $Re = 6 * 10^6$ ) [1 drag count =  $10^{-4}$ ].

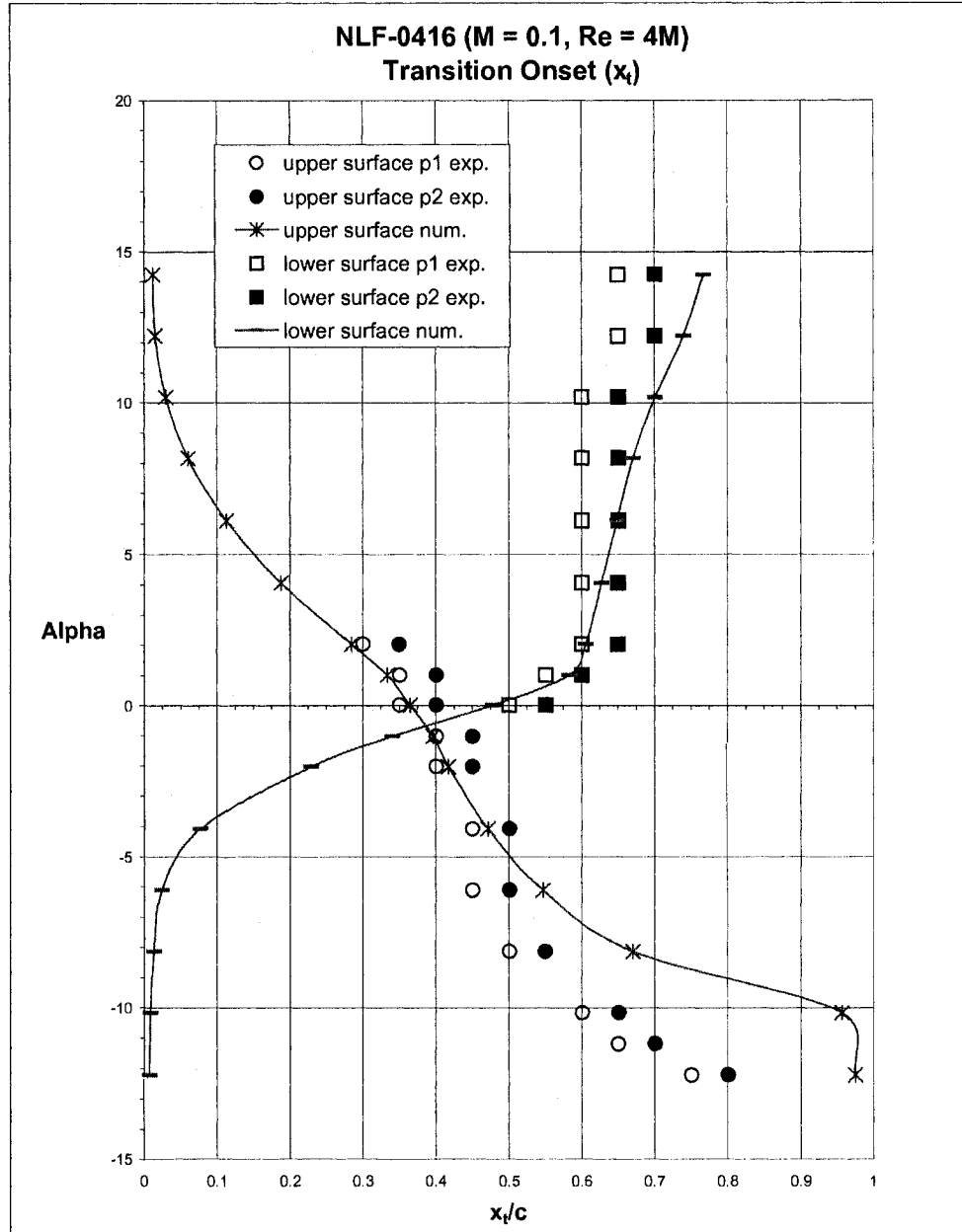


Figure 4.1: Model validation of the transition onset for the NLF-0416 airfoil Case I ( $M_\infty = 0.1$ ,  $Re = 4 * 10^6$ ). (The empty dots and squares represent laminar region and the filled dots and squares represent turbulent regions. Solid lines correspond to numerical calculations.)

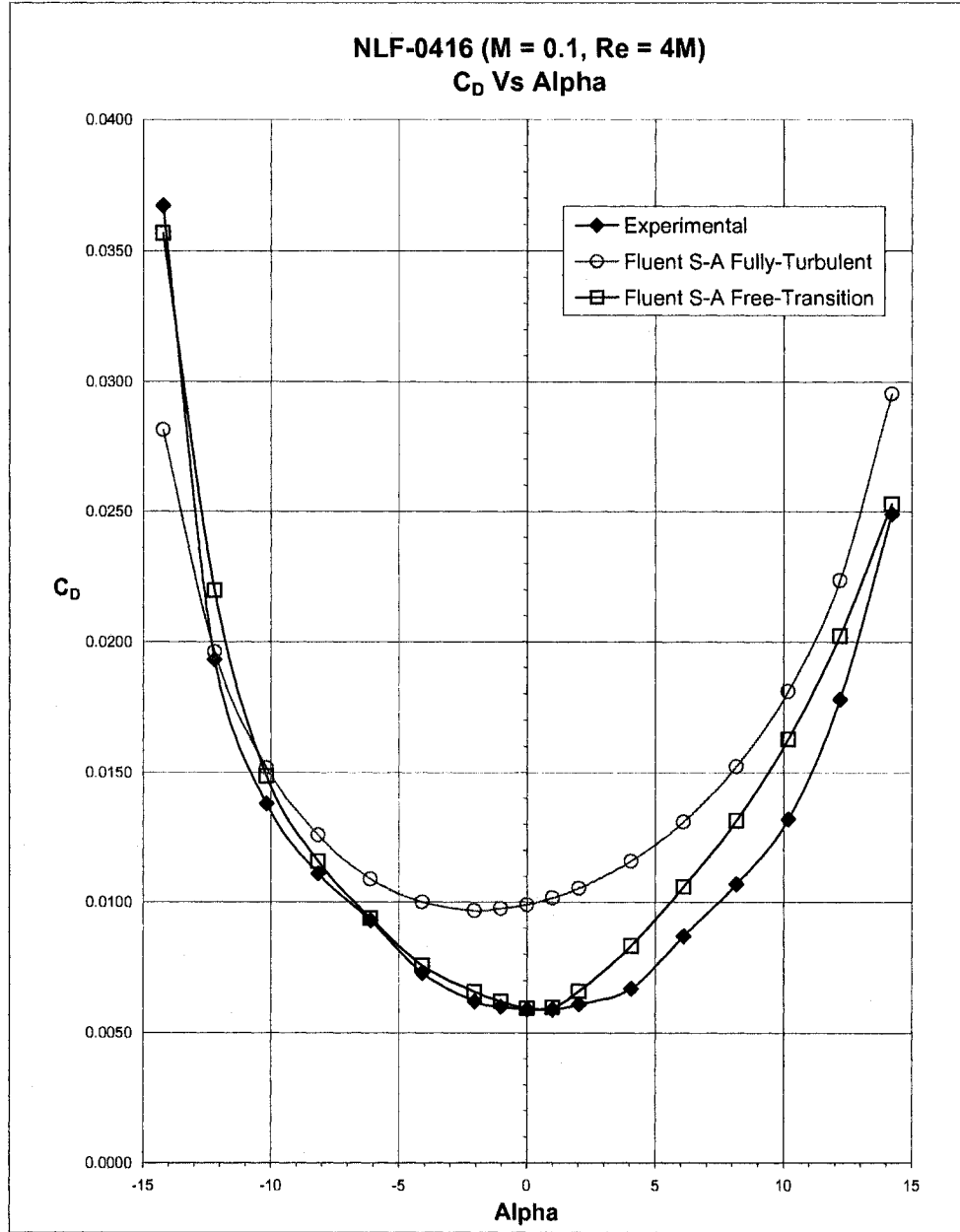


Figure 4.2: Drag coefficient comparison between experimental results and numerical results for the Fully-Turbulent and Free-Transition models for the NLF-0416 airfoil Case I ( $M_\infty = 0.1$ ,  $Re = 4 * 10^6$ ) [error in experimental drag coefficient is equal to a maximum increase of 2%].

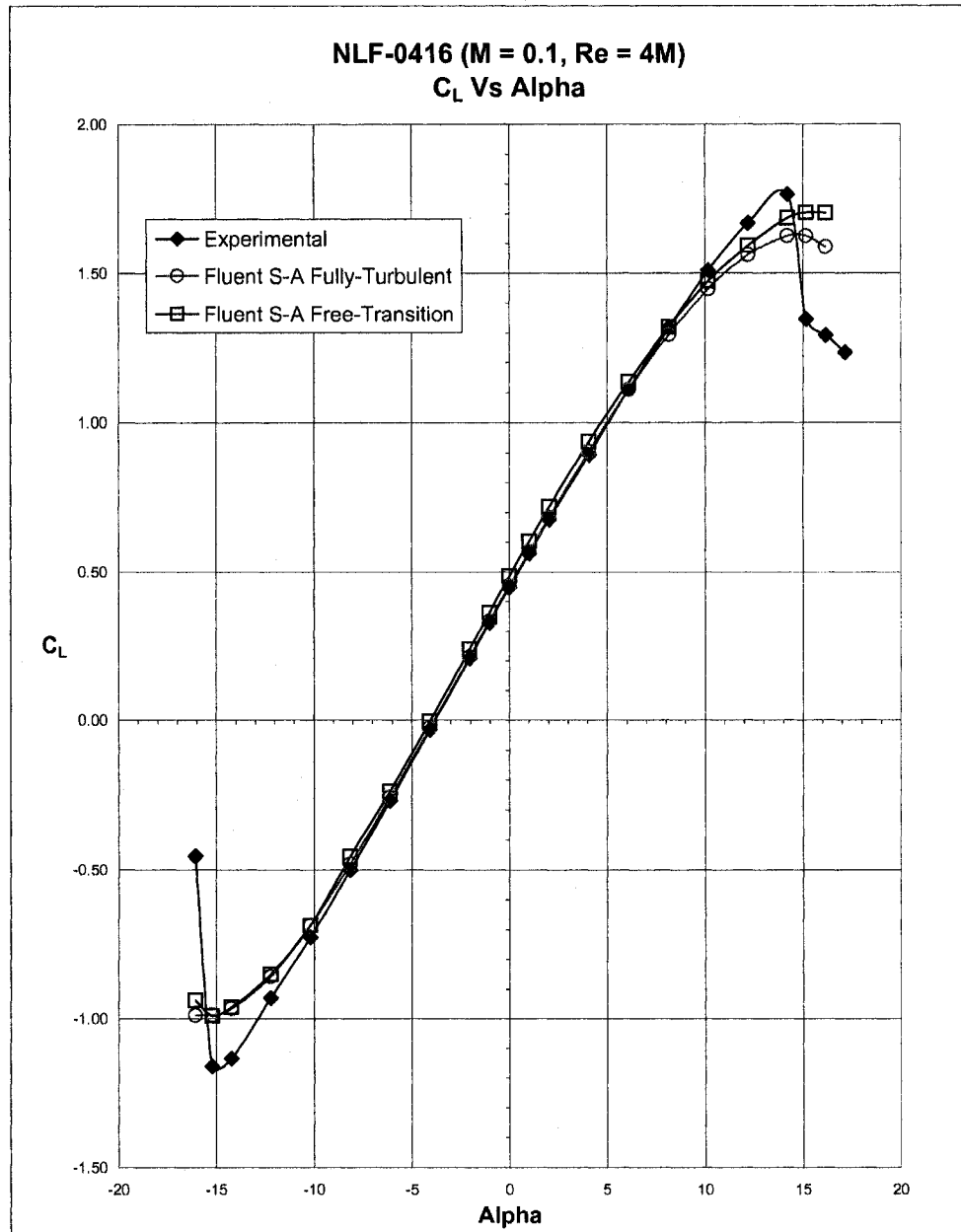


Figure 4.3: Lift coefficient comparison between experimental results and numerical results for the Fully-Turbulent and Free-Transition models for the NLF-0416 airfoil Case I ( $M_\infty = 0.1$ ,  $Re = 4 * 10^6$ ).

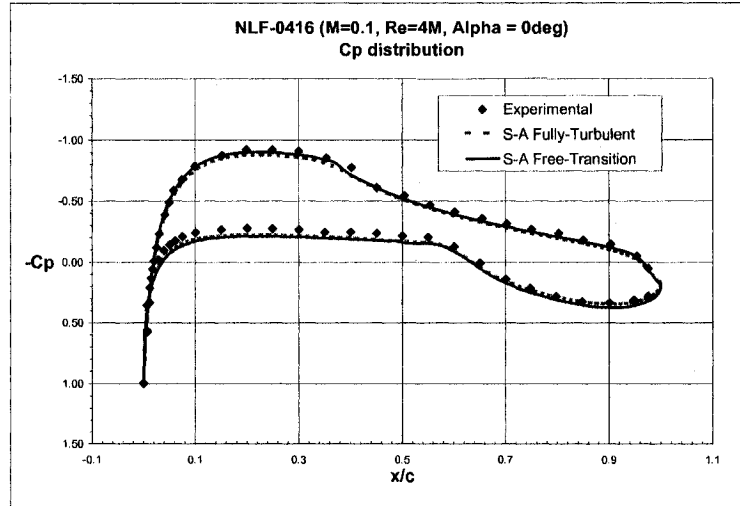


Figure 4.4: Pressure coefficient comparison between experimental results and numerical results for the Fully-Turbulent and Free-Transition models for the NLF-0416 airfoil at  $\alpha = 0^\circ$  ( $M_\infty = 0.1, Re = 4 * 10^6$ ).

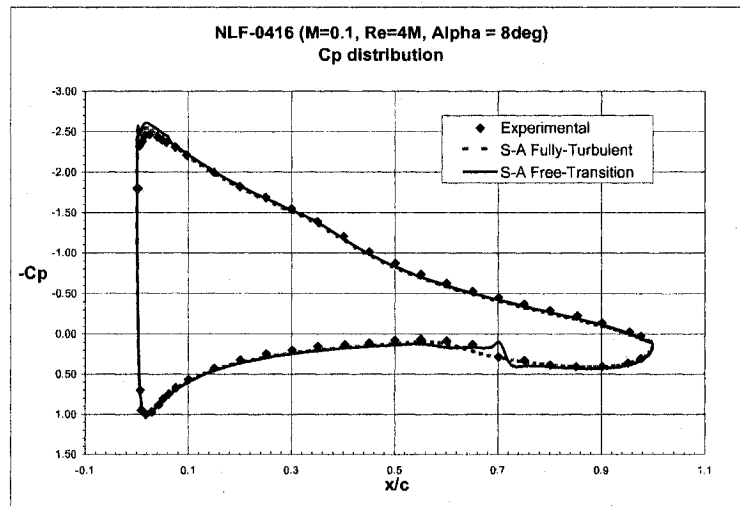


Figure 4.5: Pressure coefficient comparison between experimental results and numerical results for the Fully-Turbulent and Free-Transition models for the NLF-0416 airfoil at  $\alpha = 8^\circ$  ( $M_\infty = 0.1, Re = 4 * 10^6$ ).

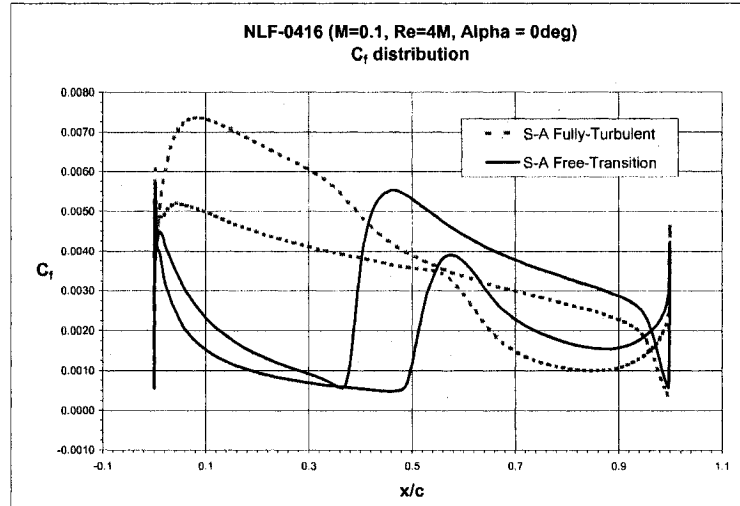


Figure 4.6: Skin-Friction coefficient comparison between numerical results obtained for the Fully-Turbulent and Free-Transition models for the NLF-0416 airfoil at  $\alpha = 0^\circ$  ( $M_\infty = 0.1, Re = 4 \times 10^6$ ).

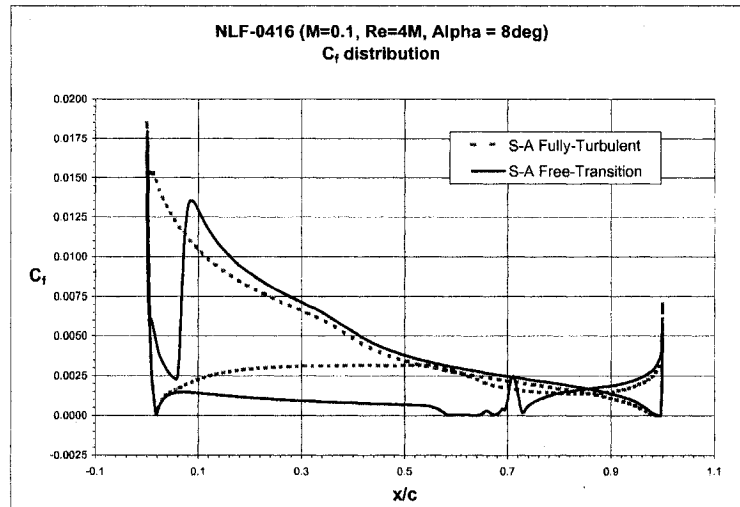


Figure 4.7: Skin-Friction coefficient comparison between numerical results obtained for the Fully-Turbulent and Free-Transition models for the NLF-0416 airfoil at  $\alpha = 8^\circ$  ( $M_\infty = 0.1, Re = 4 \times 10^6$ ).

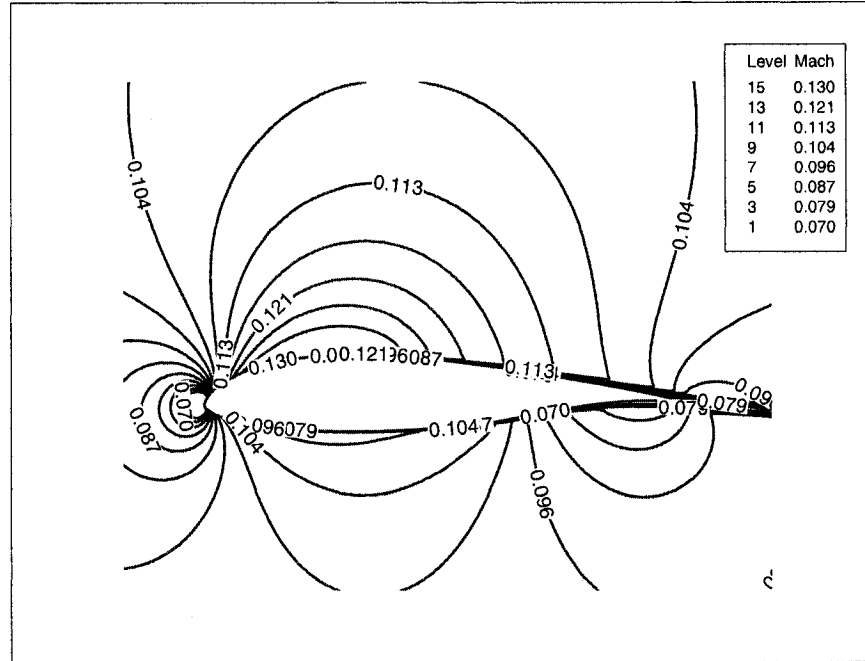


Figure 4.8: Mach number contours obtained using the Free-Transition model for the NLF-0416 airfoil at  $\alpha = 0^\circ$  ( $M_\infty = 0.1$ ,  $Re = 4 * 10^6$ ).

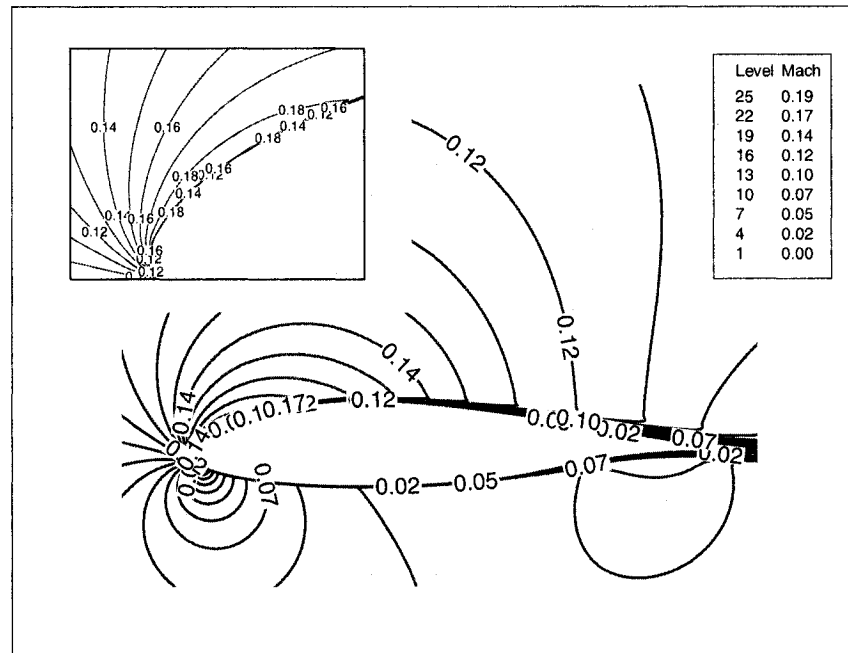


Figure 4.9: Mach number contours obtained using the Free-Transition model for the NLF-0416 airfoil at  $\alpha = 8^\circ$  ( $M_\infty = 0.1$ ,  $Re = 4 * 10^6$ ).



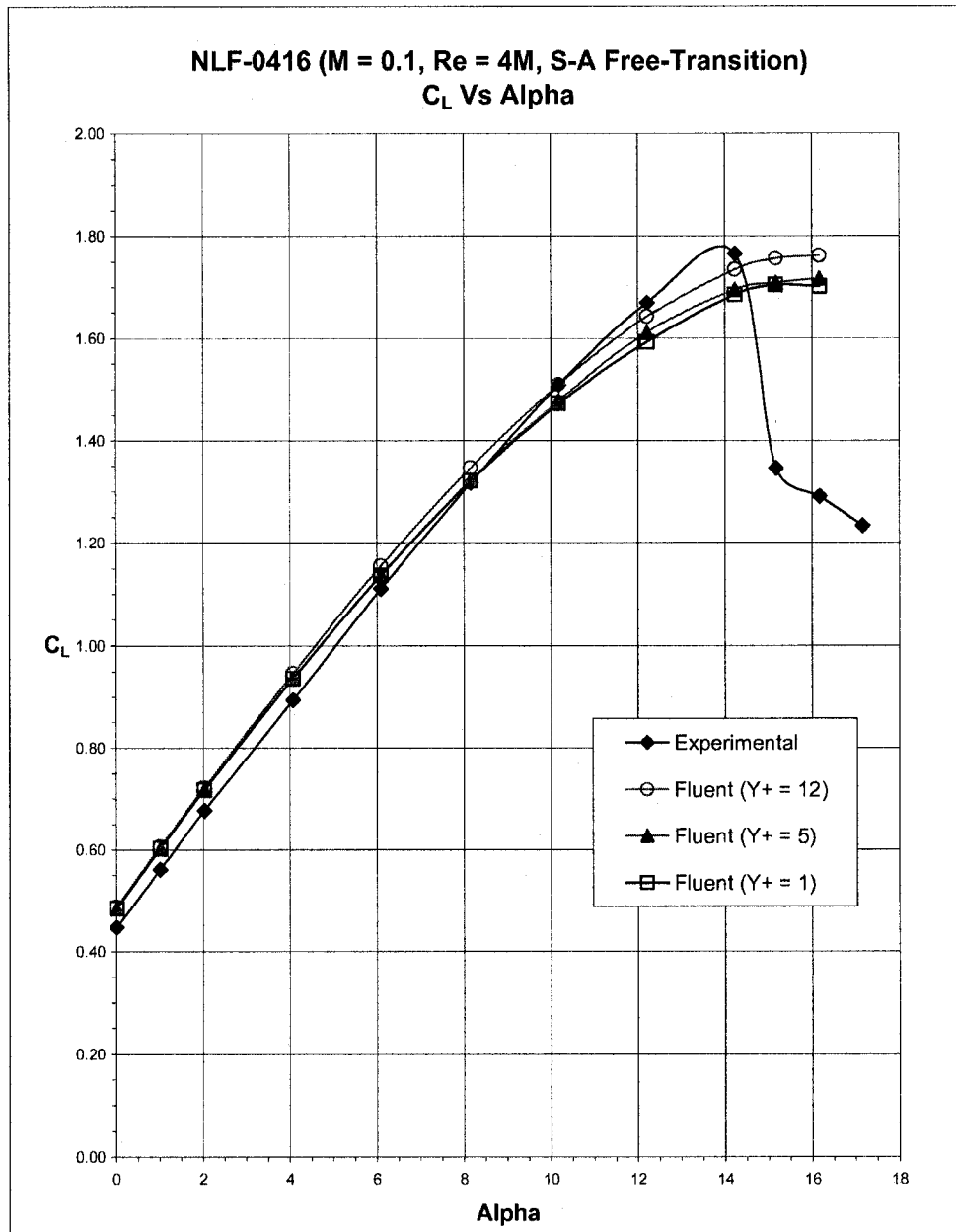


Figure 4.10: Lift coefficient comparison between experimental and numerical data for the Free-Transition model on three different meshes for the NLF-0416 airfoil Case I ( $M_\infty = 0.1$ ,  $Re = 4 \times 10^6$ ).

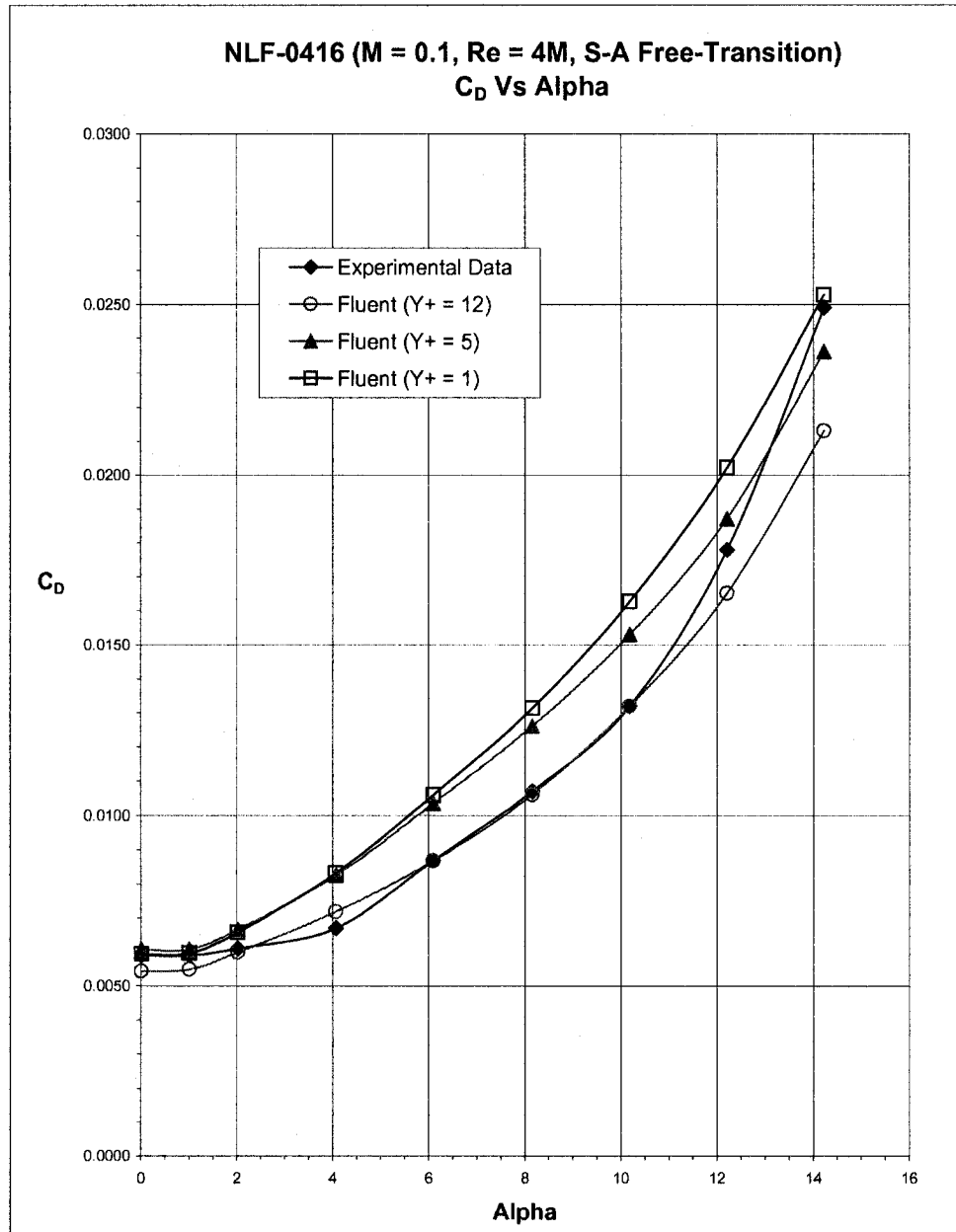


Figure 4.11: Drag coefficient comparison between experimental and numerical data for the Free-Transition model on three different meshes for the NLF-0416 airfoil Case I ( $M_\infty = 0.1$ ,  $Re = 4 * 10^6$ ) [error in experimental drag coefficient is equal to a maximum increase of 2%].

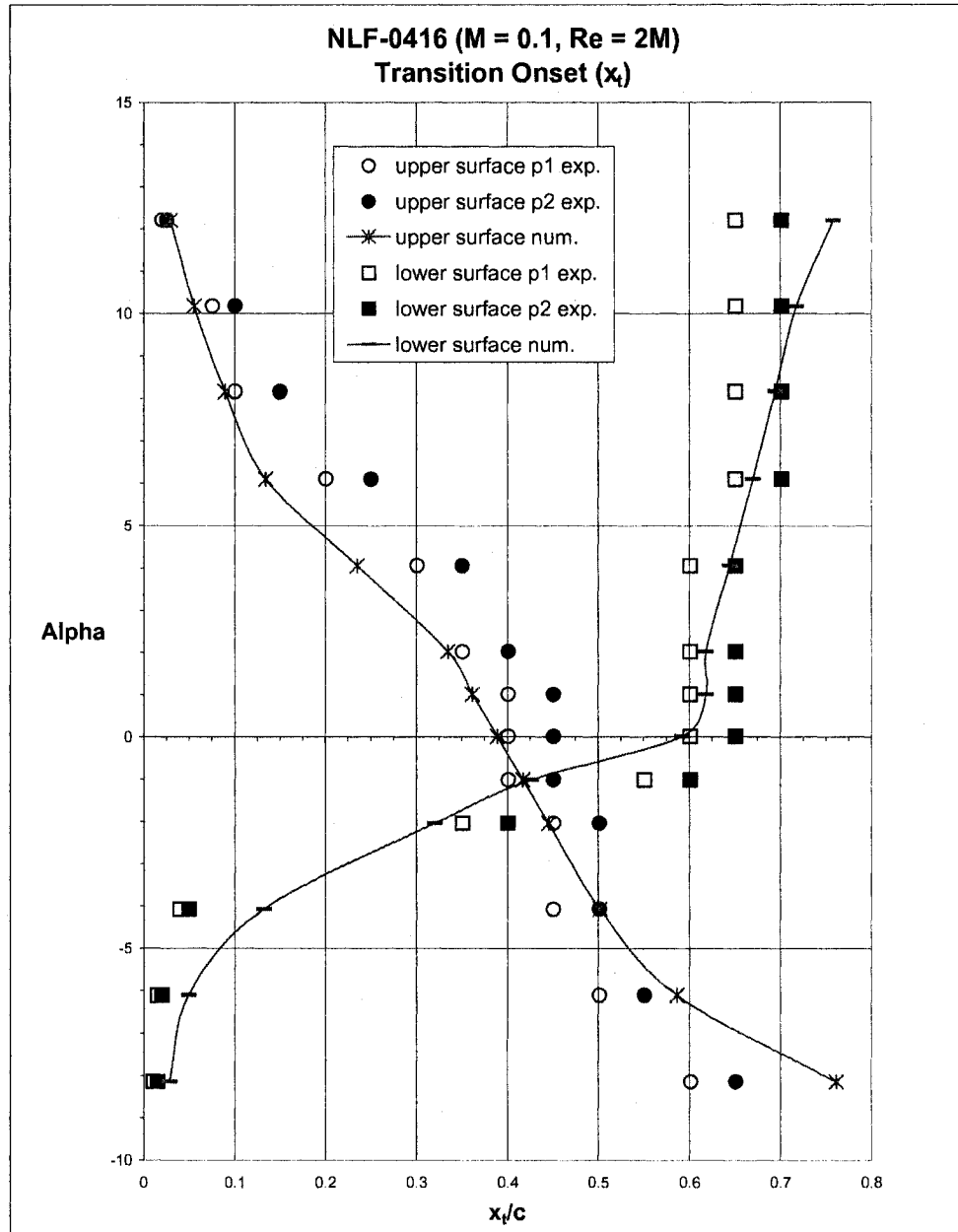


Figure 4.12: Model validation of the transition onset for the NLF-0416 airfoil Case II ( $M_\infty = 0.1$ ,  $Re = 2 \times 10^6$ ). (The empty dots and squares represent laminar region and the filled dots and squares represent turbulent regions. Solid lines correspond to numerical calculations.)

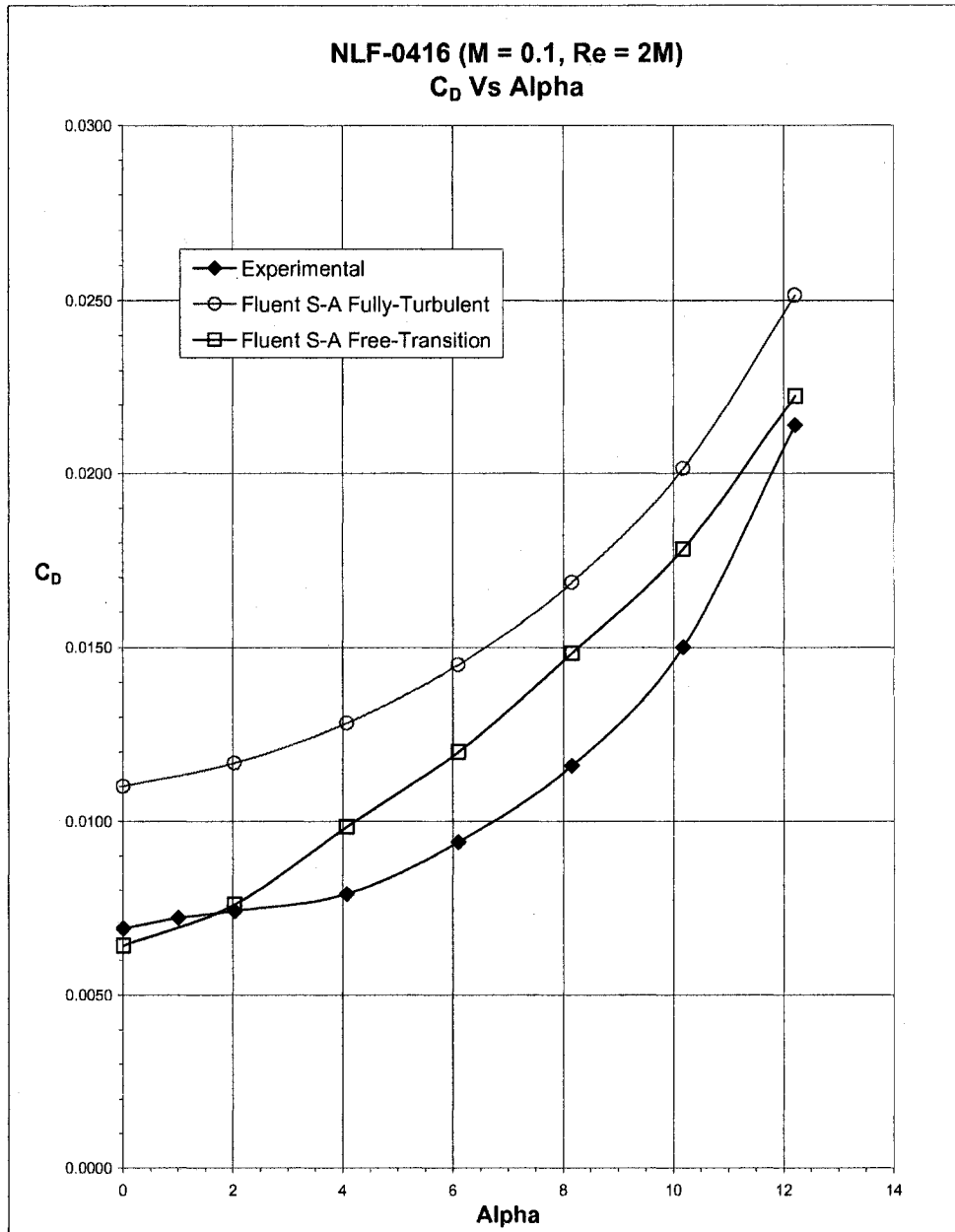


Figure 4.13: Drag coefficient comparison between experimental results and numerical results for the Fully-Turbulent and Free-Transition models for the NLF-0416 airfoil Case II ( $M_\infty = 0.1$ ,  $Re = 2 \times 10^6$ ) [error in experimental drag coefficient is equal to a maximum increase of 2%].

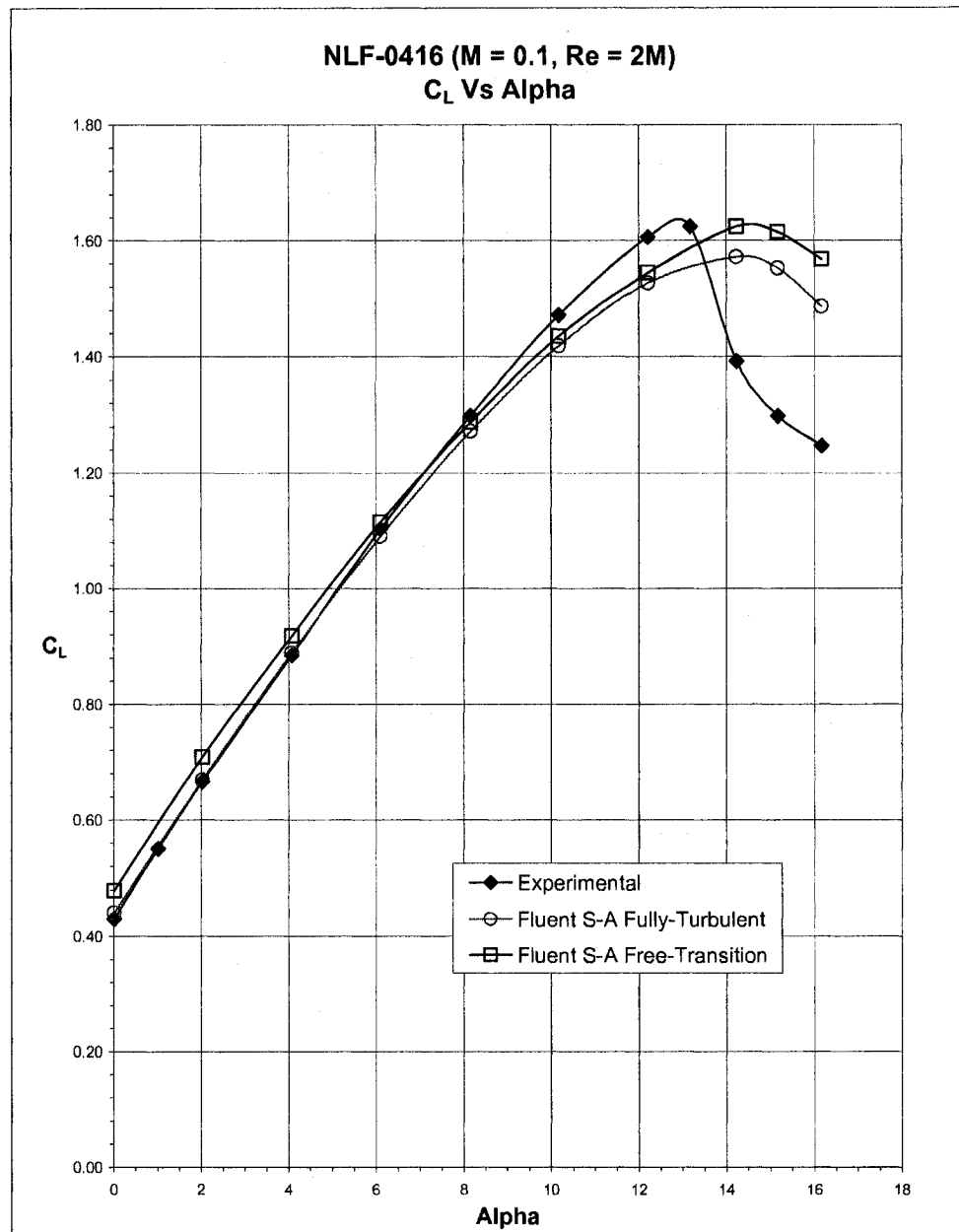


Figure 4.14: Lift coefficient comparison between experimental results and numerical results for the Fully-Turbulent and Free-Transition models for the NLF-0416 airfoil Case II ( $M_\infty = 0.1$ ,  $Re = 2 * 10^6$ ).

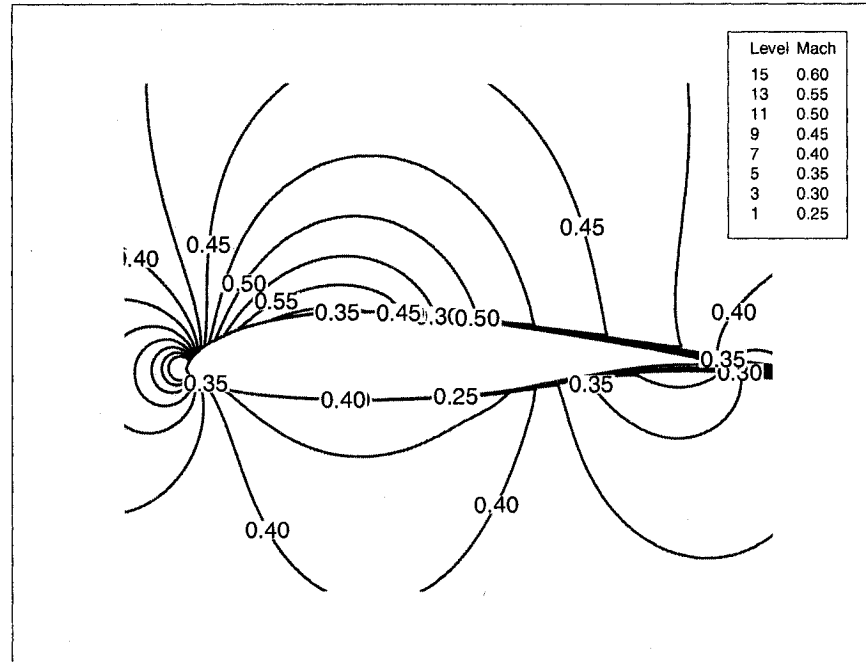


Figure 4.15: Mach number contours obtained using the Free-Transition model for the NLF-0416 airfoil at  $\alpha = 0^\circ$  ( $M_\infty = 0.4$ ,  $Re = 6 \times 10^6$ ).

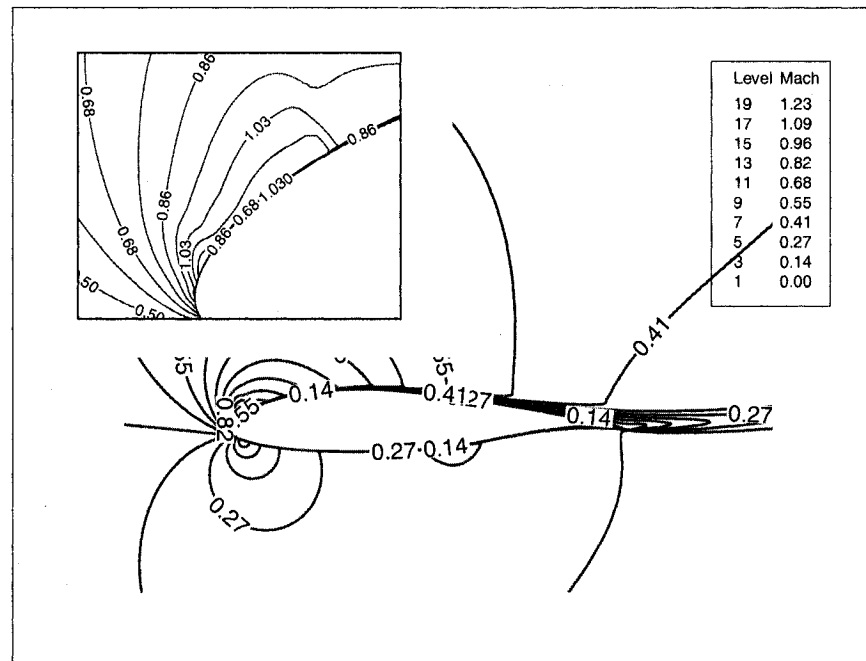


Figure 4.16: Mach number contours obtained using the Free-Transition model for the NLF-0416 airfoil at  $\alpha = 12^\circ$  ( $M_\infty = 0.4$ ,  $Re = 6 \times 10^6$ ).

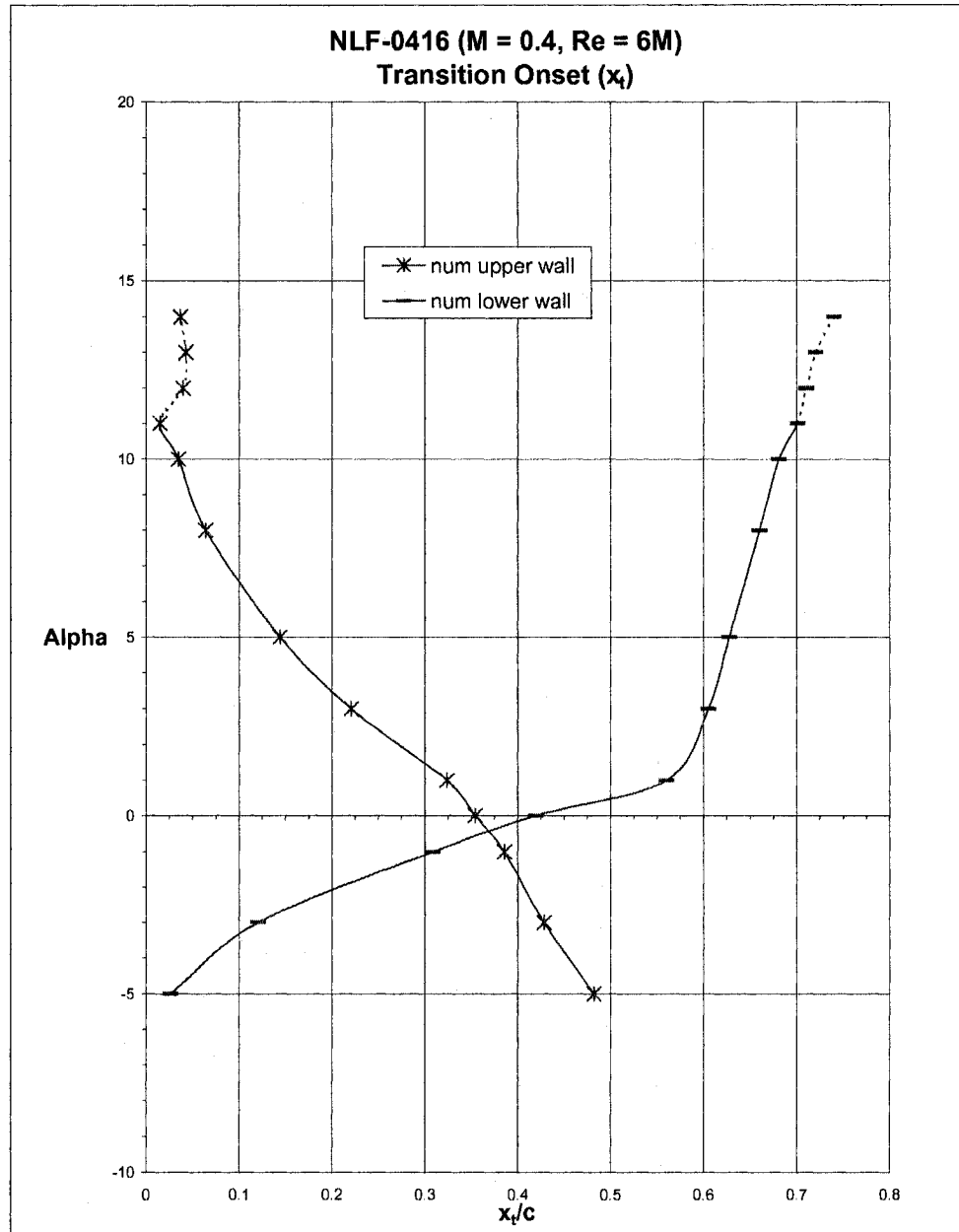


Figure 4.17: Model validation of the transition onset for the NLF-0416 airfoil Case III ( $M_\infty = 0.4$ ,  $Re = 6 * 10^6$ ).

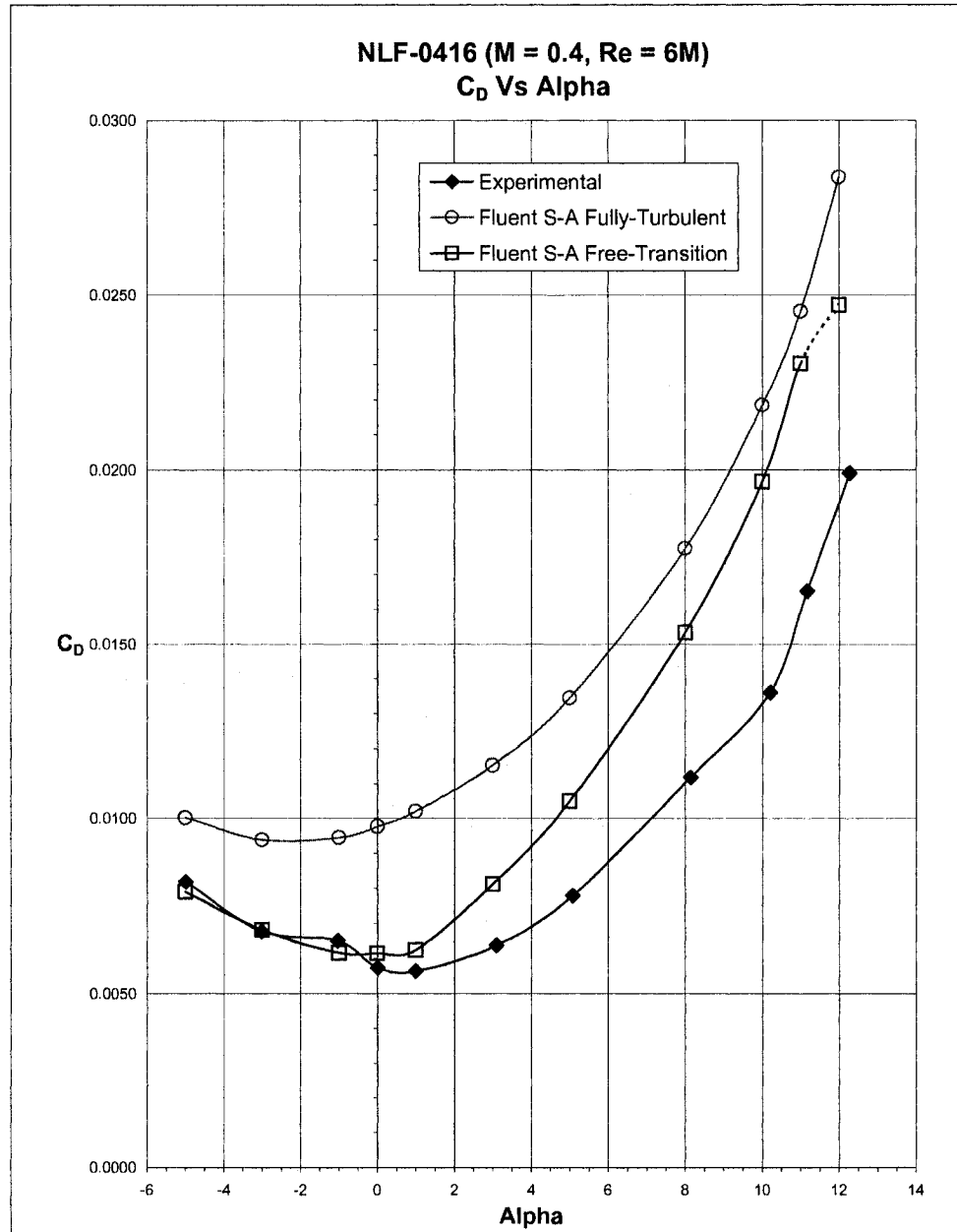


Figure 4.18: Drag coefficient comparison between experimental results and numerical results for the Fully-Turbulent and Free-Transition models for the NLF-0416 airfoil Case III ( $M_\infty = 0.4$ ,  $Re = 6 \times 10^6$ ) [error in experimental drag coefficient is equal to a maximum increase of 2%].



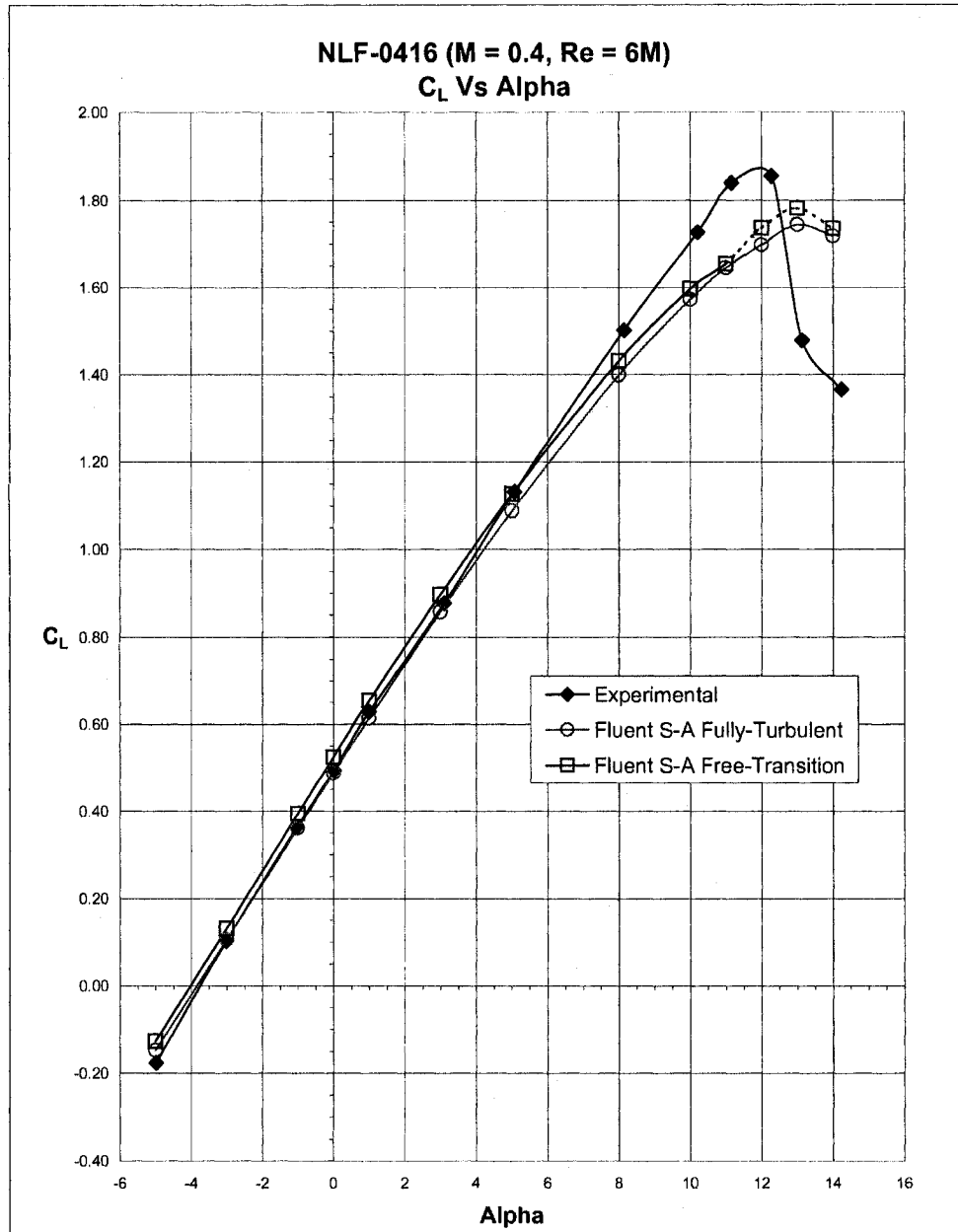


Figure 4.19: Lift coefficient comparison between experimental results and numerical results for the Fully-Turbulent and Free-Transition models for the NLF-0416 airfoil Case III ( $M_\infty = 0.4$ ,  $Re = 6 \times 10^6$ ).

## Chapter 5

# Transition Model Assessment for a Two-Element Airfoil

### 5.1. NLR-7301 Airfoil With a Trailing Edge Flap

The current chapter will discuss the results obtained for a two-element airfoil that is tested and well documented, the NLR-7301 airfoil with a trailing edge flap. This case was identified as a good candidate to test the developed transition model. The geometry and experimental data used for comparison are given in the AGARD AR-303 [21]. The experimental data available are for a free-stream Mach number  $M_\infty = 0.185$  and a Reynolds number  $Re_c = 2.51$  millions. Also the geometric configuration used in this case is that of a trailing flap with a 2.6% gap. While the surface pressure measurements are available for angles of attack between  $0^\circ$  and  $16^\circ$  at intervals of  $1^\circ$ , wake traverses and boundary layer measurements have been done at three angles of attack;  $6^\circ$ ,  $10.1^\circ$  and  $13.1^\circ$ . The error margin in the experimental data is given as  $\pm 0.01$  for the lift coefficient and  $\pm 2\%$  for the drag coefficient [21]. Here also error bars were not included in the corresponding figures to maintaining the clarity of the presented data.

The numerical simulations done in this work were carried out at selected angles of attack for both, the original Fully-Turbulent turbulence model and the modified Free-Transition model. Table 5.1 summarizes both the experimental and numerical data for the free-stream conditions. The grid used to perform the numerical calculations is a hybrid mesh with the first cell at a distance of  $10^{-5}$  chord from the wall. Both elements were surrounded by two separate structured C-type boundary layer meshes that extend at the trailing edge for a distance equal to 25 % of each element's length in order to capture the wake downstream of these elements. The mesh is composed of about 140K cells and 81K nodes.

	Experimental upstream flow	Numerical upstream flow
Mach Number	0.185	0.185
Reynolds Number	$2.51 * 10^6$	$2.51 * 10^6$
Angles of attack	$0^\circ$ to $16.1^\circ$ ( $C_L$ ) $6^\circ$ , $10.1^\circ$ , and $13.1^\circ$ ( $C_D$ )	$0^\circ$ , $3^\circ$ , $6^\circ$ , $10.1^\circ$ , $13.1^\circ$ , $14.1^\circ$ and $15.1^\circ$
Transition conditions	Free transition	a- Fully turbulent model b- Free transition model

Table 5.1: Experimental and numerical free-stream flow conditions for the NLR-7301 case.

Figures 5.1 and 5.2 show pressure coefficient distribution while Figs. 5.3 and 5.5 show the Mach number contours for two angles of attack;  $6^\circ$  and  $13.1^\circ$  respectively. Also figures representing the static pressure contours at the same angles of attack mentioned above are supplied (Figs. 5.4 and 5.6). Pressure coefficient plots show a good agreement between experimental results and the results obtained by the Free-Transition model. Also from Mach number contours shown in the corresponding figures, the maximum Mach number is about 0.582 and 0.811 for angles of attack  $6^\circ$  and  $13.1^\circ$ , respectively. This indicates that the flow is compressible in the boundary layer for some of the cases considered.

As in the results presented in previous cases, the three quantitative variables to be used for analysis are the transition onset, the lift and the drag coefficients. In

Fig. 5.7, the transition onset ( $x_t$ ) predicted using the Free-Transition model is plotted along side with the experimental values for the three available angles of attack, namely  $6^\circ$ ,  $10.1^\circ$  and  $13.1^\circ$ . The main observation that can be pointed out by examining Fig. 5.7 is that the transition onset is well predicted on the main airfoil while it is lagging the experimental values on the flap by almost one third of the flap length which is about 9% of the main element chord. This can be related to the fact that while the flow is smooth and attached in the boundary layer at the leading edge of the main element, these conditions start to deteriorate downstream. Thus for the case of the flap which is right behind the wake generated by the main element and is exposed to the jet coming from the pressure side through the gap, the assumptions under which the model was developed, namely incompressible attached flow, do not hold anymore. Therefore the Free-Transition model predictions are expected to be off. However, on the main airfoil, the predicted transition onset is in good agreement with the experimental data where the difference is about 5 % of the chord for the lower side of the main element and less than 1% of the chord for the upper side.

The drag and lift coefficients obtained from the simulations are compiled together with the experimental data and are given in Figs. 5.8 and 5.9, respectively. Again the data are divided into three sets: one corresponding to the experimental data given by the AGARD publication [21] and the other two are numerical results obtained using the Fully-Turbulent and Free-Transition models simulated using Fluent. Figure 5.8 shows a significant improvement in the drag values predicted using the Free-Transition model as opposed to those obtained using the Fully-Turbulent model. For an angle of attack  $\alpha = 6^\circ$ , the experimental drag coefficient is equal to 229 (0.0229) drag counts. The difference between the numerical value computed by the Fully-Turbulent model and the experimental one is equal to 78 (0.0078) drag counts. This difference drops to 5 drag counts (0.0005) with the Free-Transition model. The results obtained for the other two angles of attack ( $10.1^\circ$  and  $13.1^\circ$ ) show

the same behavior. Table 5.2 summarizes the difference in lift and drag coefficients, in reference to the experimental values, obtained using the two numerical models mentioned above.

Alpha	Experimental Data	Numerical Data Fully-Turbulent S-A	Numerical Data Free-Transition S-A
	$C_D(\pm 2\% \text{ error})$	Difference in $C_D$	Difference in $C_D$
6°	0.0229	78 drag count (+34%)	5 drag count (+2.1%)
10.1°	0.0323	127 drag count (+40%)	-2 drag count (-0.6%)
13.1°	0.0445	208.5 drag count (+47%)	-41.5 drag count (-9.3%)
	$C_L(\pm 0.01 \text{ error})$	Difference in $C_L$	Difference in $C_L$
6°	2.416	0.0312 (-1.29%)	0.1164 (+5.1%)
10.1°	2.877	0.1495 (-5.20%)	0.0362 (+1.3%)
13.1°	3.141	0.3127 (-10.0%)	0.0470 (-1.5%)

Table 5.2: Difference in the lift and drag coefficients between experimental and numerical results for the Fully-Turbulent and Free-Transition models for the NLR-7301 airfoil with a trailing flap [1 drag count =  $10^{-4}$ ].

As for the lift analysis, Fig. 5.9 shows that the variations in the lift coefficient is similar to that of the single element airfoil. Thus for angles of attack  $\alpha \leq 7.1^\circ$ , the Free-Transition model over-predicts the values given experimentally by an average difference of 0.138 while the difference between the experimental values and those predicted using the Fully-Turbulent model are on average difference of 0.015. For  $\alpha > 7.1^\circ$ , the values predicted by the Free-Transition are closer to the experimental data with an average difference equal to 0.05 while the difference between the experimental data and those obtained by the Fully-Turbulent model increases as angle of attack is increased. On a positive note, the  $C_{Lmax}$  predicted by the Free-transition model is in good agreement with the experimental data, in both value and location.

Drag and lift coefficients are also compiled together in a polar drag plot shown in Fig. 5.10. The figure highlights the excellent agreement between experimental data and those obtained numerically using the Free-Transition model compared to

the poor agreement between experimental data and those obtained using the Fully-Turbulent model. This clearly demonstrates the value of the current transition model in rightfully predicting the airfoil aerodynamic performance in terms of lift and drag.

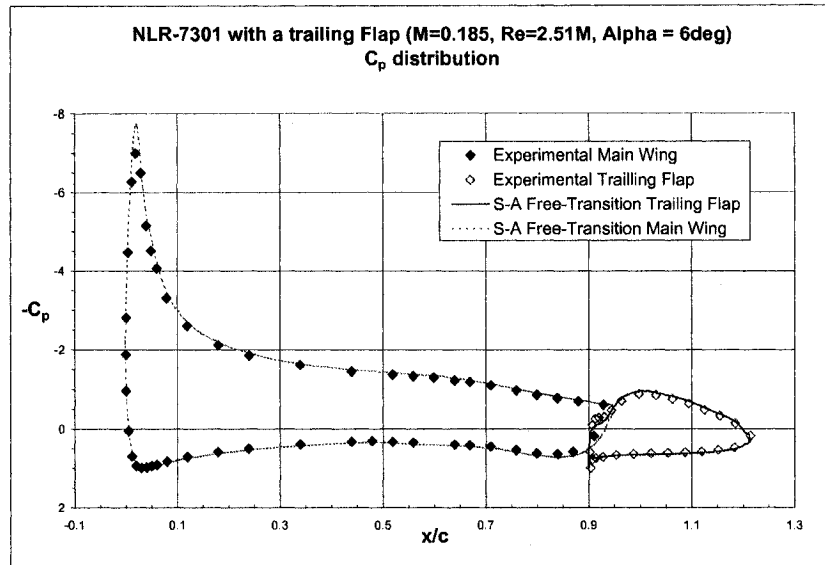


Figure 5.1: Pressure coefficient comparison between experimental results and numerical results for the Fully-Turbulent and Free-Transition models for the NLR-7301 airfoil with a trailing flap at  $\alpha = 6^\circ$ .

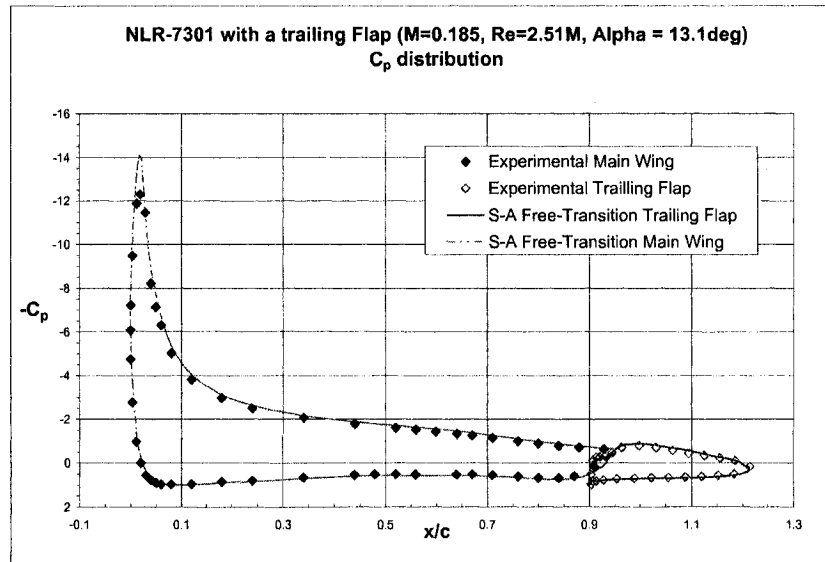


Figure 5.2: Pressure coefficient comparison between experimental results and numerical results for the Fully-Turbulent and Free-Transition models for the NLR-7301 airfoil with a trailing flap at  $\alpha = 13.1^\circ$ .

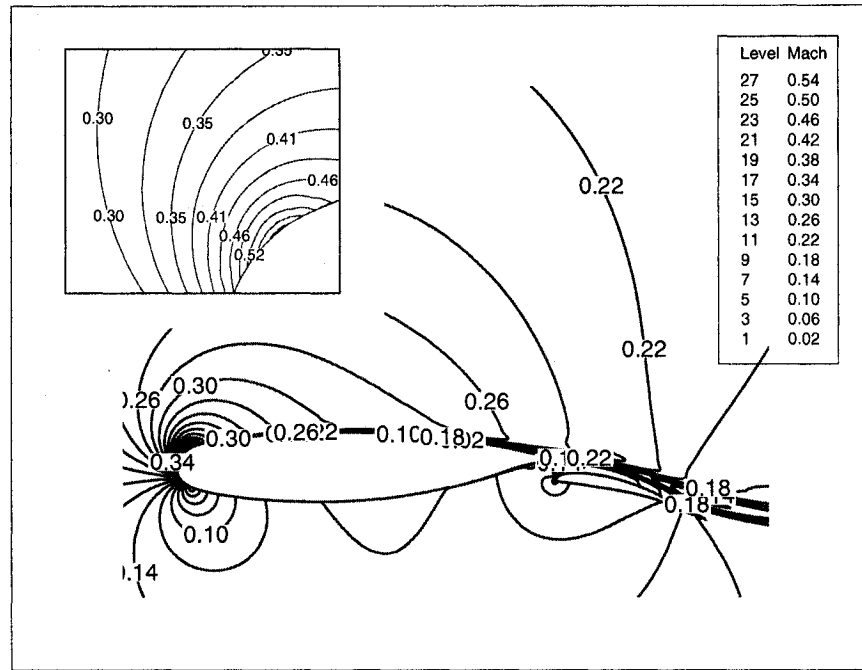


Figure 5.3: Mach number contours obtained using the Free-Transition model for the NLR-7301 airfoil with a trailing flap at  $\alpha = 6^\circ$ .

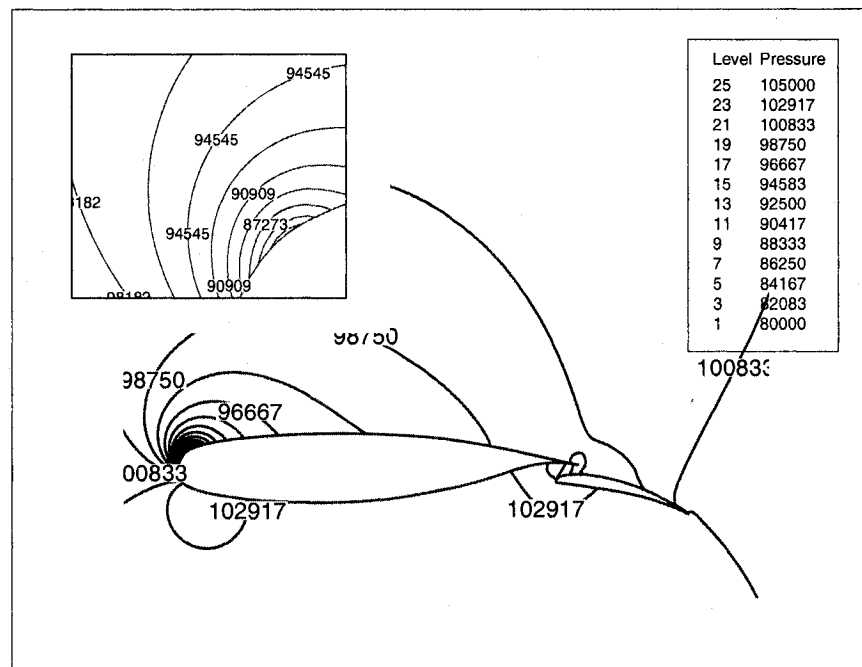


Figure 5.4: Static pressure contours obtained using the Free-Transition model for the NLR-7301 airfoil with a trailing flap at  $\alpha = 6^\circ$ .



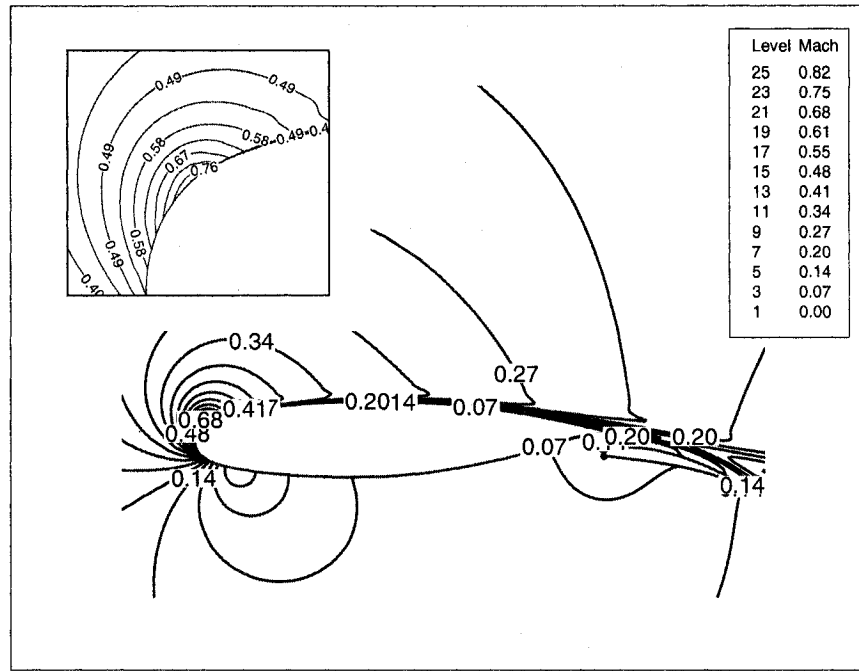


Figure 5.5: Mach number contours obtained using the Free-Transition model for the NLR-7301 airfoil with a trailing flap at  $\alpha = 13.1^\circ$ .

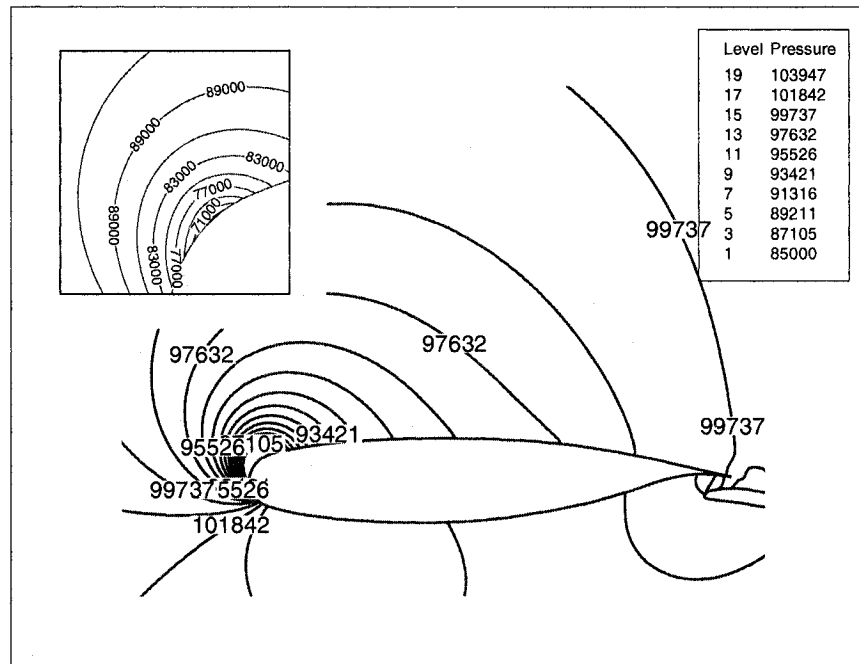


Figure 5.6: Static pressure contours obtained using the Free-Transition model for the NLR-7301 airfoil with a trailing flap at  $\alpha = 13.1^\circ$ .

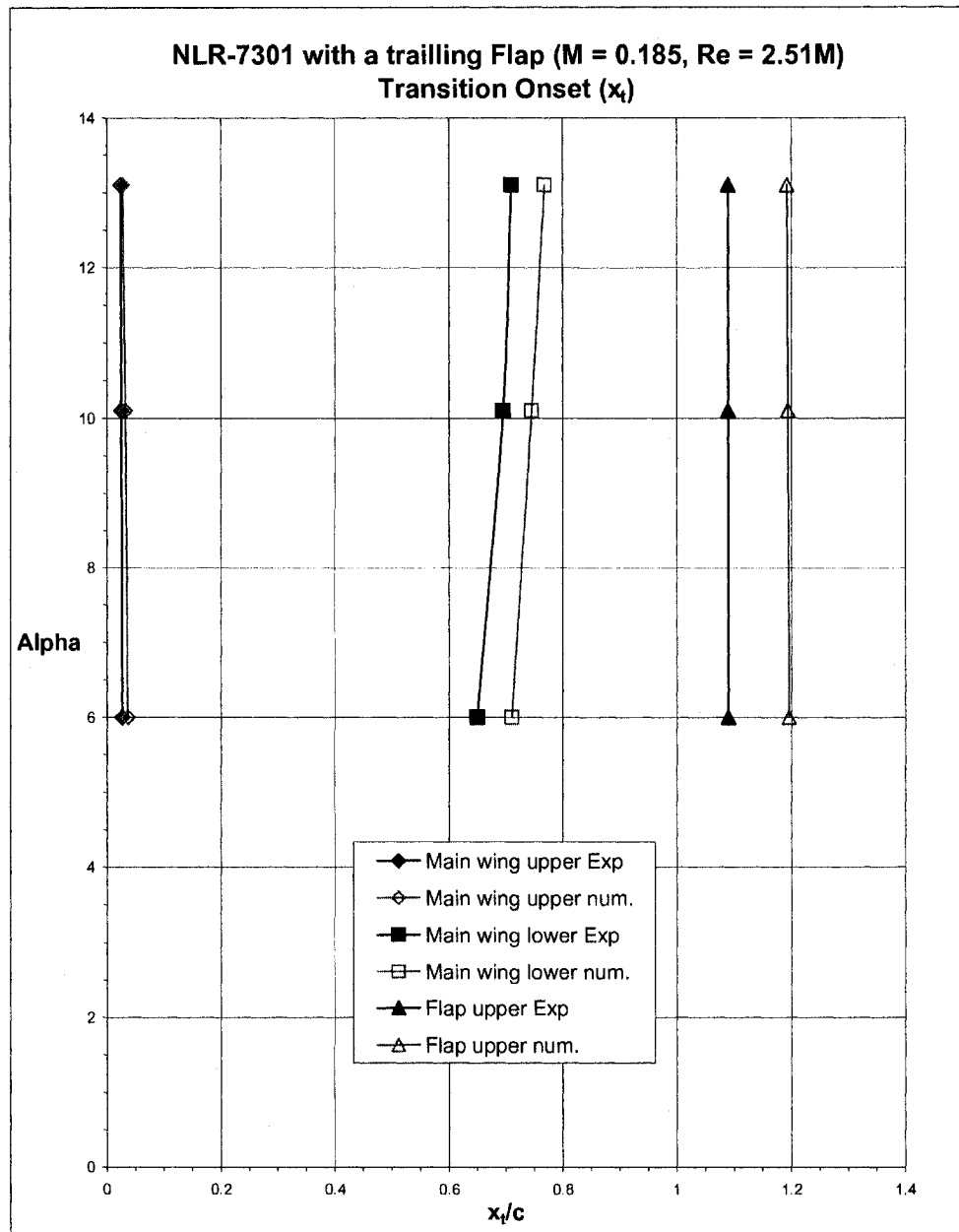


Figure 5.7: Model validation of the transition onset for the NLR-7301 airfoil with a trailing flap.

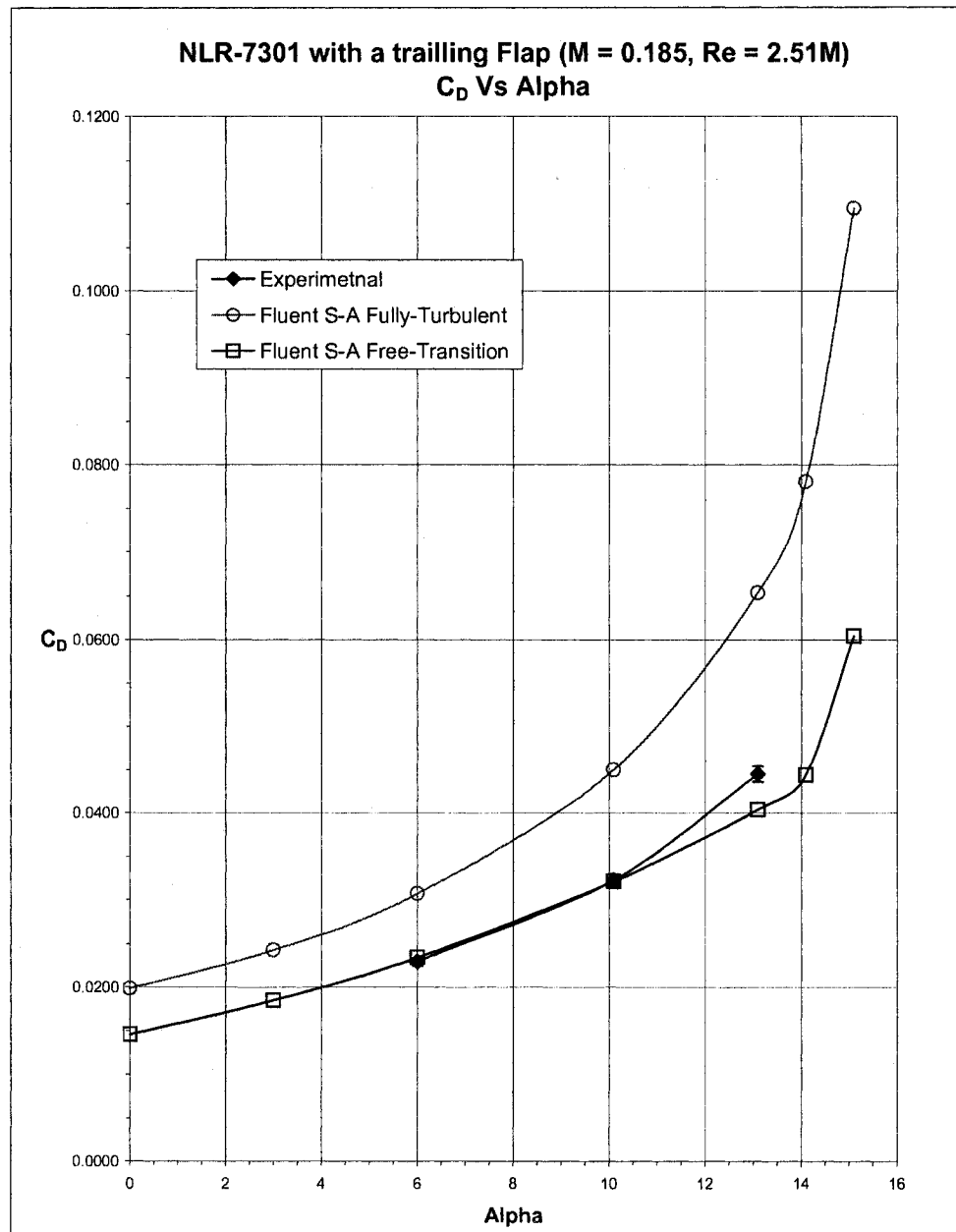


Figure 5.8: Drag coefficient comparison between experimental results and numerical results for the Fully-Turbulent and Free-Transition models for the NLR-7301 airfoil with a trailing flap [experimental drag coefficient error margin is equal to  $\pm 2\%$ ].

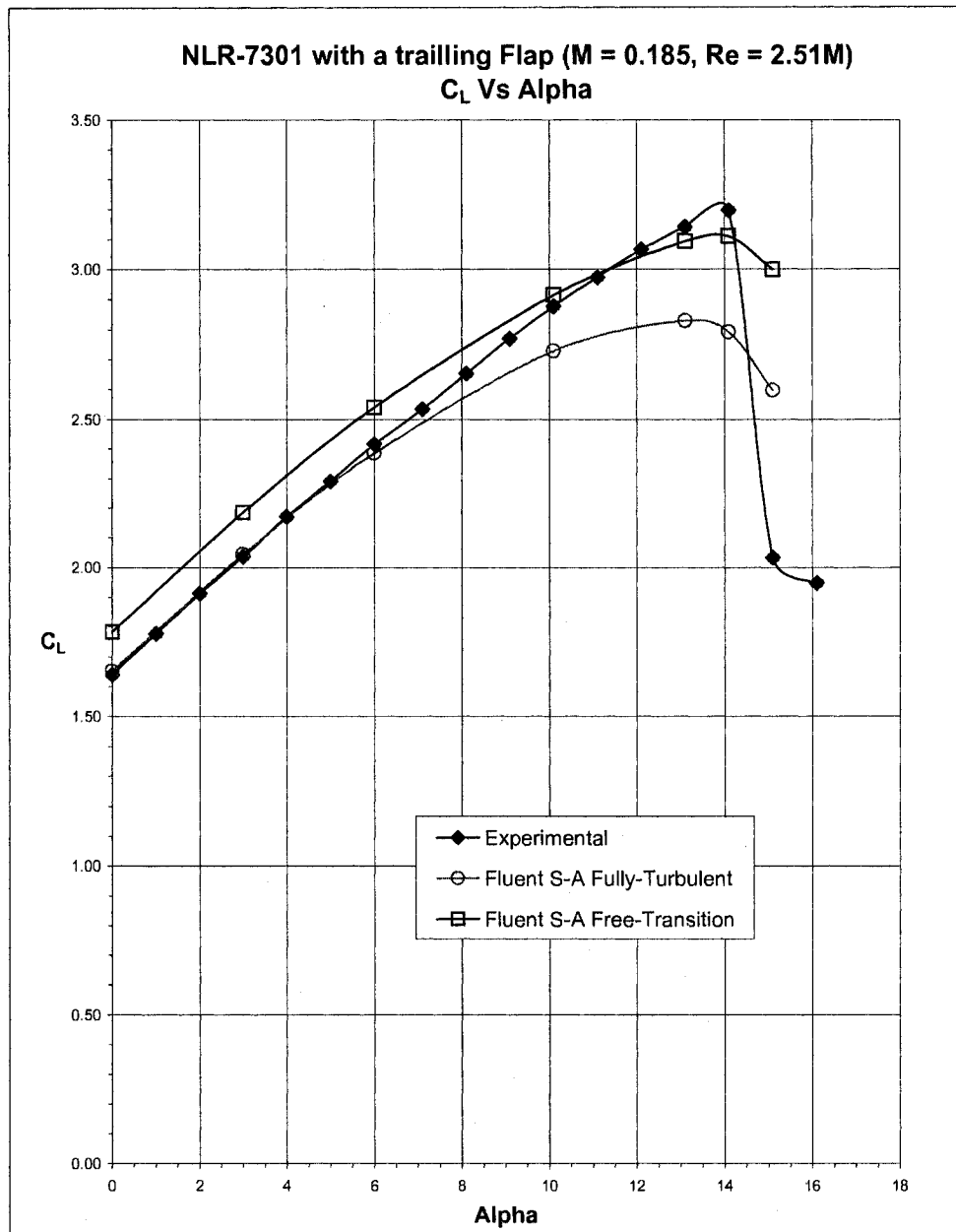


Figure 5.9: Lift coefficient comparison between experimental results and numerical results for the Fully-Turbulent and Free-Transition models for the NLR-7301 airfoil with a trailing flap [experimental lift coefficient error margin is equal to  $\pm 0.01$ ].

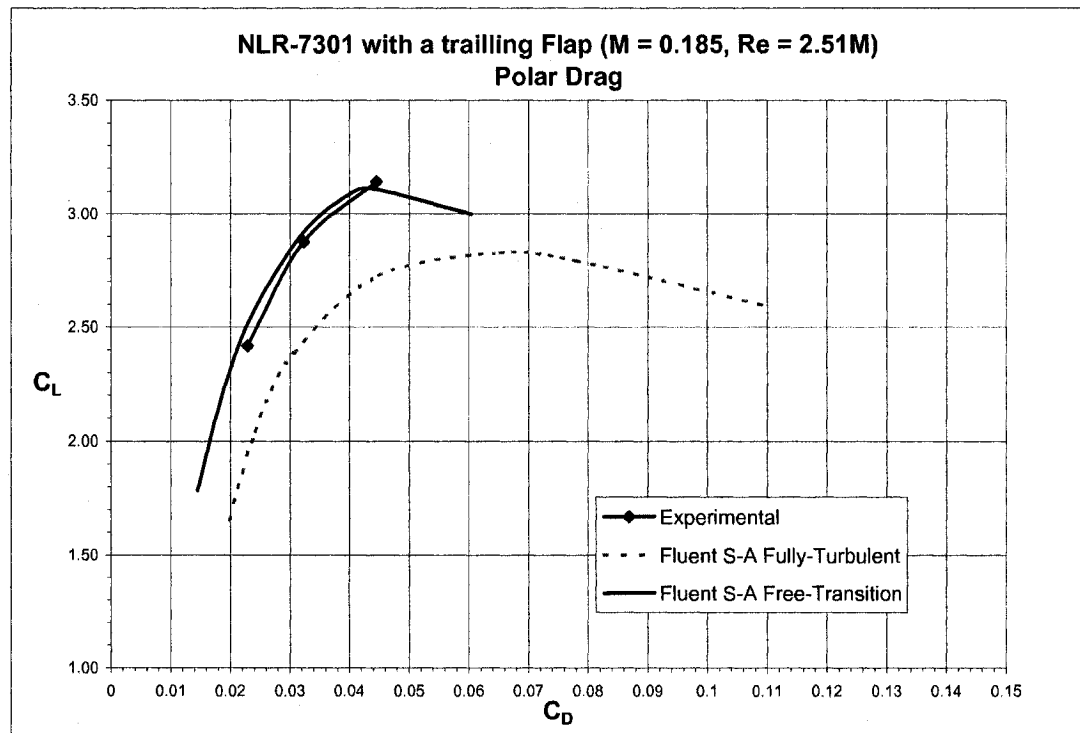


Figure 5.10: Polar drag plot representing experimental data and numerical data for the Fully-Turbulent and Free-Transition models for the NLR-7301 airfoil with a trailing flap.

# Chapter 6

## Conclusion

### 6.1. Completed Work

The objective of the current work was to develop a simple yet robust and accurate laminar to turbulent transition model that is capable of accurately predicting the drag in transitional flow over two-dimensional airfoils used typically in aerospace applications. This free transition model predicts both the onset and the extent of the transition region; it is implemented into the fully turbulent Spalart-Allmaras turbulence model available in Fluent where the RANS equations are solved. The model was then used in Fluent to simulate the flow over a wide range of angles of attack for two well documented experimental cases: a single-element airfoil (NLF-0416) and a two-element airfoil (NLR-7301 with a trailing edge flap). In both cases the drag values predicted using the developed free transition model are closer to the experimental values when compared with those computed using the original fully turbulent Spalart-Allmaras turbulence model. However, the accuracy in predicting the lift coefficient with the Free-Transition model deteriorates slightly for low angles of attack. It is also to be noted that when the model was tested at different free stream Mach numbers, the discrepancy between computed and experimental results increased

as  $M_\infty$  increased. This can be attributed to the fact that the transition model was developed for incompressible fluid flows. Nonetheless, it can be concluded that the Free-Transition model, presented in this work, resulted in a significant improvement in drag prediction for airfoils in transitional flow.

## 6.2. Future Work

As for any future additions to the current work, there are several issues that can be addressed. First, the empirical relations used for the transition onset prediction are based on incompressible attached flow for Reynolds number higher than 2 millions. Such restrictions have to be addressed so that the model would cover lower values of Reynolds number, especially that large laminar bubbles start to form in such Reynolds number ranges. Another topic to be tackled is the effect of compressibility on the boundary layer flow, especially in cases where the flow is transonic. Such a concern was reflected in the results obtained for the single-element airfoil case (NLF-0416) under compressible flow conditions ( $M_\infty = 0.4$ ). Hence, the empirical equations used to predict the transition onset can be adjusted such that the current transition model will be able to cover not only lower Reynolds numbers but also higher Mach numbers.

Beside the cases tested in the current work (a single- and a two-element airfoil), a more challenging case that would be interesting to study is that of a three-element airfoil. However, due to the lack of experimental data for natural transition conditions, a three-element case was not assessed in the current work.

Finally, this model can be extended to three-dimensional flows over wings. Two aspects have to be considered: first, the physics of natural transition over a wing have to be addressed, second the compatibility of the model with the geometry being considered has to be accounted for.

# Bibliography

- [1] C. V. Dam, *Aircraft Design and the Importance of Drag Prediction*. VKI Lecture Series: CFD-Based Aircraft Drag Prediction and Reduction, 2003.
- [2] C. V. Dam, *Critical Factors in CFD-Based Drag Prediction*. VKI Lecture Series: CFD-Based Aircraft Drag Prediction and Reduction, 2003.
- [3] T. Cebeci, *An Engineering Approach to The Calculation of Aerodynamic Flows*. Springer, 1999.
- [4] H. Reed, T. Haynes, and W. Saric, “Computational fluid dynamics validation issues in transition modeling,” *AIAA Journal*, vol. 36, pp. 742–751, 1998.
- [5] T. Cebeci and A. M. O. Smith, *Analysis of Turbulent Boundary Layers*. New York: Academic Press, 1974.
- [6] F. M. White, *Viscous Fluid Flow*. New York: McGraw-Hill, 2nd ed., 1991.
- [7] M. Drela and M. Giles, “Viscous-inviscid analysis of transonic and low reynolds number airfoils,” *AIAA Journal*, vol. 25, pp. 1347–1355, 1987.
- [8] R. Narasimha, “Modeling the transitional boundary layer,” *ICASE Report No 90-90*, 1990.
- [9] S. Dhawan and R. Narasimha, “Some properties of boundary layer flow during the transition from laminar to turbulent motion,” *Journal of Fluid Mechanics*, vol. 3, pp. 418–436, 1958.



- [10] K. Chen and N. Thyson, "Extension of emmons' spot theory to flows on blunt bodies," *AIAA journal*, vol. 9, pp. 821–825, 1971.
- [11] J. Edwards, C. Roy, F. Blottner, and H. Hassan, "Development of a one-equation transition/turbulence model," *AIAA journal*, vol. 39, pp. 1691–1698, 2001.
- [12] E. Warren and H. Hassan, "Transition closure model for predicting transition onset," *Journal of Aircraft*, vol. 35, pp. 769–775, 1998.
- [13] J. Steelant and E. Dick, "Modelling of bypass transition with conditioned navier-stokes equations coupled to an intermittency transport equation," *International Journal for Numerical Methods in Fluids*, vol. 23, pp. 193–220, 1996.
- [14] J. Cho and M. Chung, "A  $k-\epsilon-\gamma$  equation turbulence model," *Journal of Fluid Mechancis*, vol. 237, pp. 301–322, 1992.
- [15] T. Cebeci, "Essential ingredients of a method for low reynolds-number airfoils," *AIAA journal*, vol. 27, pp. 1680–1688, 1989.
- [16] B. Thwaites, "Approximate calculation of the laminar boundary layer," *Aeronautical Quarterly*, vol. 1, pp. 245–280, 1949.
- [17] Fluent, *User's Guide documentation*. Lebanon, NH: Fluent Inc. Canterra Resource Park, 2003.
- [18] P. Spalart and S. Allmaras, *A One-Equation Turbulence Model for Aerodynamic Flows*. AIAA paper-92-0439, 1992.
- [19] J. D. Ferris, R. J. McGhee, and R. W. Barnwell, *Low Speed Wind-Tunnel Results for Symmetrical NASA LS(1)-0013 Airfoil*. NASA TM-4003, 1987.
- [20] D. M. Somers, *Design and Experimental Results for a Natural-Laminar-Flow Airfoil for General Aviation Applications*. NASA Technical Paper 1861, 1981.

- [21] B. Van Den Berg and J. Gooden, *Low-Speed Surface Pressure and Boundary Layer Measurement Data for the NLR-7301 Section With Trailing Edge Flap*. AGARD AR-303, 1994.